Chapter 2
Design Methods for HgCdTe Infrared Detectors

2.1 Introduction

HgCdTe infrared detectors have been available for half a century. Many physical models of HgCdTe infrared detectors, which are based on the basic principles of semiconductor physics, have been developed. These models have been widely used in the design and simulation of HgCdTe infrared detectors for the development of infrared detector technology. However, the accuracy of device and material parameters used in the physics models, which is very important for design and simulation, is strongly dependent on the processing conditions of device and material. Obtaining these parameters precisely is a problem, which should be solved urgently by the development of device design technology. This chapter covers some methods and results for the extraction of device and material parameters. Another key point is the effectiveness of the models used in specific design and simulation software. Because of the complexity of actual device structure, three-dimensional (or two-dimensional equivalent structure) modeling software is often required for an accurate device simulation. Simplifying the calculation model is usually applied to reduce the probability of divergence in finite element mathematical problems and computation time. However, the validity of the simplified model is only effective to certain specialized devices. At the same time, one has to acquire a set of characteristic device and material parameters based on the basic model used for the actual design method. In this chapter, methods of characteristic parameter extraction and model optimization are introduced in detail.

First, this chapter presents a basic theoretical framework based on semiconductor *p-n* junction theoretical models for simulation of HgCdTe infrared detectors, and some precision optimization results of the relationship between carrier's concentration and Fermi level for HgCdTe materials. Second, the spectral response, cross talk and other important properties of HgCdTe infrared detectors, including two-color devices, are calculated and compared with experimental results. Lastly, the effective extraction method of the characteristic parameters from fabricated

© National Defense Industry Press, Beijing and Springer-Verlag Berlin Heidelberg 2016

L. He et al., *Technology for Advanced Focal Plane Arrays of HgCdTe and AlGaN*,
DOI 10.1007/978-3-662-52718-4_2

HgCdTe infrared detectors is introduced, including extractions of material parameters from device current–voltage characteristics, extraction of minority carrier lifetime in *pn* junction structure from photoelectric response, and so on.

2.2 Simulation and Design of HgCdTe Infrared Detectors

Hg is usually unstable in HgCdTe materials due to the fragility of chemical bonds Hg–Cd, which results in the formation of Hg vacancy and Hg clusters. These formations cause some physical parameters of the current–voltage characteristics of HgCdTe *p-n* junctions be randomly discrete, and together with the influence of other defects, result in the nonuniformity of device performance. Therefore, it is necessary to establish a device design platform, which is closely related to the nominal manufacturing process. This section outlines the basic assumptions of the conventional analytical model, and establishes the fitting method of characteristic parameter extraction. Effects of process conditions on the device performance are analyzed statistically, providing a theoretical basis for design and performance optimization of HgCdTe infrared detectors.

2.2.1 Foundation for HgCdTe Infrared Detector Designs

Traditional simulation of semiconductor devices is mainly to solve the combination of the Poisson equation (Eq. 2.1), steady-state continuity equation (Eq. 2.2), and carrier current density equation (Eq. 2.3) within specific boundary conditions of the device:

$$\nabla^2\psi = -\frac{q}{\varepsilon_0\varepsilon}(\Gamma + p - n) - \frac{1}{\varepsilon}\nabla\psi\nabla\varepsilon \tag{2.1}$$

$$\frac{1}{q}\nabla\vec{J}_{\mathrm{n}} + (G - R) = 0; \quad \frac{1}{q}\nabla\vec{J}_{\mathrm{p}} - (G - R) = 0 \tag{2.2}$$

$$\vec{J}_{\mathrm{n}} = qn\mu_{\mathrm{n}}\vec{E}_{\mathrm{n}} + qD_{\mathrm{n}}\nabla n; \quad \vec{J}_{\mathrm{p}} = qp\mu_{\mathrm{p}}\vec{E}_{\mathrm{p}} - qD_{\mathrm{p}}\nabla p \tag{2.3}$$

where Ψ, q, and ε are the electrostatic potential, electron charge, and permittivity of the semiconductors respectively. R is the carrier recombination rate, and G is the carrier generation rate. n and p are the concentrations of electrons and holes, where J_{n} and J_{p} are the electron and hole current densities respectively. D_{n} and D_{p} are the electron and hole diffusion coefficients, E_{n} and E_{p} are the electron and hole effective electric fields, and μ_{n} and μ_{p} are the electron and hole mobility respectively. These equations evolve into nonlinear equation groups with the finite element method (FEM), then are solved by a method such as the Newton iteration process. For the

analysis of the photoelectric effect for semiconductor devices, the photogeneration rate should be added to Eq. 2.2.

The photogeneration is simulated by ray tracing:

$$G^{\text{opt}}(z) = J(x, y, z_0) \cdot \alpha(\lambda, z) \cdot \exp\left[-\left|\int_{z_0}^{z} \alpha(\lambda, z)\mathrm{d}z\right|\right] \tag{2.4}$$

where λ is the wavelength, $\alpha(\lambda, z)$ is the absorption coefficient of HgCdTe material, $J(x, y, z_0)$ is the optical beam spatial variation of intensity over the window where rays enter the device, and z_0 is the position along the ray where absorption begins.

Narrow gap semiconductors, such as HgCdTe, have the following characteristics: (1) Conduction band $E(k)$ of HgCdTe, which can be described by Kane's $\boldsymbol{k}.\boldsymbol{p}$ model, is a non-parabolic belt, so the electron concentration in the conduction band should be fixed [1–4]. (2) The effective electron mass of the HgCdTe conduction band is very small, which causes the semiconductor to degenerate due to the low effective state density of the conduction band under low temperatures. Therefore, the distribution of carrier concentration obeys Fermi–Dirac statistics [5–7]. Fermi–Dirac integrals must be employed in the calculation of these two additional characteristics, which results in many difficulties for theoretical simulation. Only HgCdTe material parameters were joined into the parameter library when the numerical model is applied for our theoretical analysis [8–11]. However, the influence of these two characteristics has never been considered in analytical modeling [12–14]. In order to perfect the existing analytical and numerical models, this section presents a simple carrier approximation model, and applies these two characteristics of HgCdTe to device simulations. Finally, the necessity and adaptability of carrier approximate models are assessed by the analytical model.

2.2.1.1 Model of Carrier Density Approximation

The effects of carrier degeneracy and conduction band non-parabolicity are introduced into the device simulation by the expression that describes the relation between the Fermi energy and the carrier density [14]. Until the present time, there have been no detailed reports on the effects of carrier degeneracy and conduction band non-parabolicity on the simulation of the HgCdTe photovoltaic devices [14–20]. Some papers mention that neglecting the two factors leads to enormous errors in the calculation of the electron density and causes an overestimated dark current in the devices [20]. Therefore, practically understanding the carrier degeneracy and conduction band non-parabolicity effects on the simulation of HgCdTe photovoltaic devices and establishing a simple carrier density approximation that takes account of the two factors in simulation will be greatly beneficial to the design, analysis, and characterization of HgCdTe devices.

The general carrier density can be expressed by [15]:

$$n = \int \frac{\mathrm{d}N}{\mathrm{d}E} \cdot f(E) \cdot \mathrm{d}E \tag{2.5}$$

where $\mathrm{d}N/\mathrm{d}E$ is the density of the energy states, and $f(E)$ the distribution function.

By considering both carrier degeneracy and conduction band non-parabolicity, the distribution function $f(E)$ should be a Fermi function because of the carrier degeneracy. And the carrier density is given by the following integral expression [16–18]:

$$n = \frac{2N_c}{\sqrt{\pi}} \int_0^\infty \frac{\varepsilon^{1/2}(1+\alpha\varepsilon)^{1/2}(1+2\alpha\varepsilon)}{\exp(\varepsilon-\phi)+1}\mathrm{d}\varepsilon \tag{2.6}$$

Here we take the zero energy to be at the bottom of the conduction band, $\varepsilon = E/kT$ is the normalized electron kinetic energy, $\phi = E_f/kT$ the reduced Fermi energy, N_c the effective density of states. The coefficient $\alpha = \frac{1}{\varepsilon_g}\left(1 - \frac{m_e^*}{m_0}\right)^2$ is the non-parabolicity factor, here $\varepsilon_g = E_g/kT$ is the normalized band gap, and m_e^* and m_0 are electron effective mass and free electron mass, respectively.

The numerical calculation of Eq. (2.6) is time-consuming and hence is not suitable for efficient device simulation. Therefore, a simplified analytic approximation of Eq. (2.6) is often needed. Ariel et al. have proposed a relationship between Fermi energy ϕ and carrier density n, where carrier degeneracy and conduction band non-parabolicity have been taken into account [18]. Ariel's model, however, is only applicable for weak degeneracy. Additionally, they treated the effective mass m_e as constant. It is well known that m_e has a dependence on the band gap ε_g. When we take this dependence into consideration, it is shown in Fig. 2.1 that Ariel model deviates from the numerical solution of Eq. (2.6) in the range of about $\phi > 7$. For n-on-p devices whose junction is formed by ion implantation, the carrier concentration on n-side could be up to the order of 10^{18} cm^{-3} [16, 19], and at the liquid nitrogen cooled temperature, the Fermi energy ϕ is in the order of 20–30. Hence, it is necessary to have the solution of Eq. (2.6) in the range of $\phi < 30$ for practical HgCdTe device simulations.

In this work, we propose a new simple carrier approximation derived from the Ariel model, adding three parameters α_1, α_2, and B_2 as follows:

$$\phi = \ln\frac{n}{B_0 N_c} + B_1\left(\frac{n}{N_c}\right)^{\alpha_1} + B_2\left(\frac{n}{N_c}\right)^{\alpha_2} \tag{2.7a}$$

Here, the expression of parameter α_1, α_2, B_1, B_2 is shown in reference [14]. Figure 2.1 shows a comparison between the actual numerical solution of Eq. 2.6 in open dots and our approximation of Eq. (2.7a) in solid lines. Also shown is the Ariel model in open triangles. As can be seen, our new approximation is in good agreement with the numerical solution in the range of $\phi < 30$ for both LWIR (Fig. 2.1a) and MWIR (Fig. 2.1b) devices. This approximation appears in the same

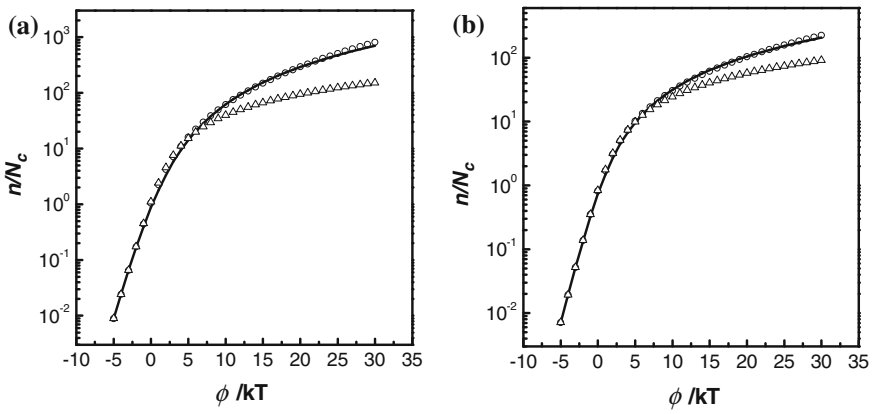

Fig. 2.1 Comparisons of carrier concentration versus reduced Fermi level in the range of $\phi < 30$ for $Hg_{0.8}Cd_{0.2}Te$ (**a**), and $Hg_{0.6}Cd_{0.4}Te$ (**b**) at 80 K calculated by actual numerical solution (*open circle*), Ariel model (*open triangle*), and the approximation Eq. (2.7a) (*solid lines*). Reprinted with permission from Ref. [14] © 2006, Elsevier

form as the Boltzmann's approximation, and is applicable to both analytic and numerical device simulation models.

The hole density p, can be written as an expression similar to Eq. (2.7a) but with generally different coefficients

$$-\phi - \varepsilon_g = \ln\frac{p}{B_{0v}N_v} + B_{1v}\left(\frac{p}{N_v}\right)^{\alpha_{1v}} + B_2 v\left(\frac{p}{N_v}\right)^{\alpha_{2v}} \tag{2.7b}$$

The valence band is parabolic which is equivalent to assuming that the non-parabolicity factor $\alpha = 0$ in Eq. (2.7a). Therefore, we get the valence band coefficient $B_{0v} = 1$, $B_{1v} = 0.944$, $B_{2v} = -0.577$, $\alpha_{1v} = 0.745$, and $\alpha_{2v} = 0.624$ from the expressions for B_0, B_1, B_2, α_1, and α_2 by putting $\alpha = 0$.

We now consider an intrinsic semiconductor where electrical neutrality requires $n = p = n_i$. Using this condition in Eqs. (2.7a) and (2.7b), an implicit expression for n_i can be obtained:

$$\frac{n_i^2}{B_0 B_{0v}}\exp\left[B_1\left(\frac{n_i}{N_c}\right)^{\alpha_1} + B_2\left(\frac{n_i}{N_c}\right)^{\alpha_2} + B_{1v}\left(\frac{n_i}{N_v}\right)^{\alpha_{1v}} + B_{2v}\left(\frac{n_i}{N_v}\right)^{\alpha_{2v}}\right] = N_c N_v \exp(-\varepsilon_g) \tag{2.8}$$

This equation can be solved iteratively for n_i if the other quantities are known.

Subtracting Eq. (2.7b) from Eq. (2.7a) and using the charge neutrality condition, we obtain the following expression for the intrinsic Fermi level ϕ_i of a non-parabolic semiconductor:

$$\phi_i = -\frac{\varepsilon_g}{2} + \frac{1}{2}\ln\left(\frac{B_{0v}N_v}{B_0N_c}\right) + \frac{1}{2}\left[B_1\left(\frac{n_i}{N_c}\right)^{\alpha_1} + B_2\left(\frac{n_i}{N_c}\right)^{\alpha_2} - B_{1v}\left(\frac{n_i}{N_v}\right)^{\alpha_{1v}} - B_{2v}\left(\frac{n_i}{N_v}\right)^{\alpha_{2v}}\right] \tag{2.9}$$

With known n_i, ϕ_i, and with the help of Eqs. (2.7a), (2.7b), (2.8), (2.9), we derive new relations that describe the Fermi level in terms of carrier densities and intrinsic properties:

$$\phi_n - \phi_i = \ln\left(\frac{n}{n_i}\right) + B_1\left[\left(\frac{n}{N_c}\right)^{\alpha_1} - \left(\frac{n_i}{N_c}\right)^{\alpha_1}\right] + B_2\left[\left(\frac{n}{N_c}\right)^{\alpha_2} - \left(\frac{n_i}{N_c}\right)^{\alpha_2}\right] \tag{2.10a}$$

$$\phi_i - \phi_p = \ln\left(\frac{p}{n_i}\right) + B_{1v}\left[\left(\frac{p}{N_v}\right)^{\alpha_{1v}} - \left(\frac{n_i}{N_v}\right)^{\alpha_{1v}}\right] + B_{2v}\left[\left(\frac{p}{N_v}\right)^{\alpha_{2v}} - \left(\frac{n_i}{N_v}\right)^{\alpha_{2v}}\right] \tag{2.10b}$$

The expressions (2.10a, 2.10b) can be solved iteratively for Fermi level E_{fn} and E_{fp}, which are the Fermi energy level of the n-side and the p-side without contact with each other. So we can obtain the built-in potential $V_{bi} = E_{fn} - E_{fp}$ of the p-n junction.

Therefore, with the help of Eqs. (2.7a, 2.7b), non-parabolicity and carrier degeneracy can be adequately modeled by the calculation of built-in potential V_{bi}, intrinsic carrier concentration n_i and intrinsic Fermi level E_i.

Different material compositions can therefore be described by using different carrier density models. In this section, we analyze four carrier density models by considering (I) both the carrier degeneracy and the conduction band non-parabolicity, (II) only the carrier degeneracy, (III) only the conduction band non-parabolicity, and (IV) neither of these two factors.

In Model II, only carrier degeneracy is considered, assuming a parabolic conduction band. The carrier density is given by the following integral expression:

$$n = \frac{2N_c}{\sqrt{\pi}}\int_0^\infty \frac{\sqrt{\varepsilon}}{1 + \exp(\varepsilon - \phi)}\mathrm{d}\varepsilon \tag{2.11}$$

Equation (2.6) will be the same as Eq. (2.11) if the non-parabolicity factor α equals to zero. According to Eq. (2.7a), we can obtain the carrier approximation of Model II:

$$\phi = \ln\frac{n}{N_c} + 0.994\left(\frac{n}{N_c}\right)^{0.745} - 0.577\left(\frac{n}{N_c}\right)^{0.624} \tag{2.12a}$$

The hole density approximation is given by

$$-\phi - \varepsilon_g = \ln\frac{p}{N_v} + 0.994\left(\frac{p}{N_v}\right)^{0.745} - 0.577\left(\frac{p}{N_v}\right)^{0.624} \tag{2.12b}$$

In Model III, the distribution function $f(E)$ can be a Boltzmann function because of carrier non-degeneracy, and only conduction band non-parabolicity is considered. The carrier density is given by the following integral expression:

$$n = \frac{2N_c}{\sqrt{\pi}}\int_0^\infty \varepsilon^{1/2}(1+\alpha\varepsilon)^{1/2}(1+2\alpha\varepsilon)\exp(\phi-\varepsilon)\mathrm{d}\varepsilon \tag{2.13}$$

The approximation of Eq. (2.13) can be given by a modified Boltzmann approximation [18]:

$$n = B_0 N_c \exp(\phi) \tag{2.14a}$$

Likewise, the hole density approximation is given by

$$p = B_{0v} N_v \exp(-\phi - \varepsilon_g) \tag{2.14b}$$

In Model IV, neither carrier degeneracy nor conduction band non-parabolicity is considered. The carrier density is given by the following integral expression:

$$n = \frac{2N_c}{\sqrt{\pi}}\int_0^\infty \sqrt{\varepsilon}\cdot\exp(\phi-\varepsilon)\cdot\mathrm{d}\varepsilon \tag{2.15}$$

The carrier density can be given by a conventional Boltzmann approximation

$$n = N_c \exp(\phi) \tag{2.16a}$$

The hole density approximation is given by

$$p = N_v \exp(-\phi - \varepsilon_g) \tag{2.16b}$$

We present comparisons among the four approximations for carrier density versus Fermi energy in Fig. 2.2. As can be seen from the figure, for both $Hg_{0.8}Cd_{0.2}Te$ (a) and $Hg_{0.6}Cd_{0.4}Te$ (b), comparing with Model I (considering both carrier degeneracy and conduction band non-parabolicity), Model II (considering only carrier degeneracy) underestimates the carrier density, while Model III (considering only conduction band non-parabolicity) and Model IV (considering neither of them) yield significantly larger carrier density at the range of $\phi > 0$ [14]. When Cd composition x changes from 0.2 to 0.4, the difference between Model I and

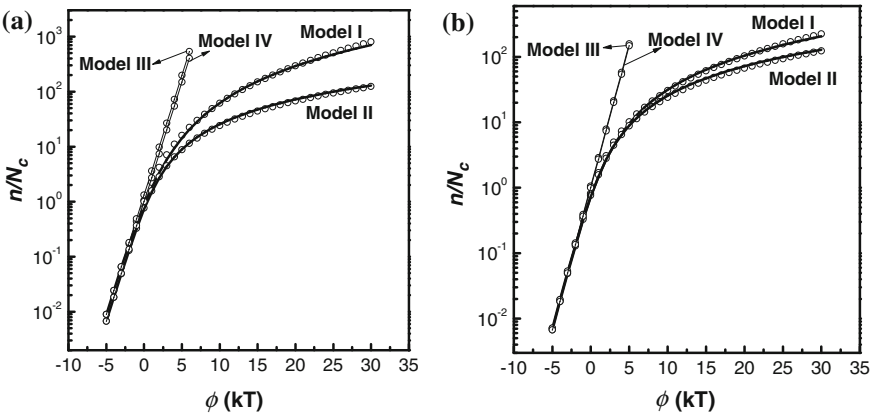

Fig. 2.2 Calculated carrier concentration versus reduced Fermi level with Model I (considering both carrier degeneracy and conduction band non-parabolicity), Model II (considering only carrier degeneracy), Model III (considering only conduction band non-parabolicity), and Model IV (considering neither of them) for $Hg_{0.8}Cd_{0.2}Te$ (**a**), and $Hg_{0.6}Cd_{0.4}Te$ (**b**) at 80 K (*solid lines*). The *open circles* are respective actual numerical solutions. Reprinted with permission from Ref. [14] © 2006, Elsevier

Model II decreases because the increased band gap reduces the non-parabolicity factor α. In addition, one can also see in Fig. 2.2 that the calculations using the four approximations (solid lines) accurately fit the corresponding numerical solutions (open circles) obtained by solving Eqs. (2.6), (2.11), (2.13), and (2.15), respectively, in the range of $\phi < 30$. This indicates that these models can be used in place of a numerical solution to investigate the effects of carrier degeneracy and conduction band non-parabolicity on the simulation of HgCdTe photovoltaic devices.

To further verify the applicability of the above approximations, the measured R_d–V curves from real HgCdTe devices are fitted with the analytic model for device simulation (see Appendix) by using the four models. The samples are LWIR ($x = 0.2323$) and MWIR ($x = 0.2927$) n-on-p diodes fabricated using ion implantation [21]. Their material and device parameters, which are not used as fitting parameters, are summarized in Table 2.1, where x is the Cd composition, T is the measuring temperature, A is the junction area, N_a is the dopant densities of the p-side, and μ_p is the mobility of excess holes.

The fitting parameters are listed in Tables 2.2 and 2.3 for Sample I and Sample II [14], respectively. For Sample II ($x = 0.2927$), the fitting parameter μ_n/τ_n is absent because the diffusion current is insignificant in the dark current for MWIR devices

Table 2.1 Material and device parameters of the two HgCdTe photovoltaic samples

	x	T (*K*)	A (cm^2)	N_a (cm^{-3})	μ_p (cm^2/V s)
Sample I	0.2323	80	2.5×10^{-5}	5.65×10^{15}	813
Sample II	0.2927	80	2.5×10^{-5}	4.66×10^{15}	579

Reprinted with permission from Ref. [14] © 2006, Elsevier

Table 2.2 Fitting parameters obtained by fitting the four models to the measured R_d–V curves of Sample I

Model	μ_p/τ_n ($cm^2/V\ s^2$)	τ_0 (ns)	N_d (cm^{-3})	E_t/E_g	N_t (cm^{-3})
I	1.613×10^{14}	0.154	1.493×10^{16}	0.486	1.659×10^{12}
II	2.128×10^{14}	0.121	1.478×10^{16}	0.488	1.624×10^{12}
III	1.096×10^{14}	0.142	1.564×10^{16}	0.488	1.721×10^{12}
IV	1.248×10^{14}	0.119	1.543×10^{16}	0.488	1.722×10^{12}

Reprinted with permission from Ref. [14] © 2006, Elsevier

Table 2.3 Fitting parameters obtained by fitting the four models to the measured R_d–V curves of Sample II

Model	τ_0 (ns)	N_d (cm^{-3})	E_t/E_g	N_t (cm^{-3})
I	1.488	8.649×10^{17}	0.586	1.302×10^{13}
II	1.389	4.759×10^{17}	0.589	1.174×10^{13}
III	1.492	1.0×10^{19}	0.581	4.398×10^{13}
IV	1.492	1.0×10^{19}	0.581	4.398×10^{13}

Reprinted with permission from Ref. [14] © 2006, Elsevier

at 80 K. It is evident from these tables that these parameters from the four models are different from each other, and the sensitivity of the fitted values of device parameters to the used model is obvious. This implies that the omission of carrier degeneracy and conduction band non-parabolicity brings deviations into the simulation of the HgCdTe device, and the magnitude of the deviations is dependent on the parameters of device and material.

In Fig. 2.3, the solid line denotes the theoretical calculation by using Model I, and the open circles denote the measured data for $x = 0.2323$ (a) and $x = 0.2927$ (b). It can be seen that the theoretical calculation fits the experimental data well. In

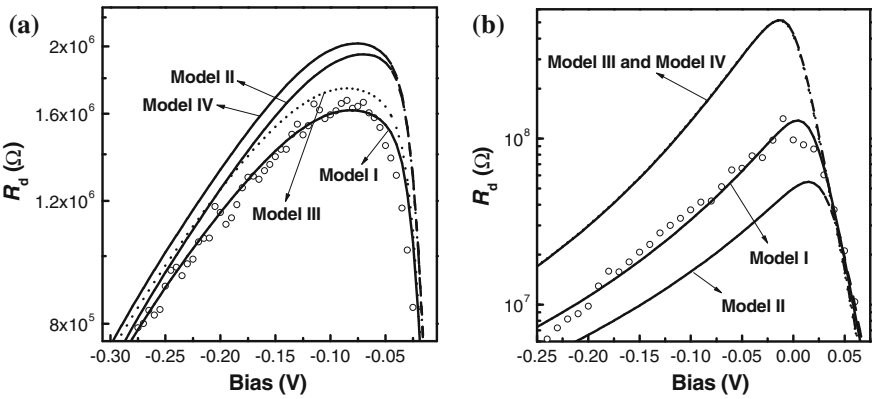

Fig. 2.3 Fitting curves of Model I (*solid lines*) with experimental R_d-V characteristics (*open circles*) and the calculations of Model II (*dashed lines*), III (*dotted lines*) and IV (*dash-dotted lines*) using the parameters in Table 2.1 and the parameters from Model I in Tables 2.2 and 2.3 for Sample I (**a**) and Sample II (**b**) at 80 K. Reprinted with permission from Ref. [14] © 2006, Elsevier

this work, we consider that Model I is a perfect model for HgCdTe, and the fitting parameters from Model I are the authentic parameters for HgCdTe devices. To estimate the deviation of R_d–V characteristics calculated by Model II, III, and IV from those calculated using Model I, all the parameters in Table 2.1 and the parameters for Model I in Tables 2.2 and 2.3 are also employed in the further calculations using Model II, III, and IV. The calculated results are also shown in Fig. 2.3. It is evident from the figure that, compared to Model I, Model IIII predicts larger R_d for LWIR ($x = 0.2323$) and smaller R_d for MWIR ($x = 0.2927$), while Model III and Model IV yield larger R_d for both LWIR and MWIR.

In the above calculations, the differences of the built-in potential $V_{bi,}$ the intrinsic carrier concentration n_i and the intrinsic Fermi level E_i among the three approximations are responsible for the differences in the above three R_d–V curves. It is via these three parameters that the carrier degeneracy and the conduction band non-parabolicity influence the simulation calculations. Therefore, we have calculated V_{bi}, n_i and E_i with various device parameters such as composition and doping level in Model II, III, and IV to estimate their deviation from Model I so that the dark current deviation of Model II, III, and IV from Model I can be further evaluated.

For the purpose of brevity and clarity, the relative deviations of V_{bi}, n_i, and E_i are hereafter referred to simply as A_j/A_1 (A denotes V_{bi}, n_i and E_i, and subscript $j = 1$–4 stands for the four models, respectively). n_i and E_i are dependent on the composition and temperature of the device. Since HgCdTe devices usually work at liquid nitrogen cooled temperatures, we consider a temperature of 80 K in this work. We carried out the calculations for E_{ij}/E_{i1} and n_{ij}/n_{i1} in the composition range of $x = 0.2$–0.4, and the results are shown in Fig. 2.4. Figure 2.5 shows the plots of V_{bij}/V_{bi1} versus the composition x (a) and the doping density of the n-side, N_d (b). The deviations of V_{bij}/V_{bi1} from unity increase with the decreasing x and increasing N_d. The detailed analysis of Figs. 2.4 and 2.5 is shown in the paper of Ref. [14].

Tables 2.4, 2.5, and 2.6 summarize the relative deviations, comparing with Model I, of dark currents in various mechanisms obtained from Model II, III and IV, respectively. For SWIR and MWIR with light doping, the effects of carrier degeneracy and conduction band non-parabolicity on the simulation may be omitted. For LWIR with light doping or those devices with heavy doping, the omission of carrier degeneracy and conduction band non-parabolicity will lead to enormous error in the calculation of the dark current. By using Model I, an accurate simulation can be obtained.

2.2.1.2 Heterostructure Models

The HgCdTe heterojunction has greatly improved the performance of HgCdTe photovoltaic detectors. However, the potential barrier of minority carriers in the heterojunction, prevents the transport of photogenerated minority carriers through the junction, which leads to a decrease in device performance [22–26]. By adjusting the design parameters of the heterojunction, the potential barrier could be decreased

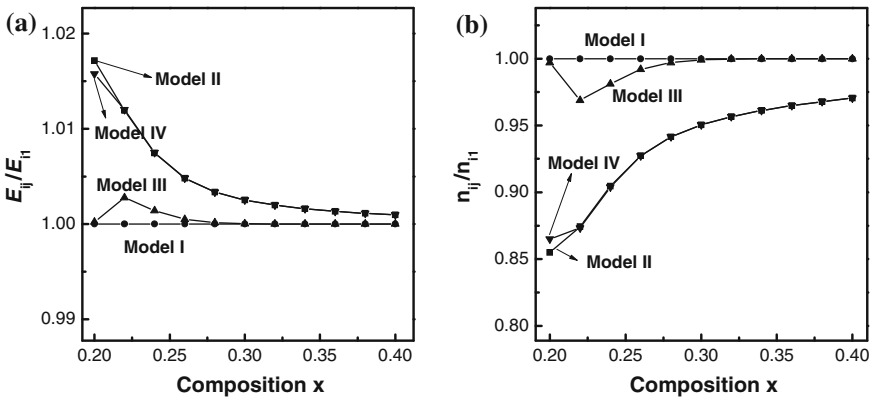

Fig. 2.4 Relative deviations of Model II, III and IV against Model I in intrinsic Fermi level E_{ij}/E_{i1} (**a**) and intrinsic carrier concentration n_{ij}/n_{i1} (**b**) at various composition x (subscript j = 1–4 denotes four models, respectively). Reprinted with permission from Ref. [14] © 2006, Elsevier

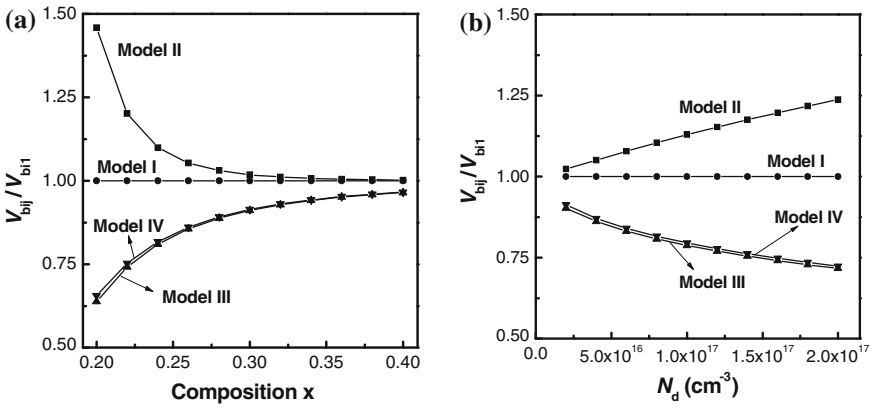

Fig. 2.5 Relative deviations of Model II, III and IV against Model I in built-in potential V_{bij}/V_{bi1} at various composition x (**a**) and various n-side doping density N_d (**b**) (subscript j = 1–4 denotes the four models, respectively). Reprinted with permission from Ref. [14] © 2006, Elsevier

Table 2.4 Relative deviations in various dark currents of Model II (considering only carrier degeneracy) from Model I (considering both carrier degeneracy and conduction band non-parabolicity)

	Light doping		Heavy doping	
	SWIR	LWIR	SWIR	LWIR
I_{diff}	U (<10 %)	U (<30 %)	U (<10 %)	U (<30%)
$I_{g\text{-}r}$	U (<5 %)	U (<20 %)	U (<8 %)	U (<50%)
I_{TAT}	Zero	O (<10 %)	O (<100 %)	O (<350%)
I_{BBT}	Zero	O (<30 %)	O (<1000 %)	O (<5000%)

(*U* denotes 'underestimate', and *O* denotes 'overestimate'.) Reprinted with permission from Ref. [14] © 2006, Elsevier

Table 2.5 Relative deviations in n_i, V_{bi} and various dark currents of Model III (considering only conduction band non-parabolicity) from Model I (considering both carrier degeneracy and conduction band non-parabolicity)

	Light doping		Heavy doping	
	SWIR	LWIR	SWIR	LWIR
I_{diff}	Zero	U (<6 %)	Zero	U (<6 %)
$I_{g\text{-}r}$	Zero	U (<3 %) or O (<10 %)	O (<10 %)	U (<3 %) or O (<60 %)
I_{TAT}	Zero	U (<18 %)	U (<90 %)	U (<99 %)
I_{BBT}	Zero	U (<45 %)	U (<99 %)	U (<99 %)

(*U* denotes 'underestimate', and *O* denotes 'overestimate'). Reprinted with permission from Ref. [14] © 2006, Elsevier

Table 2.6 Relative deviations in n_i, V_{bi} and various dark currents of Model IV (considering neither degeneracy nor non-parabolicity) from Model I (considering both carrier degeneracy and conduction band non-parabolicity)

	Light doping		Heavy doping	
	SWIR	LWIR	SWIR	LWIR
I_{diff}	U (< 10 %)	U (<30 %)	U (<10 %)	U (<30 %)
$I_{g\text{-}r}$	U (< 5 %)	U (<15 %) or O (<8 %)	U (<5 %) or O (<10 %)	U (<15 %) or O (<60 %)
I_{TAT}	Zero	U (<15 %)	U (<95 %)	U (<99 %)
I_{BBT}	Zero	U (<35 %)	U (<99 %)	U (<99 %)

(*U* denotes 'underestimate', and *O* denotes 'overestimate'). Reprinted with permission from Ref. [14] © 2006, Elsevier

and even be eliminated. However, there are many parameters for HgCdTe and the relationships between them are very complicated. Therefore, a reliable theoretical method is urgently needed for the design of the band structure of heterojunctions [27].

Much research has been done in this field. Migliorato and White [28] considered the interdiffusion effect of both composition and doping, and calculated the band structure of HgCdTe/CdTe heterojunction. Bratt and Casselman [29] developed the MW model, which can be suitable for calculating the heterojunction with different composition of $Hg_xCd_{1-x}Te$. However, these two models are both based on common anion rule, namely assuming that there was no discontinuity of the valence band, and their calculations both neglected the degeneracy of the carrier and the non-parabolic conduction band of HgCdTe. Then, after Madrasz and Szmulowiz [30–32] introduced the Fermi–Dirac integral based on these two models, the following characteristics of HgCdTe can be included in the calculation of band structure: (1) the carrier degeneracy; (2) the non-parabolic conduction band; (3) the valence band discontinuity. However, the Fermi–Dirac integral without any approximation greatly increases the total computing time, which limits the use of the model and makes it only suitable for the solution of the Poisson equation under

equilibrium. The research of Bratt and Casselman [29] demonstrated that the band structure of heterojunctions can be optimized by controlling the positions of the *p-n* junction and the Cd composition junction, but the work of Madrasz and Szmulowiz [30–32] assumed that the position of the *p-n* junction coincides with that of the Cd composition junction and ignored the effect of relative position between the *p-n* junction and the Cd composition junction on the band structure. Moreover, recent work indicated that there was charge at the interface of a heterojunction [33, 34]. It was stated that the interface charge was usually caused by a discontinuity within the lattice and the process technology. Though the lattice discontinuity between HgCd and CdTe is less than 0.3 %, the fixed charge also exists at the interface because of the different polar intensities of HgCd and CdTe. Therefore, the density of interface charge, which can be either positive or negative, is very hard to be controlled and extracted in general cases [33]. The density of charge at the interface between HgCd and CdTe is about $\pm 1 \times 10^{12}$ cm^{-2}. However, the density of charge at the interface of HgCdTe with different compositions varies linearly with the gradient of the Cd composition [35]. The influence of this magnitude of interface charge on band structure is not ignorable, so it is very necessary to study the influence of interface charge in the design of a heterojunction structure. In this section, the following three aspects are considered in the physical model: (1) the carrier degeneracy; (2) the non-parabolic conduction band; (3) the valence band discontinuity. Based on the approximation model of carriers in Sect. 2.2.1.1, the Fermi–Dirac integral can be calculated rapidly. Therefore, it not only satisfies the demand for computational speed, but also enhances the accuracy of the physical model. As a result, a feasible method can be proposed for weakening the effect of interface charge.

In the Fermi–Dirac integral calculation, z is set for the location, $0 < z < L$, L is the length along the growth orientation of the device, and $L = 4$ μm. Assuming that the valance band at $z = 0$ is a zero energy point, then the Poisson equation can be expressed as:

$$\nabla^2\psi = -\frac{q}{\varepsilon}\left[p - n + N_{\mathrm{d}}^{+} - N_{\mathrm{a}}^{-} + Q_{\mathrm{e}}\right] - \frac{1}{\varepsilon}\nabla\psi\nabla\varepsilon \tag{2.17}$$

where Ψ is electrostatic potential, ε is the permittivity, p is the hole density, n is the electron density, N_{d}^{+} is the ionized donor density, N_{a}^{-} is the ionized acceptor density, Q_{e} is the interface charge profile. It is assumed that the donor and acceptor are both fully ionized during the calculation.

The boundary conditions can be expressed as:

$$\psi(0) = 0 \tag{2.18}$$

$$\psi(L) = \phi(L) - \phi(0) + \Delta E_{\mathrm{v}}(L) \tag{2.19}$$

where ϕ is counted by iteration according to formula (2.3) and charge neutrality condition, ΔE_{v} is the valence band discontinuity.

Assumed that ΔE_v^0 is the valence band discontinuity of the HgTe/CdTe heterojunction [36, 37], and $\Delta E_v^0 = 0.35$ eV. Since the valence band discontinuity of the HgCdTe/HgCdTe heterojunction is proportional to the difference of the Cd composition (Δx), $\Delta E_v = \Delta x \cdot \Delta E_v^0$. Because of the interdiffusion effect of both composition and doping, there is a composition-graded region around the composition junction and a doping-graded region around the *p-n* junction respectively.

For a graded composition junction, assuming that material A layer is followed by material B layer along the z direction, then the profile of Cd composition can be described by an error function of z:

$$x(z) = x_B + 0.5 \times (x_A - x_B) \times \mathrm{erfc}\left(\frac{z - z_c}{0.5W_c}\right) \tag{2.20}$$

where x_A and x_B are the Cd composition of A and B HgCdTe material respectively, W_c is the width of graded composition, z_c is the location of composition junction, in the later calculations, z_c is fixed at $z = 2.0$ μm. $z = 0$ is the reference point, $\Delta E_v = \Delta x \cdot \Delta E_v^0$, then, the discontinuity of valence band along z direction $\Delta E_v(z) = [x(0) - x(z)] \cdot \Delta E_v^0$, put formula (2.20) into it:

$$\Delta E_v(z) = (x_A - x_B) \cdot \Delta E_v^0 \left[1 - \frac{1}{2}\mathrm{erfc}\left(\frac{z - z_c}{0.5W_c}\right)\right] \tag{2.21}$$

The doping profile along the z direction can be described by an error function of the coordinate z:

$$N(z) = N(L) + \frac{N(0) - N(L)}{2} \cdot \mathrm{erfc}\left(\frac{z - z_B}{0.5W_B}\right) \tag{2.22}$$

where $N = N_d - N_a$, W_B is the width of graded doping, and z_B is the location of *p-n* junction. In the design of a HgCdTe heterojunction, W_B is 0.01 μm.

The profile of the interface charge along the z direction is described by a Gauss function:

$$Q_e(z) = Q \cdot \exp\left[-\frac{(z - z_Q)^2}{2\sigma^2}\right] \tag{2.23}$$

In the design of a HgCdTe heterojunction, set the maximum density (Q) of interface charge as a parameter for calculation. The interface charge is mainly produced from the lattice discontinuity between two materials on both sides of the heterojunction. Therefore, the profile of the interface charge is related to the location and width of the composition junction. Assuming that the center position of the function (z_Q) coincides with the position of the composition junction (z_c), then the full width half maximum (σ) is equal to $0.25W_c$.

Since the p and n in Eq. (2.17) are a function of the variable Ψ, the Poisson equation is nonlinear. However, the Poisson equation can be disposed discretely and linearly by the finite difference method, and then it can be solved by Newton iteration.

The valance band and conduction band can be expressed as:

$$E_{\mathrm{v}}(z) = \Delta E_{\mathrm{v}}(z) - q \cdot \psi(z) \tag{2.24}$$

$$E_{\mathrm{c}}(z) = E_{\mathrm{v}}(z) + E_{\mathrm{g}}(z) \tag{2.25}$$

For convenience, the p-n junction of wider (narrower) bandgap p-type HgCdTe material on narrower (wider) bandgap n-type HgCdTe material is set as "Pn" and "pN" structure respectively.

2.2.2 *Design of Heterojunctions HgCdTe Infrared Detectors*

The mainstream of HgCdTe detectors nowadays are homojunctions. However, HgCdTe devices tend to be manufactured by heterojunctions with the evolution of fabrication processes. Wide band gap material can decrease the tunneling rate of carriers through the junction, which results in the decrease of the dark current and noise of devices [23]. Therefore, the performance of a device with a heterojunction structure can be greatly improved. However, the structure of heterojunction is more complicated than homojunction, which makes the analysis of heterojunction devices become more difficult. For heterojunction devices, it is difficult for us to analyze the device's performance by using solely an analytical model. Therefore, a numerical model is needed to be proposed for design of heterojunction devices.

2.2.2.1 The Calculation of Band Structure in Heterojunction Devices

The influence of the p-n junction location (z_{B}) on the band structure is shown in Figs. 2.6 and 2.7. The calculated results are in good agreement with Figs. 1 and 5 in Ref. [28], which demonstrates the accuracy of the approximation Eqs. (2.7a, 2.7b). The comparison of the band structures (with no valance discontinuity) with different z_{B} is shown in Fig. 2.8a, it is shown that the potential barrier decreases and finally disappears when the p-n junction enters into narrow band gap material. This conclusion is in good agreement with BC model. However, the effect of valance discontinuity on the band structure is shown in Fig. 2.8b. It is shown that a potential well appears at the same time, and the potential well increases when the p-n junction enters into narrow band gap material. The appearance of the potential well also degrades the detector performance, so the entrance of the p-n junction into narrow band gap material should be avoided in this situation.

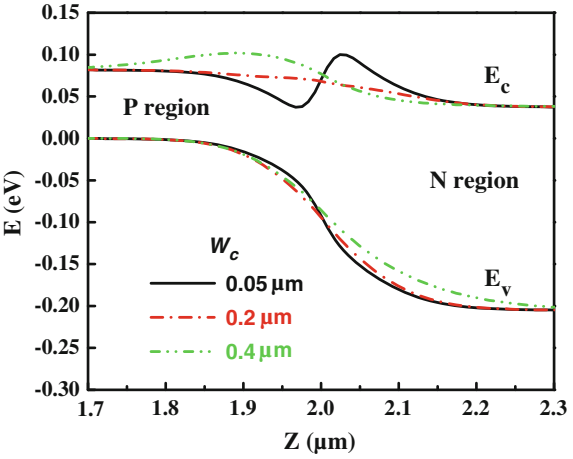

Fig. 2.6 The band structure profile of pn structure with different composition graded width W_c at 77 K. Where $x_n = 0.3$, $x_p = 0.2$, $N_a = N_d = 5 \times 10^{15}$ cm^{-3}. Redrawn from Ref. [27], Copyright 2006, The Chinese Physical Society

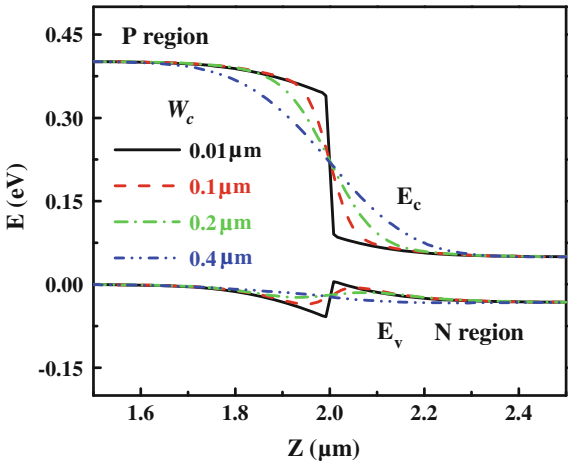

Fig. 2.7 The band structure profile of Pn structure with different composition graded width W_c at 77 K. Where $x_n = 0.2$, $x_p = 0.4$, $N_a = N_d = 1 \times 10^{15}$ cm^{-3}. Redrawn from Ref. [27], Copyright 2006, The Chinese Physical Society

For the Pn structure, Figs. 2.8 and 2.9 illustrate that the potential barrier of valance band will decrease, and a potential well will appear when the *p-n* junction enters into narrow band gap region. When the *p-n* junction enters into a wide band gap region, the potential well of valance band becomes shallow, and the height of potential barrier increases. For the pN structure, when the *p-n* junction enters into narrow band gap region, the potential barrier of conduction band decreases, and a potential well appears. When the *p-n* junction enters into a wide band gap region, the potential well of the conduction band becomes shallow, and the height of potential barrier increases.

(1) The influence of the interface charge density (Q) on the band structure in pn device is shown in Fig. 2.10. When the interface charge is positive, the potential barrier of conduction band electrons decreases. When interface

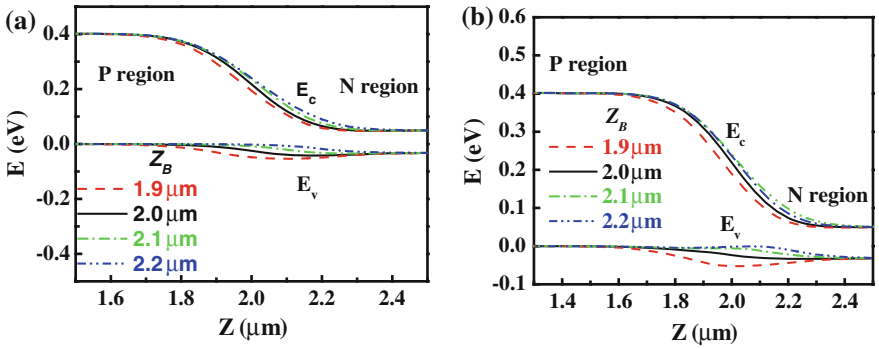

Fig. 2.8 The band structure profile of Pn structure with different *p-n* junction location (z_B) at 77 K, Where $x_n = 0.2$, $x_p = 0.4$, $N_a = N_d = 1 \times 10^{15}$ cm^{-3}, $W_c = 0.4$ μm. **a** The valance discontinuity $\Delta E_v^0 = 0$ eV, **b** The valance discontinuity $\Delta E_v^0 = 0.35$ eV. Redrawn from Ref. [27], Copyright 2006, The Chinese Physical Society

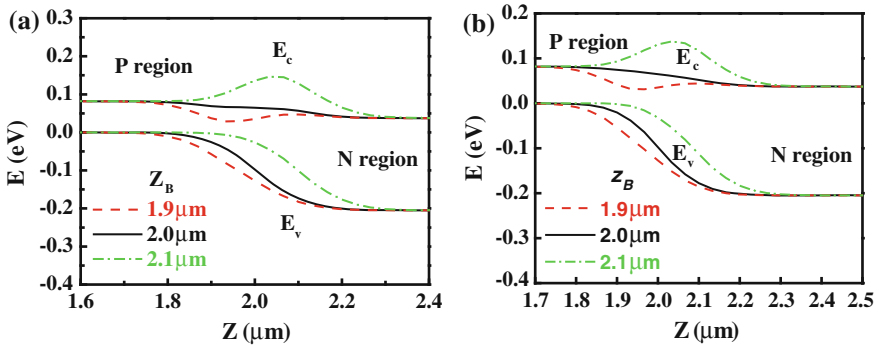

Fig. 2.9 The band structure profile of pN structure with different *p-n* junction location (z_B) at 77 K, Where $x_n = 0.3$, $x_p = 0.2$, $N_a = N_d = 5 \times 10^{15}$ cm^{-3}, $W_c = 0.2$ μm. **a** The valance discontinuity $\Delta E_v^0 = 0$ eV, **b** The valance discontinuity $\Delta E_v^0 = 0.35$ eV. Redrawn from Ref. [27], Copyright 2006, The Chinese Physical Society

charge is negative, the potential barrier of electrons in the conduction band will increase. For a Pn device, the appearance of the interface charge can influence the shape of valance band. When the interface charge is positive, the potential barrier of holes in the valance band will increase. When the interface charge is negative, the potential barrier of holes in the valance band will decrease, and the potential well of holes will increase.

(2) The optimization of parameter z_B and Q. Figure 2.11 shows the band profile of pN and Pn structures with different position (z_B). For the pn structure, when the interface charge is negative, the potential barrier of electron in conduction band can be decreased by adjusting the position of *p-n* junction. However, a

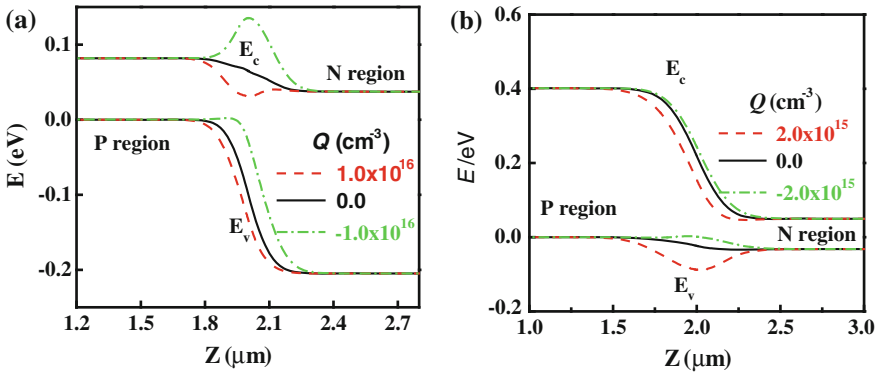

Fig. 2.10 The band profiles with different Q at 77 K. **a** pN structure, where $x_n = 0.3$, $x_p = 0.2$, $N_a = N_d = 5 \times 10^{15}$ cm^{-3}, and $W_c = 0.2$ μm, **b** Pn structure, where $x_n = 0.2$, $x_p = 0.4$, $N_a = N_d = 1 \times 10^{15}$ cm^{-3}, and $W_c = 0.4$ μm. Redrawn from Ref. [27], Copyright 2006, The Chinese Physical Society

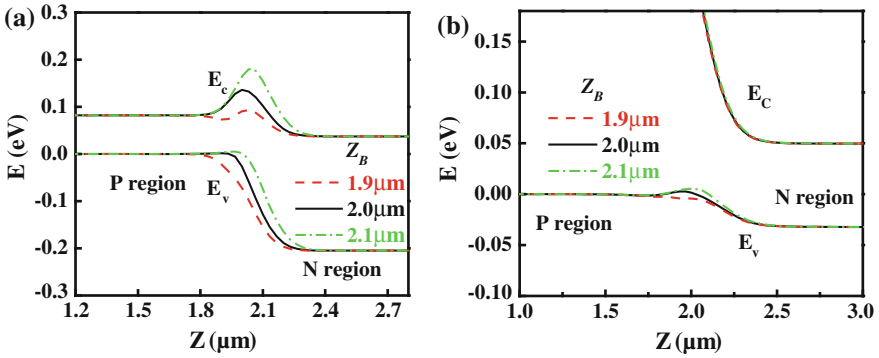

Fig. 2.11 The band profiles with different z_B at 77 K when interface charge is negative. **a** pN structure, where $x_n = 0.3$, $x_p = 0.2$, $N_a = N_d = 5 \times 10^{15}$ cm^{-3}, $W_c = 0.2$ μm, and $Q = -1 \times 10^{16}$ cm^{-3}, **b** Pn structure, where $x_n = 0.2$, $x_p = 0.4$, $N_a = N_d = 1 \times 10^{15}$ cm^{-3}, $W_c = 0.4$ μm, and $Q = -2 \times 10^{15}$ cm^{-3}. Redrawn from Ref. [27], Copyright 2006, The Chinese Physical Society

potential well will appear when the potential barrier decreases to a certain value. For the Pn structure, the potential well of holes in the valance band can also be decreased by adjusting the position of *p-n* junction.

When the interface charge is positive, the band profile of pN and Pn structures with different position (z_B) is shown in Fig. 2.12. For the pN structure, the potential well of electrons in the conduction band can be decreased by adjusting the position of *p-n* junction. For the Pn structure, the potential barrier of hole in valance band can also be decreased by adjusting the position of *p-n* junction. However, when the potential barrier decreases to a certain value, a potential well will appear.

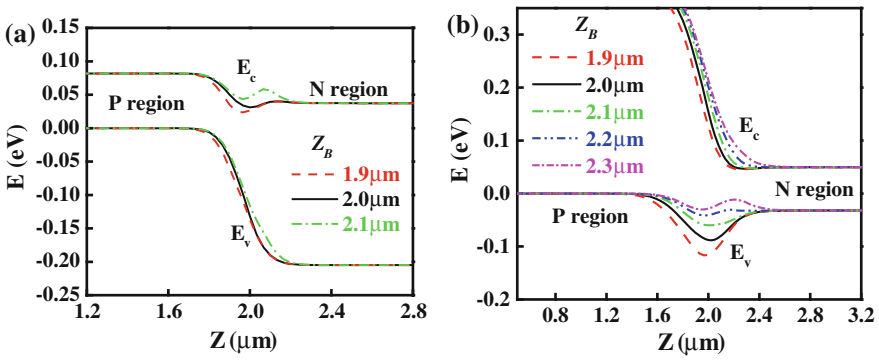

Fig. 2.12 The band profiles with different z_B at 77 K when interface charge is positive. **a** pN structure, where $x_n = 0.3$, $x_p = 0.2$, $N_a = N_d = 5 \times 10^{15}$ cm^{-3}, $W_c = 0.2$ μm, and $Q = 1 \times 10^{16}$ cm^{-3}, **b** Pn structure, where $x_n = 0.2$, $x_p = 0.4$, $N_a = N_d = 1 \times 10^{15}$ cm^{-3}, $W_c = 0.4$ μm, and $Q = 2 \times 10^{15}$ cm^{-3}. Redrawn from Ref. [27], Copyright 2006, The Chinese Physical Society

Therefore, the effect of z_B on the band structure is likely to be relatively limited, and is determined by the density of the interface charge. When the density of the interface charge is low enough, the potential barrier or well can be eliminated by optimizing the position of *p-n* junction. However, when the interface charge density is greater than a certain value, fine-tuning the position of *p-n* junction can only decrease the potential barrier or potential well. Additionally, a further change in the position of the composition junction will generate other potential barriers or potential wells. The optimal design of parameter z_B and Q can be obtained from Figs. 2.11 and 2.12. For the pN structure, when the interface charge is negative, the position of the *p-n* junction should be near the narrow band gap material. For the *Pn* junction, when the interface charge is positive, the position of the *p-n* junction should be near the wide band gap material.

2.2.2.2 The Influence of Potential Barrier on the Device Performance

As above mentioned, the potential barrier of the heterojunction will degrade the performance of the device. The influence of the potential barrier on the transport of minority carriers in P^+-on-*n* heterojunctions was studied by experimental and theoretical methods [24]. It was discovered that when the height of potential barrier was $2kT$, the quantum efficiency decreased to 95 %, when the height of potential barrier was $4.5kT$, the quantum efficiency decreased to 50 %. However, only the optical characteristic of the device was studied for the potential barrier of the heterojunction. The electrical characteristics of the device were neglected. The influence of the position of the *pn* junction in relation to the composition junction on band structure was studied [26, 27]. In the above section, the change of graded length of composition in heterojunction can produce the potential barrier.

Therefore, this section will analyze quantitatively the influence of the graded length of the composition on the device performance.

In the previous section, Eqs. (2.7a, 2.7b) for carrier density has been established, which is very suitable for HgCdTe material. The form of this equation is similar to the Boltzmann approximation equation. Therefore, it is suitable for the analytical model, as well as the numerical model. However, as this equation is a transcendental equation, there are too many iterations in numerical calculation, which make the convergence of the solution be worse and the computing time become longer. In order to solve these problems, the approximation model of carrier density should be proposed as a form of non-transcendental equation.

For a given ϕ, many analytical approximation models have been reported to solve the density of electrons [27, 38]. The revised Boltzmann approximation model only considered the non-parabolic approximation, which is not suitable for the degenerate case. The Ehrenberg model is not suitable for the highly degenerate case, and the Sommerfeld model is only suitable for the highly degenerate case. The results of these models and the accurate numerical Eq. (2.6) are shown in Fig. 2.13. It illustrates that when $\phi < -2$, the result of the Ehrenberg model is in agreement with the numerical result, and when $\phi > 5$, the result of the Sommerfeld model is in agreement with the numerical result. In order to fit the result of the carrier approximation model with that of numerical integral in the range of $\phi < 30$, it is very necessary to modify the Sommerfeld model and add it into Ehrenberg model:

$$n = \frac{B_0^* N_c \exp(\phi)}{1 + 0.75 B_0^* B_1^* \exp(\phi)} + \frac{\sqrt{2}}{3\sqrt{\pi}} N_c [(\phi + |\phi|) \cdot (1 + \alpha\phi)]^{3/2} \tag{2.26}$$

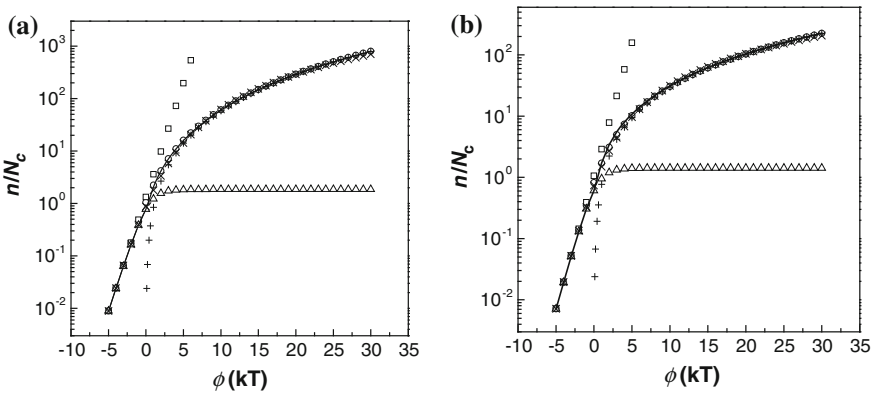

Fig. 2.13 The curve of carrier density versus Fermi level calculated by several approximation model of carrier density and numerical integral in **a** $Hg_{0.8}Cd_{0.2}Te$ and **b** $Hg_{0.6}Cd_{0.4}Te$ at 80 K. *Open circle* is solved by accurate numerical integral, *open square* is solved by the revised Boltzmann approximation, *open triangle* is solved by Ehrenberg model, *plus* is solved by Sommerfeld model, *cross* is the calculation of Eq. (2.3), *solid line* is the approximation of carrier density solved by Eqs. (2.10a, 2.10b)

The results of Eqs. (2.2), (2.3), and (2.26) are shown in Fig. 2.13. It illustrates that Eq. (2.26) is fitted well with Eqs. (2.2) and (2.3) in the range of $\phi < 30$. Therefore, Eq. (2.3) can be replaced by Eq. (2.26).

The hole density of HgCdTe can be expressed as:

$$p = \frac{2N_v}{\sqrt{\pi}} F_{1/2}(-\phi - \varepsilon_g) \tag{2.27}$$

where $F_{1/2}(\eta)$ is 1/2 of Fermi level [39]:

$$F_{1/2}(\eta) \approx \frac{2\sqrt{\pi}}{3\sqrt{\pi}a^{-3/8} + 4\exp(-\eta)} \tag{2.28}$$

where $a = \eta^4 + 33.6\eta\{1-0.68\exp[-0.17(\eta + 1)^2]\} + 50$. When η varies from $-\infty$ to $+\infty$, the relative error between the above analytical model and accurate calculation is not less than 0.4 %.

Since the form of Eqs. (2.26) and (2.27) are not similar with that of Boltzmann approximation equations, the equations are rewritten as [40]:

$$n = n_{i,\text{eff}} \cdot \gamma_n \cdot \exp\left(\frac{E_{fn} - E_i}{kT}\right) \tag{2.29}$$

$$p = n_{i,\text{eff}} \cdot \gamma_p \cdot \exp\left(\frac{E_i - E_{fp}}{kT}\right) \tag{2.30}$$

where γ_n and γ_p is the function of η_n and η_p, respectively:

$$\gamma_n = \frac{n}{N_c}\exp(-\eta_n) \tag{2.31}$$

$$\gamma_p = \frac{p}{N_v}\exp(-\eta_p) \tag{2.32}$$

$$\eta_n = \frac{E_{fn} - E_c}{kT} \tag{2.33}$$

$$\eta_p = \frac{E_v - E_{fp}}{kT} \tag{2.34}$$

According to Eqs. (2.29) and (2.30) of carrier density, a solution of the one-dimensional HgCdTe *pn* junction is obtained by finite difference method. The detailed process and method of one-dimensional simulation refers to the literature [41–43]. In order to verify the validity of program, the calculated result was compared with the solution obtained using the commercial software DESSIS. The one-dimensional schematic of HgCdTe device is shown in Fig. 2.14, and the relevant material and structural parameters are listed in Table 2.7.

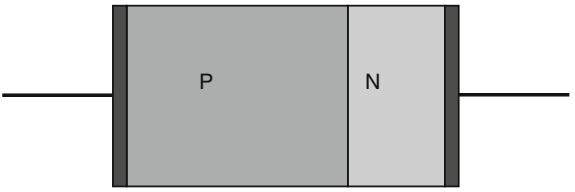

Fig. 2.14 One-dimensional simulated schematic of HgCdTe device

Table 2.7 Relevant material and structure parameters of one-dimensional HgCdTe device

Composition x	0.22
Temperature	77 (K)
SRH lifetime	10 (ns)
Doping concentration of N region	1×10^{16} (cm^{-3})
Doping concentration of P region	8×10^{15} (cm^{-3})
Thickness of N region	1 (μm)
Thickness of P region	9 (μm)
Junction area	50×50 (μm^2)

The result of locally produced software is in good agreement with that of DESSIS software, which demonstrates the validity of the program (Fig. 2.15). However, only the thermal effects, namely diffusion current and generation–recombination current are considered in the dark current aspects of this program. In narrow band gap semiconductors such as HgCdTe, the device performance is usually limited by the tunneling mechanism. Therefore, to exactly calculate the electrical characteristics of the HgCdTe heterojunction, the effects of trap-assisted tunneling and band-to-band tunneling should be added into the numerical model, where the two models are integrated into the continuity equation as generation–recombination terms. This revised recombination rate in the continuity equation of the numerical model is:

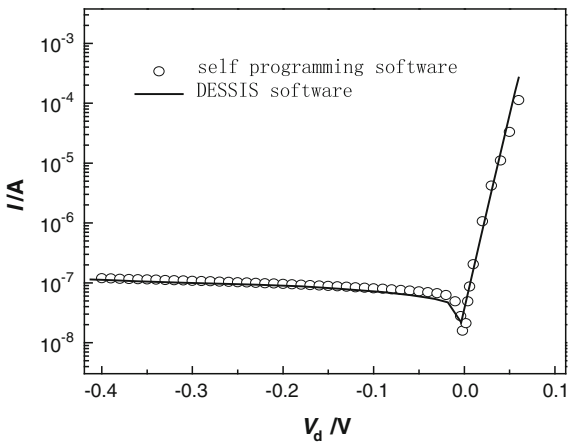

Fig. 2.15 Comparable results of locally developed software and commercial DESSIS software

$$U = U_{\text{rad}} + U_{\text{aug}} + U_{\text{SRH}} + U_{\text{tat}} + U_{\text{bbt}} \tag{2.35}$$

where U_{rad} is the Radiation recombination, U_{aug} is the Auger recombination, and U_{SRH} is the Shockley–Read–Hall (SRH) recombination [44]. U_{tat} and U_{bbt} is the recombination rate of trap-assisted tunneling and band-to-band tunneling respectively. The analytical expressions of U_{tat} and U_{bbt} are expressed as follows:

$$U_{\text{tat}} = A_{\text{tat}} \cdot E \cdot \exp\left(-\frac{B_{\text{tat}}}{E}\right) \tag{2.36}$$

$$U_{\text{bbt}} = A_{\text{bbt}} \cdot E^2 \cdot \exp\left(-\frac{B_{\text{bbt}}}{E}\right) \tag{2.37}$$

$$A_{\text{tat}} = -\frac{\pi^2 q N_{\text{t}} m_{\text{e}}^* M^2}{1.62 \cdot h^3 (E_{\text{g}} - E_{\text{t}})} \tag{2.38}$$

$$B_{\text{tat}} = \frac{1.62 \cdot \sqrt{3} E_{\text{g}}^2 F(a)}{8\sqrt{2} q P} \tag{2.39}$$

$$A_{\text{bbt}} = -\frac{q^2 \sqrt{2 m_{\text{e}}^*}}{1.62^2 \cdot 4\pi^3 \hbar^2 \sqrt{E_{\text{g}}}} \tag{2.40}$$

$$B_{\text{bbt}} = \frac{1.62 \cdot \pi \sqrt{m_{\text{e}}^*/2} E_{\text{g}}^{3/2}}{2q\hbar} \tag{2.41}$$

In the above equations, the electric field (E) of depletion region is the average electric field because the depletion region approximation is considered in the analytical model. However, the depletion region approximation is not suitable for the numerical model. Therefore, a factor of 1.62 [45] is introduced for equivalent calculating.

The R–V curve calculated by the analytical model compared with that calculated by the numerical model is shown in Fig. 2.16, where R_{sz} is the dynamic resistance of the numerical model. It is shown that the R–V curve of the analytical model is in good agreement with that of the numerical model. However, the extracted parameters of these models are listed in Table 2.8 which illustrate that there is quite a difference between them, mainly caused by the depletion region approximation.

In order to study the influence of the graded length of composition on the performance of devices, a one-dimensional program is applied for the characterization of the pN and Pn structures (see Fig. 2.7). The parameters are listed in Table 2.9. The R–V curves of pN and Pn structures with different graded lengths of composition are calculated by 1D simulation program, as shown in Fig. 2.17. The corresponding R–V curve of the homojunction is marked with the composition of 0.

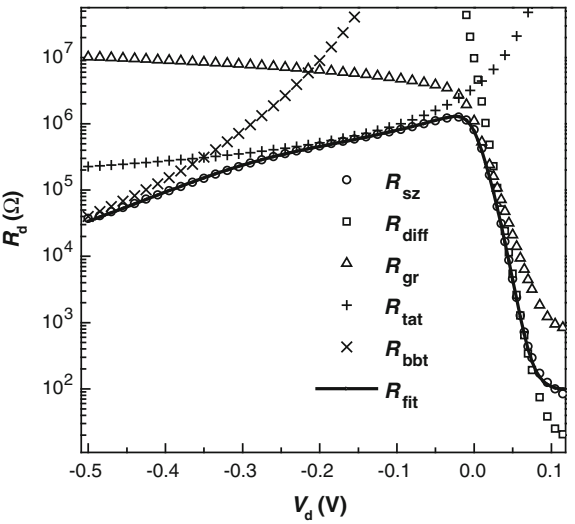

Fig. 2.16 Fitted results of *R–V* curve of self programming software with that of analytical model

Table 2.8 Parameters of HgCdTe device in analytical model and numerical model

	Analytical model	Numerical model
Composition x	0.2323	0.2323
Temperature (K)	77.3	77.3
Doping concentration of P region (cm^{-3})	9×10^{15}	9×10^{15}
Electron mobility (cm^2/V s)	20,000	20,000
Hole mobility (cm^2/V s)	600	600
Hole effective mass	0.55	0.55
Thickness of N region	1 (μm)	–
Thickness of P region	9 (μm)	–
Junction area (μm^2)	28×28	28×28
Doping concentration of N region (cm^{-3})	2×10^{16}	2.044×10^{16}
SRH lifetime in neutral region (ns)	0.5	0.606
SRH lifetime in depletion region (ns)	0.5	0.602
Trap level (E_g)	0.645	0.602
Trap concentration (cm^{-3})	2×10^{12}	1.426×10^{12}
Series resistance (Ω)	–	79.3

It demonstrates that the dynamic resistances of a pN structure with different graded lengths are almost the same under a forward bias. However, the dynamic resistance of a *Pn* heterojunction is bigger than that of homojunction. This is mainly because that the minority lifetime of the *p* region is very short, and the dark current is dominated by diffusion current under a forward bias. Diffusion current mainly is produced in the *p* region, and has almost no dependence on the junction region. Therefore, the length of graded composition has little effect on the dynamic

Table 2.9 Parameters used in one-dimensional simulation program

	Pn structure	Pn structure
Temperature (K)	77	77
Junction area (μm^2)	28 × 28	28 × 28
SRH lifetime (ns)	5	500
Trap level (E_g)	E_i	E_i
Trap concentration (cm^{-3})	2×10^{12}	2×10^{12}
Hole effective mass	0.55	0.55
Composition of *N* region *x*	0.3	0.2
Composition of *P* region *x*	0.2	0.4
Doping concentration of *N* region (cm^{-3})	5×10^{15}	1×10^{15}
Doping concentration of *P* region (cm^{-3})	5×10^{15}	1×10^{15}
Thickness of *N* region (μm)	1	9
Thickness of *P* region (μm)	9	1
Electron mobility (cm^2/V s)	1×10^5	1×10^5
Hole mobility (cm^2/V s)	600	600

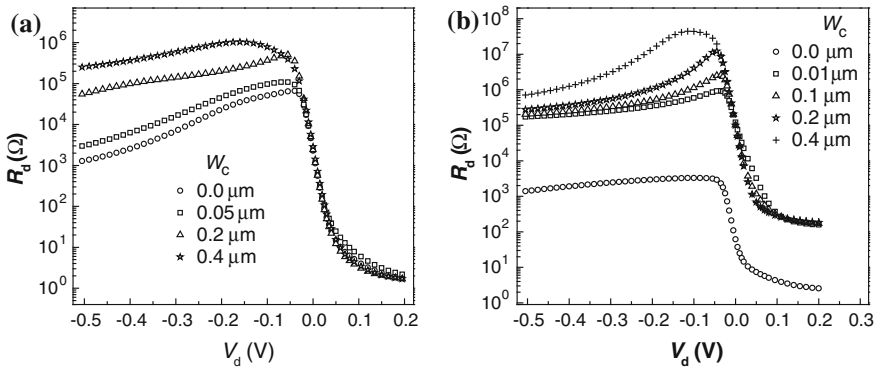

Fig. 2.17 *R–V* curve with different W_c. **a** pN structure, **b** Pn structure. $W_c = 0$ represents the result of homojunction

resistance under a forward bias. However, for a pN structure, the minority lifetime of the *p* region is long, and the dark current is dominated by recombination current under a forward bias. Therefore, the length of the graded composition has a great effect on the dynamic resistance under a forward bias. Moreover, the dynamic resistance of these two structures both increase with the length of graded composition under a reverse bias. At present, infrared detectors usually work under a reverse bias. Therefore, the longer the length of graded composition, the better is the electrical performance. However, the detectivity of the detector is not only proportional to dynamic resistance (*R*), but also to the quantum efficiency (η). In

order to study the influence of the potential barrier on device performance, quantum efficiency η, namely the optical characteristics, should be considered and calculated.

In the numerical model, the generation–recombination rate in the continuity equation can be expressed as:

$$U = U_{\text{rad}} + U_{\text{aug}} + U_{\text{SRH}} + U_{\text{tat}} + U_{\text{bbt}} - G_{\text{photo}} \tag{2.42}$$

where the photogenerated term G_{photo} is:

$$G_{\text{photo}}(z) = Q \cdot (1 - r) \cdot \alpha(z) \cdot \exp\left[- \int_0^z \alpha(t) \mathrm{d}t \right] \tag{2.43}$$

where Q is the power density of the incident light, and r is the reflectance coefficient, $\alpha(z)$ is the absorption coefficient.

The photoresponse curve of two heterojunction structures with different lengths of grade composition is shown in Fig. 2.18, where the incident light power is 0.01 W/m^2 [27]. According to the electrical characteristics shown in Fig. 2.17 and the optical characteristics shown in Fig. 2.18, the influence of the potential barrier on the device performance can be analyzed quantitatively. It is known that the detectivity of device is proportional to $\eta \cdot \sqrt{RA}$, so $\eta \cdot \sqrt{RA}$ can be used to characterize the performance of detectors. The normalized quantum efficiency (η) and dynamic resistance (R) with the length of grade composition in two heterojunction structures are shown in Fig. 2.19, where the bias voltage is −0.05 V. The normalized $\eta \cdot \sqrt{RA}$ in two heterojunction structures with the length of grade composition is shown in Fig. 2.20. For a pN structure, it demonstrates that the performance of the heterojunction device is the best when the length of grade composition is 0.2 μm. For a Pn structure, the performance of the heterojunction device is the best when the length of grade composition is 0.4 μm. This conclusion is consistent with the optimal design of band structure shown in Fig. 2.7.

2.2.3 Design of Long Wavelength HgCdTe Detectors

Currently, the study of $Hg_{1-x}Cd_xTe$ detectors is mainly based on various one-dimensional analytical models. Though the physical meaning of each variable is clear, the description of the devices is not very accurate. The real device is always a three-dimensional *pn* junction, where the lateral current and electric field cannot be analyzed by a one-dimensional model. For $Hg_{1-x}Cd_xTe$ devices with two contacts on the same side, this problem is more complex, and is beyond the theoretical framework of a one-dimensional analytical model. However, it is very complicated to establish the integrated three-dimensional model. Lateral current and the electric

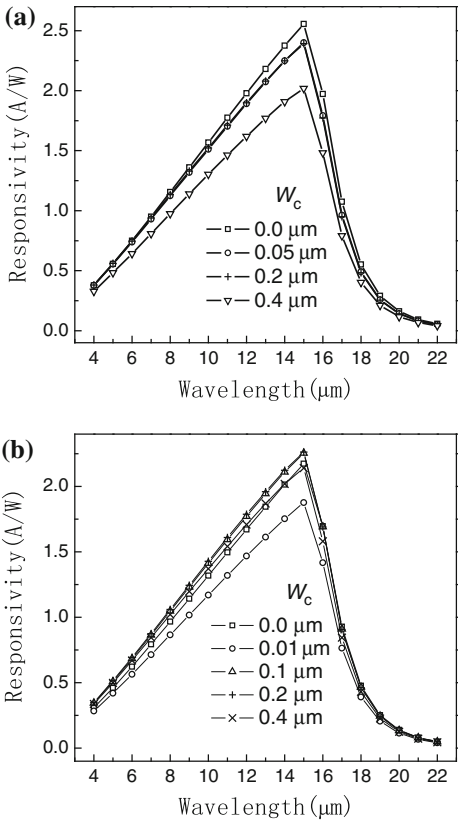

Fig. 2.18 Photo responsivity with different width of graded composition W_c. **a** Pn structure, **b** Pn structure

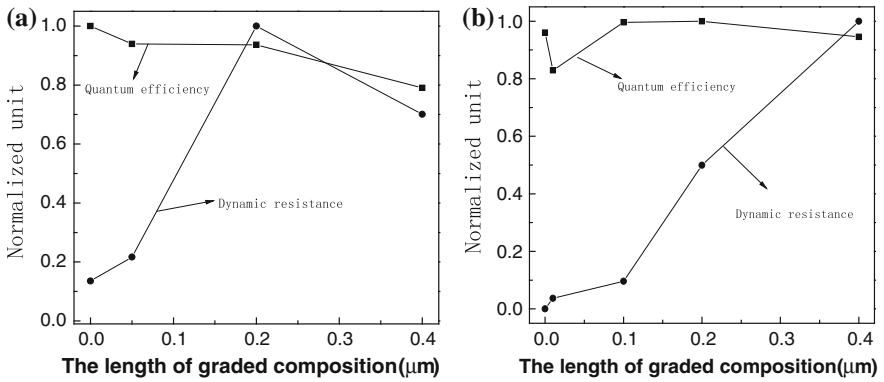

Fig. 2.19 Normalized quantum efficiency and dynamic resistance with the length of graded composition in two heterojunction structures. **a** pN structure, **b** Pn structure

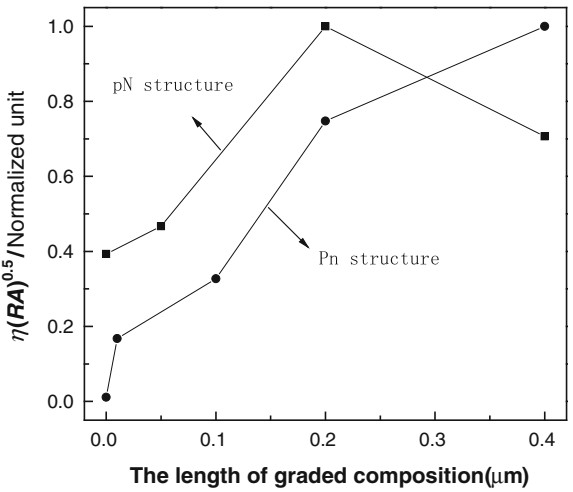

Fig. 2.20 Normalized $\eta \cdot \sqrt{RA}$ with the length of grade composition in two heterojunction structures

field can be handled by using a two-dimensional model, which overcomes the shortage of the one-dimensional model.

In this section, numerical simulation is used to study the relationship of R_0A and photocurrent with the thickness of p region, distance of contacts, doping concentration, minority lifetime and trap-assisted tunneling effect, and the influence of electron recombine lifetime and surface recombine rate on the spectral response. The spectral response is investigated experimentally and theoretically, which provides a basic reference for the optimization of device design.

The related material parameters of HgCdTe in this calculation are listed in Table 2.10, the composition of the p-type epitaxial layer is $x = 0.224$, the power density of infrared radiation is 10 W/m^2. In this calculation, the typical device parameters are listed as follows: the acceptor concentration of the p region is 10^{15} cm^{-3}, the thickness (junction depth) of the n^+ region is 1 μm, and the operating temperature is 80 K. The definite mesh of device is carefully created, which is shown in Fig. 2.21b.

Table 2.10 Related material parameters of $Hg_{1-x}Cd_xTe$ ($x = 0.224$) in calculation ($T = 80$ K)

Parameter	Value	Parameter	Value
Band gap E_g	0.122 eV	Electron mobility μ_e	5.0×10^4 cm^2/(V s)
Absorption coefficient α	2.15×10^3 cm^{-1}	Hole mobility μ_h	400 cm^2/(V s)
Effective electron mass m_e	9.15×10^{-3} m_0	Auger recombination rate G_{A1}	3.54×10^{-25} cm^6/s
Effective hole mass m_h	0.50 m_0	Radiative recombination rate G_R	2.00×10^{-10} cm^3/s
Refractive index n	3.54		

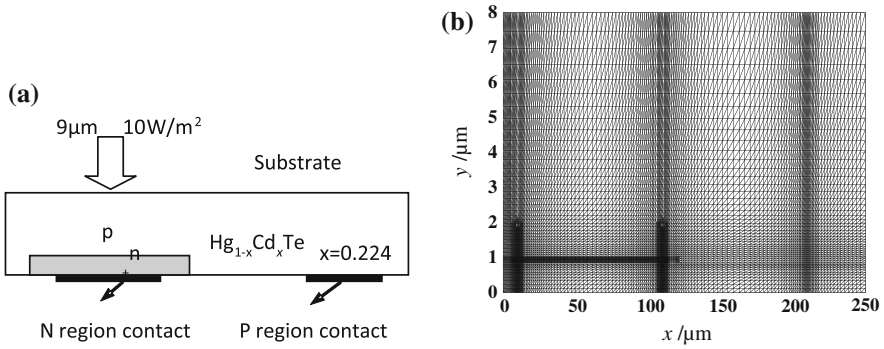

Fig. 2.21 **a** N-on-p structure of HgCdTe infrared detector, **b** The finite mesh of device

2.2.3.1 R_0A and Photocurrent

In the design of long wavelength devices, thickness of *p* region, distance of contacts, minority lifetime, doping concentration, and trap-assisted tunneling effect in a deep level have important influences on the R_0A, photocurrent, and quantum efficiency of device.

The relationship between the thickness of the *p* region and R_0A is shown in Fig. 2.22. Radiation recombination, Auger recombination, and band-to-band tunneling effects are included in the calculation. The thickness of the n^+ region is about 1 μm. The n^+ region is the heavy doping region, where the resistance is very small. In contrast, the *p* region is relatively thick and is the main absorption region under back illumination, and the resistance of it is relative large. The determination of thickness of the *p* region should consider both the light absorption and R_0A. When the thickness of the *p* region increases, the efficiency of absorption will also increase. However, the photogenerated carriers are more difficult to diffuse into the junction region, so the thickness cannot be too large. Additionally, the increase in

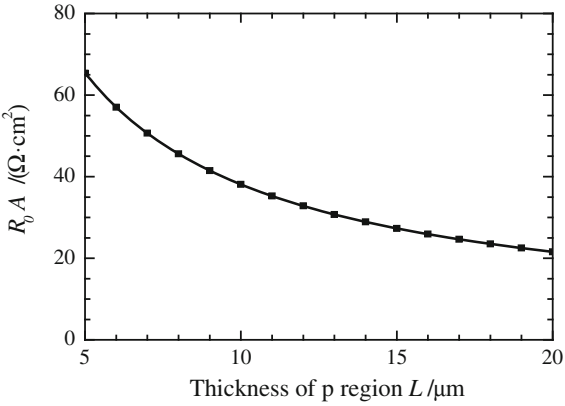

Fig. 2.22 Relationship between R_0A and the thickness of *p* region

the thickness of the p region will decrease the parallel resistance. Therefore, R_0A decreases with the thickness of p region. As known from the calculation, when the thickness of the p region varies from 7 to 20 μm, the photocurrent will change little. Therefore, the proper thickness of p region is about 10 μm. It should be noted that in the 1D model, R_0A will be nearly proportional to the thickness of the p region, which is very different than the 2D model and is not in accord with the real device. Actually, both vertical and lateral current exist in the device (see Fig. 2.1), and the distribution of current density is not uniform (Figure 2.23a, b shows the profile of current density in the device with thicknesses of 8 and 20 μm respectively). In the following calculation, the thickness of the p region is 10 μm.

The contact size of the n^+ region with heavy doping has no effect on the device performance. The resistance of p region is large. The calculated results show that the device performance with different width of contacts in p region is the same. However, the location of the contact has an important influence on both R_0A and photocurrent, as shown in Figs. 2.24 and 2.25.

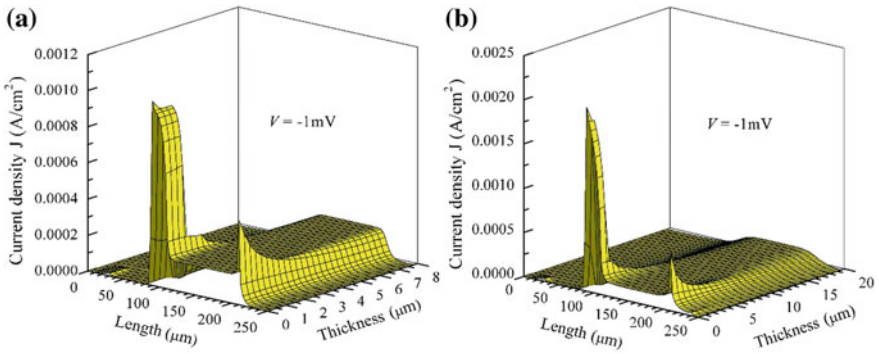

Fig. 2.23 Profile of current density with **a** the p region thickness of 8 μm and **b** the p region thickness of 20 μm

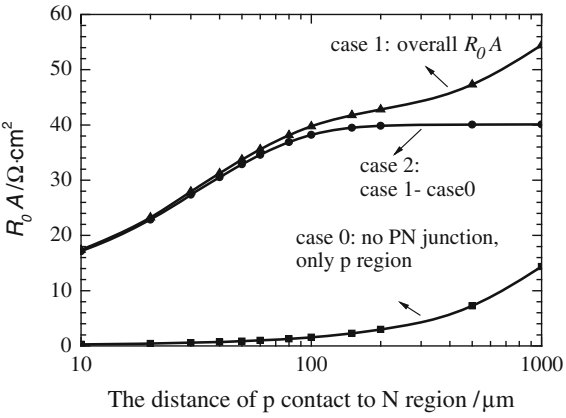

Fig. 2.24 Relationship between R_0A and the location of contact in p region

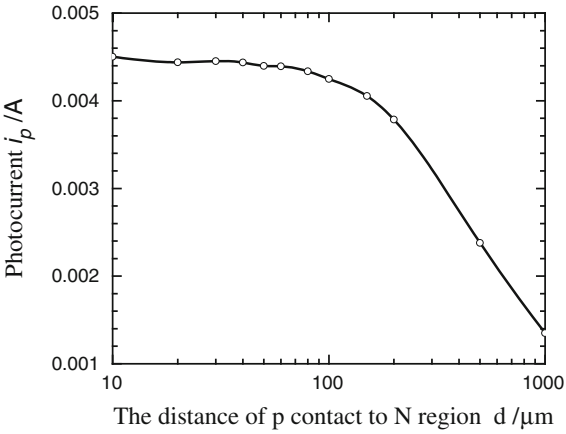

Fig. 2.25 Relationship between photocurrent (i_p) under zero bias and the location of contact in *p* region

Considering all the resistances, R_0A obviously increases with the distance of contacts (Marked as case 1). One reason is the influence of series resistance in the *p* region. If the whole device is set to a uniform p-type structure, series resistance is calculated by the same way (Marked as case 0). This shows that the resistance is approximately linear with the distance of contacts (Semi-log coordinate in Fig. 2.24). The difference between them (case2 = case1 − case0) can be treated as the R_0A of the *pn* junction without series resistance. When the distance of contacts is 100 μm, R_0A increases with the distance of contacts. And when the distance is more than 100 μm, R_0A tends to be stable. This is mainly due to the profile of the electric field and current density and is related to the location of contact in the *p* region. The current density with a contact distance of 10 μm (see Fig. 2.26) is different from that with a contact distance of 100 μm (see Fig. 2.23). The influence of the contact distance on the electric field (in the junction area) and current density is gradually weakened when the distance of contacts is great enough. Therefore, R_0A of *pn* junction tends to be stable.

The situation of photocurrent under zero bias is different from R_0A. The photocurrent under zero bias decreases with the distance of contacts. As shown in Fig. 2.25, when the distance of contacts is 100 μm, the photocurrent under zero bias changes little, and when the distance is more than 100 μm, the photocurrent under zero bias is decreased notably. Photocurrent reflects quantum efficiency. Therefore, the decrease in photocurrent illustrates the decrease of quantum efficiency. Apart from the influence of electric field and current density due to the change of the contact location, the main reason for the decrease of quantum efficiency is that the collecting efficiency of photogenerated carriers to the contact decreases with the distance of contacts. Assume that the gain is 1, quantum efficiency (η) can be extracted from the photocurrent. As shown in Fig. 2.27, the trend of quantum efficiency is similar to that of the photocurrent. The detectivity D^*, η, and R_0A of device have the following relationship [46]:

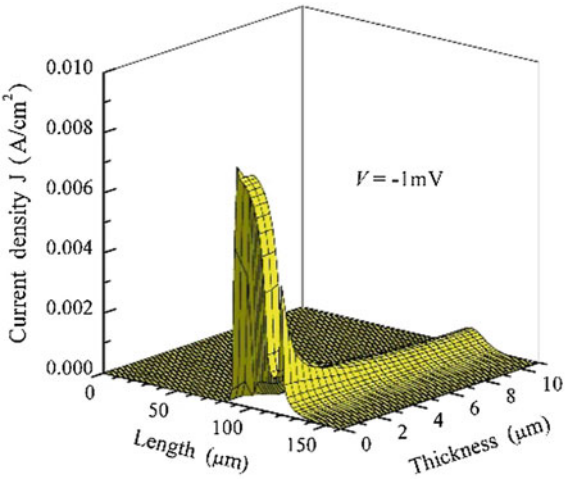

Fig. 2.26 Distribution of current density in device when the distance of contacts in p region is 10 μm

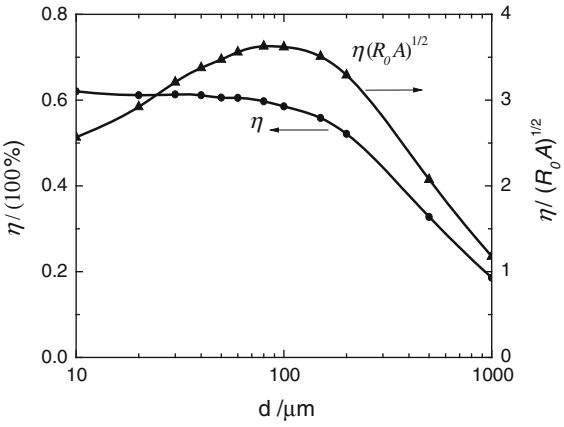

Fig. 2.27 Relationship between quantum efficiency (η, η $(R_0A)^{1/2}$) and the distance from p layer contact to n^+ area (d)

$$D^* \propto \eta(R_0A)^{1/2} \tag{2.44}$$

The relationship between $\eta(R_0A)^{1/2}$ and the location of contact is shown in Fig. 2.27. When the contact is about 100 μm from n^+-type region, $\eta(R_0A)^{1/2}$ will reaches the maximum size. It is the optimal location of contact in p region.

The structure of a linear HgCdTe device is shown in Fig. 2.28. Two lines of pn junction are staggered, the first line of pn junction is about 60 μm away from the common contact, and the second line is about 150 μm. Based on the above discussion, different distances of contacts will produce the different dynamic resistance and photocurrent, which leads to the difference of overall signal. A simple and feasible solution is to set a symmetrical common contact in the p region, which can eliminate the difference of signal caused by the geometrical structure of device. In

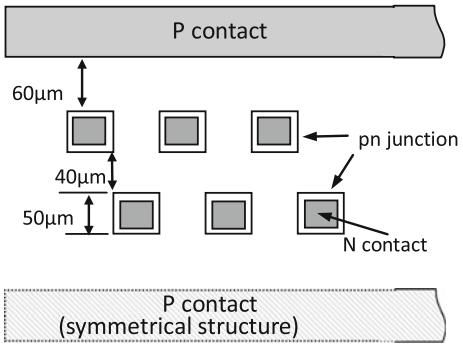

Fig. 2.28 Planar geometrical structure of linear HgCdTe detector

addition, if the distance of two contacts is too large, the photocurrent will not increase linearly and distinctly with the light power density. Therefore, the distance of contacts should not be too large.

In the above calculation, it is assumed that an ideal abrupt *pn* junction is formed at the interface between the n^+ region and the *p* region. In fact, there are different distributions of donor impurity, which are dependent on the process technology. HgCdTe-based *pN* junctions are usually formed by ion implantation. A p-type epitaxial layer is changed into an n type in the ion implantation region. The profile of donor impurity in the ion implantation region varies with the energy of ion implantation. Moreover, the ion implantation damage defects can influence the mobility and lifetime of HgCdTe material. In this section, the effect of ion implantation damage defects is not considered. Only the distribution of donor impurity in p-type region is discussed here.

For a *pN* junction formed by ion implantation, the distribution of donor impurity is approximated by Gaussian functions with appropriate parameters [47]. It is assumed that the distribution of donor impurity is described by Gaussian functions with variance δ, as shown in Fig. 2.29.

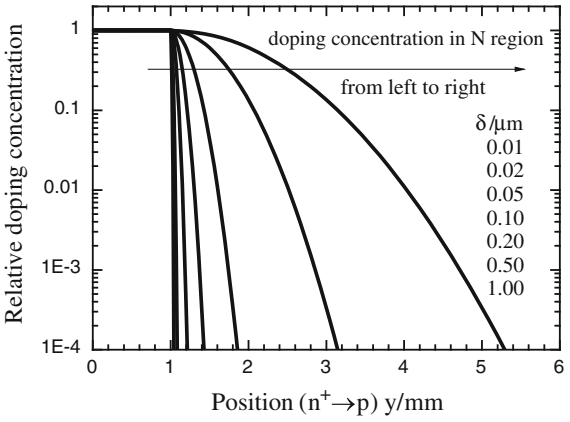

Fig. 2.29 Distribution of donor impurity in junction

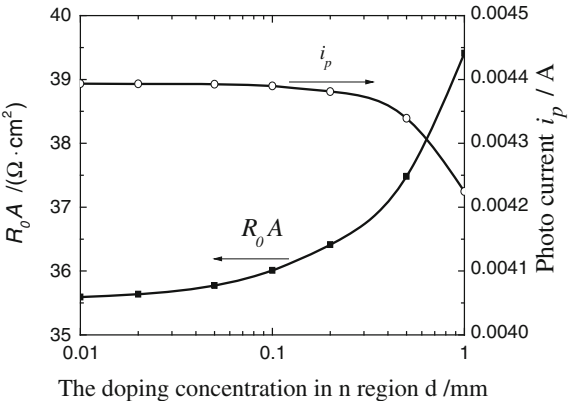

Fig. 2.30 Relationship of R_0A and photocurrent under zero bias with the different distribution of donor impurity in junction

The relationships of R_0A and photocurrent under zero bias with the distribution of donor impurity are shown in Fig. 2.30. R_0A increases slowly with the broadening of the donor impurity distribution. On the other hand, the photocurrent under zero bias decreased slightly with the broadening of the donor impurity distribution. Therefore, it is obvious that there is little influence of the distribution of donor impurity on R_0A and photocurrent. It illustrates that the conclusion drawn from the abrupt junction can be applied in the graded junction.

For an n-on-p structure, light absorption mainly occurs in the *p* region, thus the minority (electron) lifetime in the *p* region is very important for the device. In contrast, the majority (hole) lifetime has little effect on device. The electron lifetime of HgCdTe material is determined by three recombination processes: Radiative recombination, Auger recombination, and SRH recombination. The prior two recombination processes belong to the inherent properties of HgCdTe material regardless of the fabrication processes. However, SRH recombination is closely related to the fabrication processes. The defects, dislocations, and impurities of material are likely to form the recombination center, which results in increase of electron lifetime.

The relationship of R_0A and photocurrent (i_p) under zero bias with the electron lifetime of SRH recombination is shown in Fig. 2.31. It demonstrates that device performance decreases rapidly with the electron lifetime of SRH recombination. The electron lifetime is short, which reflects a large density of recombination centers formed by material defects, dislocations, impurities, etc. Therefore, R_0A and photocurrent are decreased. If the electron lifetime is long, photogenerated carriers will have enough time to diffuse into the junction region. In order to obtain the excellent device performance, the electron lifetime of SRH recombination should be longer than 100 ns. R_0A and photocurrent tend to be saturation when electron lifetime is about 1 μs. For high-quality HgCdTe material, the density of recombination centers is very small, and the electron lifetime of SRH recombination is long. The minority lifetime is an important parameter of device design.

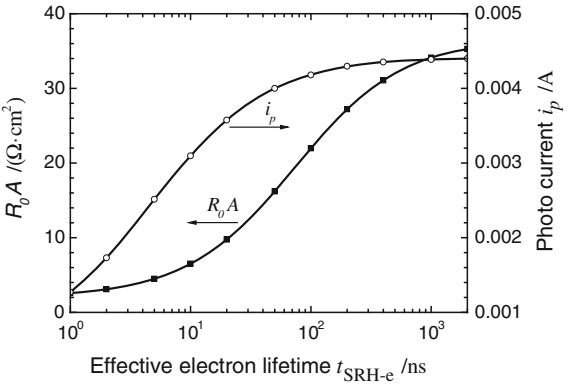

Fig. 2.31 R_0A and photocurrent (i_p) under zero bias with the electron lifetime of SRH recombination

The influence of the donor concentration in the n^+ region on device performance is seldom mentioned in literatures. In the above calculation, the donor concentration in the n^+ region is 10^{17} cm^{-3} (the effective doping concentration is about 1.6×10^{16} cm^{-3}) R_0A and photocurrent with different donor concentration in the n^+ region are discussed in detail. The acceptor concentration in p region is still 10^{15} cm^{-3} in the calculations. In general, the mobility of carriers and concentration of recombination center vary with the doping concentration. However, there is no reported qualitative explanation of this problem. Therefore, assume that other parameters like carrier mobility and concentration of recombination center do not vary with the doping concentration in calculation.

The calculated results are shown in Fig. 2.32, where the abscissa axis is the effective doping concentration. The effective mass of electrons in HgCdTe is very small. Therefore, the effective state density of conduction band is low (approximately 3.0×10^{15} cm^{-3} at 80 K). When the doping concentration is more than 1×10^{16} cm^{-3}, the conduction band will become degenerate, and impurity ionization rate decreases rapidly, which results in the failure of high doping. Figure 2.32 shows that both R_0A and photocurrent increase with the donor concentration in n^+ region. R_0A and photocurrent tend to be saturated when the donor concentration is 2×10^{16} cm^{-3}. The increase of donor concentration in n^+ region

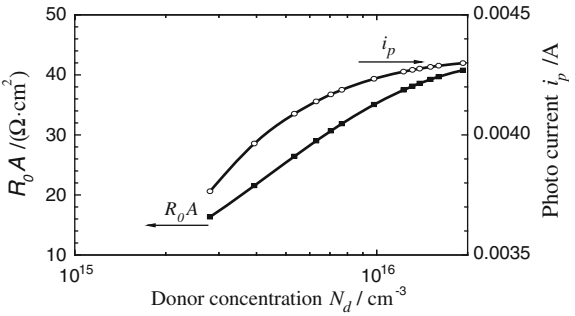

Fig. 2.32 The relationship of R_0A and photocurrent with effective donor concentration

can enhance the built-in electric field and widen the junction, which results in the increase of R_0A and photocurrent. The results show that the effective concentration of n^+ region should be more than 1×10^{16} cm^{-3}.

The effective hole mass of HgCdTe is relatively large, the effective state density of the conduction band is high, about 1.4×10^{18} cm^{-3} at 80 K. Therefore, apart from a very high doping concentration, the conduction is usually in non-degenerate state, and impurity ionization rate is very high. The acceptor concentration of the *p* region in infrared HgCdTe photovoltaic the *n* region, mobility and the concentration of recombination centers will vary with the acceptor concentration. Here the device performance is discussed in a simple condition. Assume that other parameters like carrier mobility and concentration of recombination center do not vary with the acceptor concentration in calculation.

The abscissa axis in Fig. 2.33 is the effective acceptor concentration. It shows that R_0A and photocurrent will increase with the acceptor concentration. R_0A and photocurrent tend to be saturated when the acceptor concentration is about 10^{16} cm^{-3}. The acceptor concentration in p-type material is about 10^{15}–10^{16} cm^{-3}, this acceptor concentration can make photocurrent and R_0A reach a maximum value. The *I*–*V* curve illustrates that the band-to-band tunneling rate also increases with the acceptor concentration in *p* region, and results in the increase of differential resistance (R_d) at low reverse bias. The results show that the effective acceptor concentration of *p* region is at the range of 10^{15}–10^{16} cm^{-3}.

When radiative recombination, Auger recombination, SRH recombination, and band-to-band tunneling (BBT) effect are considered in the calculation, the dark current is still smaller than in the real HgCdTe detector. Therefore, there must be other physical effects, which contribute to the dark current of the device. Many researchers have proposed different models to explain dark current. Nemirovsky et al. [48, 49] proposed a trap-assisted tunneling model (TAT), Elliot et al. [50] proposed an impact ionization model, Dosenfeld et al. [51] proposed a TAT described by segmented function. There are several free parameters that can be used to adjust these models. Therefore, the measured dark current can be explained to some extent. At present, there still is not an acknowledged model that can explain the total dark current in the experiment. Therefore, Hurkx et al. proposed a revised

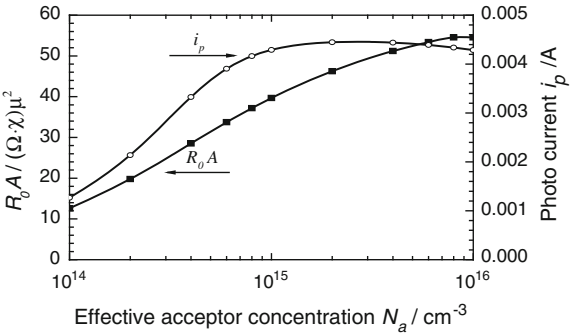

Fig. 2.33 Relationship of R_0A and photocurrent with effective acceptor concentration of *p* region

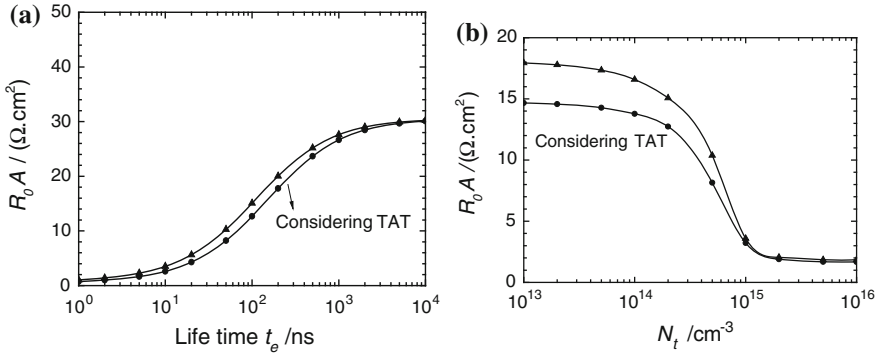

Fig. 2.34 R_0A with and without trap-assisted tunneling effect

model [52], which combines the TAT effect with the SRH recombination effect. The recombination rate can be expressed as

$$R_{\mathrm{TAT+SRH}} = \frac{pn - n_{\mathrm{ie}}}{\frac{\tau_{\mathrm{p}}}{1+\Gamma_{\mathrm{p}}}\left[n + n_{\mathrm{ie}}\exp(\frac{E_{\mathrm{T}}-E_{\mathrm{i}}}{kT})\right] + \frac{\tau_{\mathrm{n}}}{1+\Gamma_{\mathrm{n}}}\left[p + n_{\mathrm{ie}}\exp(\frac{E_{\mathrm{T}}-E_{\mathrm{i}}}{kT})\right]} \tag{2.45}$$

where E_{T} is the deep level of the trap, E_{i} and n_{ie} are the Fermi levels of intrinsic material and carrier concentration respectively, τ_{p} and τ_{n} are the recombination lifetime of holes and electrons respectively. Parameters Γ_{p} and Γ_{n} reflect the trap-assisted effect. For a weak electric field, this model can be simplified as SRH recombination. Lui et al. proposed a new model based on this current model, and the expression is similar to Eq. (2.45).

R_0A calculated by the Hurkx model varies with recombination lifetime and trap density is shown in Fig. 2.34. In the calculation, the effective doping concentration in the n^+ region is 10^{16} cm^{-3}. It shows that R_0A will decrease when the TAT effect is added into the calculation, especially when the electron recombination lifetime is very short. When the electron recombination lifetime is more than 100 ns, the TAT effect is not significant. When the trap concentration is more than 10^{14} cm^{-3}, R_0A will decrease rapidly. Figure 2.35 shows the relationship of quantum efficiency with trap concentration. It shows that when the concentration is more than 10^{15} cm^{-3}, quantum efficiency will decrease rapidly. Considering both R_0A and quantum efficiency, the trap concentration should be less than 10^{14} cm^{-3}.

2.2.3.2 Spectral Response

Figure 2.36 shows the spectral response (quantum efficiency) under different values of electron SRH lifetime. When the electron lifetime varies from 10 ns to 100 ns, quantum efficiency is increased by 50 %, and when the electron lifetime varies from 100 ns to 10 μs, the increase of quantum efficiency is limited, which is the same

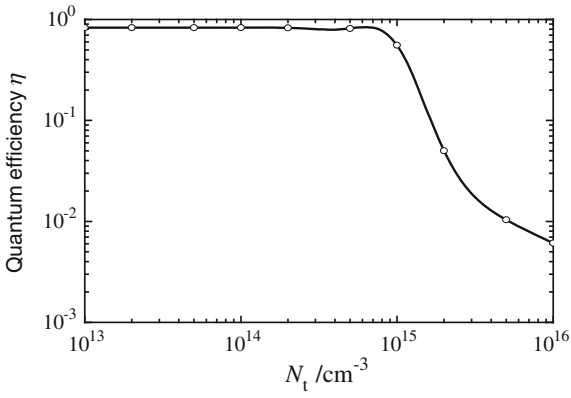

Fig. 2.35 Relationship with quantum efficiency and deep level concentration (λ = 9.5 mm)

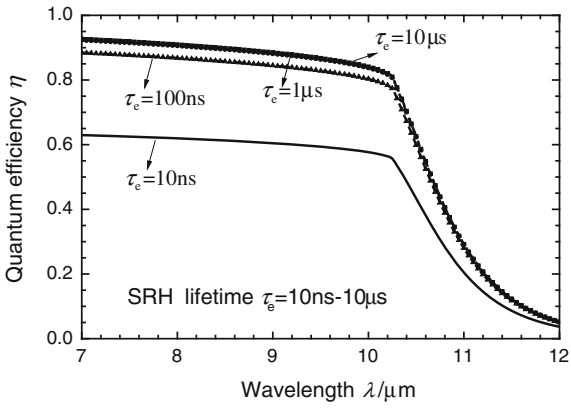

Fig. 2.36 Relationship of quantum efficiency and electron recombination lifetime

trend as Fig. 2.31. The device has relatively high quantum efficiency when the recombination lifetime of electron is more than 100 ns. The cutoff wavelength of the device is about 10.8 μm. Figure 2.37 shows the energy profile along the thickness direction (the direction of incident light). It shows that the shorter the wavelength, the radiation absorption is closer to the surface. Besides, the photon whose energy is only below the band gap tends to be uniform absorbed.

The material discontinuity at surface or interface of semiconductor devices, leads to a certain density of interface state, which results in the increase of the carrier recombination rate. If surface tarnish, oxidation and adsorption exist, surface recombination centers are possibly induced. In order to reduce the interface state, the surface of a HgCdTe device is generally passivated, including anodizing or prepared passivation film, such as ZnS and CdTe film. After the surface passivation, the density of the interface state is greatly reduced. However, the surface recombination effect still exists, which influences the dark current and photocurrent. Research into the influence of surface recombination on device performance has practical significance.

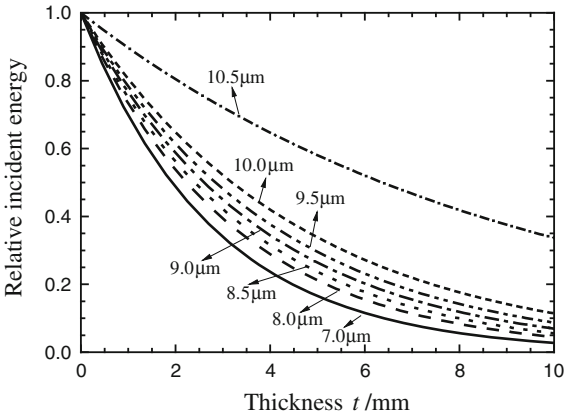

Fig. 2.37 Distribution of incident radiation energy in the device along the direction of thickness

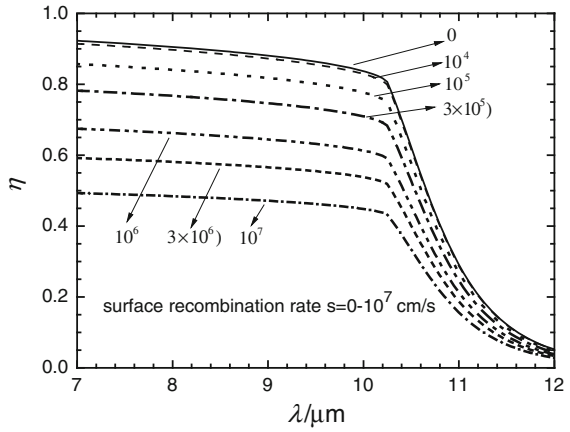

Fig. 2.38 Relationship of quantum efficiency and surface recombination rate

The relationship between quantum efficiency with surface recombination rate is shown in Fig. 2.38. The surface recombination rate is very low, and has little effect on the quantum efficiency. When the surface recombination rate increases to 10^5 cm/s, quantum efficiency begins to decrease. When it is more than 10^5 cm/s, quantum efficiency decreases rapidly. In order to obtain high quantum efficiency, the surface recombination rate for a long wavelength n^+-on-p device should be controlled below 10^5 cm/s, and preferably less than 10^4 cm/s.

Rosenfeld et al. have studied the responsivity of long wavelength devices with an n-type absorber layer. The results show that the responsivity decreases rapidly when the surface recombination is about 2×10^3 cm/s (about two orders of magnitude different from the above conclusion 10^5 cm/s). The reason can be explained as follows:

The influence of surface recombination on responsivity is related to the factor γ

$$\gamma = \frac{sL}{D} = s\sqrt{\frac{\tau}{D}} = \sqrt{\frac{q}{kT}}s\sqrt{\frac{\tau}{\mu}} \tag{2.46}$$

where μ and τ are the (bulk) minority mobility and lifetime respectively. The absorption region mainly contributes to the responsivity. The factor γ represents capacity of surface recombination. For the device with a p-type absorber layer, electrons acting as the minority carrier have a short lifetime and large mobility. Therefore, γ is small under the same surface recombination rate, and has little impact on the responsivity. For the device with an n-type absorber layer, holes acting as minority carrier have a long lifetime and small mobility. Therefore, γ is large under the same recombination rate at surface, and has large impact on the responsivity. Therefore, the device with the n-type absorber layer is a better choice under the same surface recombination rate.

Figure 2.39 shows the experiment measurements (solid line) and theoretical calculation (dot line) of spectral response of two n^+-on-p detectors. The results are in agreement with the experimental measurements near the cutoff wave band and the short wave band. When the wavelength is shorter than the 1–2 μm wave band (corresponding to the material band gap), the experimental data are lower than that of theoretical calculation. This phenomenon happens in many long wavelength devices. One possible reason is the nonuniform composition of material in the device.

There are lateral and vertical profiles of components in HgCdTe material. For a large material region, the lateral nonuniformity of composition may be obvious. A detector grown by MBE with an active detection area of only 50 × 50 μm^2 is shown in Fig. 2.39. Therefore, the lateral nonuniformity of composition can be neglected. The vertical nonuniformity of the composition is the main factor for the spectral response.

The device is a GaAs/CdTe/HgCdTe multilayer structure. The diffusion of composition is inevitable in the process of material growth and fabrication, which

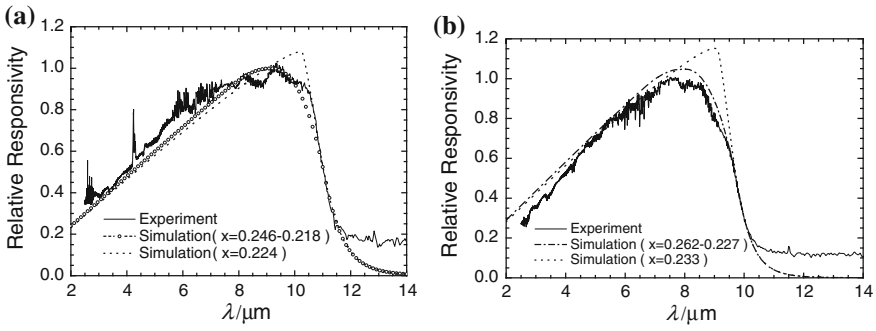

Fig. 2.39 Spectral response of long wavelength. **a** Detector 1, **b** detector 2

results in the vertical nonuniformity of HgCdTe material. Based on the theory of graded components, the numerical simulations of detectors 1 and 2 are shown in Fig. 2.39. From the interface to the surface of device, the components of detector 1 vary from 0.246 to 0.218, and the composition of detector 2 varies from 0.262 to 0.227. It shows that the results of the graded composition theory are more accurate compared to those of the uniform composition theory.

2.2.3.3 Thickness of Absorption Layer and Interface Charge Density

As HgCdTe materials and device technology matures, HgCdTe detector structure tends to become more complicated, such as heterojunctions, two-color detectors [53–59], etc. The minority diffusion length in the base region of long wavelength HgCdTe detectors is relatively small, but the absorption layer must be large, so it is necessary to optimize the thickness of the base region and, due to bandgap narrowing, the influence of the interface charge is more obvious so it is very necessary to analyze the impact of interface charge.

For a typical n-on-p HgCdTe detector, when the incident light is back illuminated from substrate into the detector, the light is absorbed in base region. The photogenerated carriers then diffuse to junctions, and are separated by the built-in electric field in the junction to form a photoelectromotive force. Therefore, under the same conditions, the thicker the base absorption layer, the more the light is completely absorbed thus creating more photogenerated carriers, and higher responsivity. On the other hand, the absorption of light is not uniform, but varies along the length of the exponential decay path, i.e., absorption of light mainly occurs at the beginning of the absorption path. The thicker absorption layer, resulting in the main absorption region is further from the junction. Therefore, the probability of the photogenerated carriers participating in the diffusion process is greater, resulting in a lower generated responsivity. It is acknowledged that the responsivity of the device, as a function of the light absorption layer thickness, changes according to the two competing mechanisms. When the absorption layer is thinner, the former mechanism dominates, therefore an increase in responsivity is due to an increase in the absorption layer thickness. When the thickness absorption of layer is large, the latter mechanism is dominant and therefore the responsivity decreases with an increase in absorption layer thickness. So there is an optimal absorption layer thickness in the middle.

The following is an example of a long wavelength detector in which the optimal thickness of the absorption layer is obtained by simulation. Detailed material and structural parameters are listed in Table 2.11. *P* region is the base region, so the thickness of the *p* region is the absorption layer. According to the material parameters, the minority diffusion length can be solved:

Table 2.11 Material and structural parameters of long wavelength HgCdTe photodetector

Parameters	Value	Units
Cd composition (x)	0.211	–
Temperature	77	K
Electron SRH lifetime	5	ns
Hole SRH lifetime	5	ns
Doping density of N region	1×10^{17}	cm^{-3}
Doping density of P region	8×10^{15}	cm^{-3}
Thickness of N region	1	mm
Thickness of P region	d	mm
Width of N region	30	mm
Distance of unit center	40	mm

Reprinted from Ref. [22], with kind permission from Springer Science+Business Media

$$L_d = \sqrt{D_n \cdot \tau} = \sqrt{\frac{kT}{q}\mu_n \cdot \tau} = 21\ \mu m \tag{2.47}$$

The longer the diffusion length, the easier minority carriers diffuse to a junction. So diffusion length is a very important parameter that directly influences the responsivity.

Figure 2.40 shows the responsivity as function of the wavelength of incident light. The peak responsivity occurs when the wavelength of incident light is 12.4 μm and the thickness of absorption layer changes from 5 to 21 μm. Figure 2.40a shows, at the short wavelength range, the responsivity monotonously decreases with the increase in the thickness of the absorption layer. The absorption coefficient at the short wavelength range is larger than that of the long wavelength range, thus the light is completely absorbed over a small fraction of the absorption

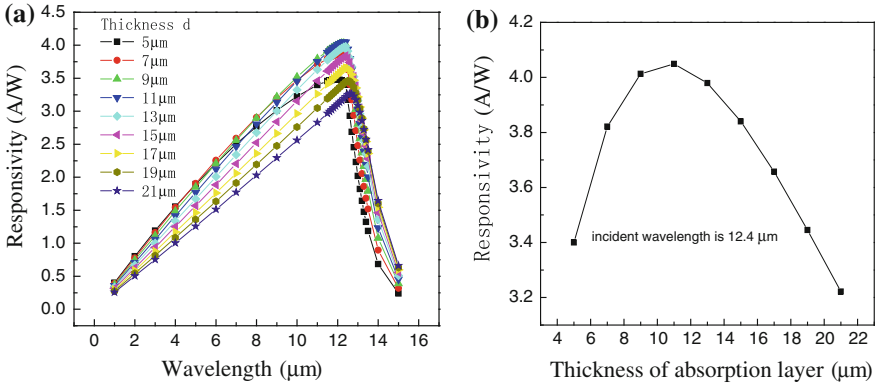

Fig. 2.40 **a** Photo response as function of the wavelength of incident light with the thickness of absorption layer changing from 5 to 21 μm, **b** when the wavelength of incident light is 12.4 μm, photo response as function of the thickness of absorption layer. Reprinted from Ref. [22], with kind permission from Springer Science+Business Media

layer. Here, diffusion is the dominant mechanism of the responsivity causing the monotonous decrease. It is also shown in Fig. 2.40a that the responsivity monotonously increases with the increase of the thickness of the absorption layer, and finally saturates, when the incident light wavelength is longer than the cut-off wavelength. This is because the absorption coefficient in the long wavelength range is very small, so the absorption length is equal to the thickness of the absorption layer. Here, absorption is the dominant mechanism of the responsivity causing the monotonous increase. When the thickness of absorption layer is close to the diffusion length of the minority carrier, the absorption at one diffusion length distance from the *p-n* junction can not affect the responsivity, consequently causing the gradual saturation. It can be seen in Fig. 2.40b that, near the peak responsivity wavelength, the responsivity increases with the increase of the thickness of absorption layer first, and then decreases. The maximum responsivity, which is the consequence of competing effects of the absorption and diffusion, is reached when thickness of absorption layer is 11 μm.

Figure 2.41 compares the photoresponse for different minority carrier lifetimes when the incident light wavelength is 12.4 μm as a function of minority carrier lifetime for 5, 10, 20, and 50 ns. The corresponding minority diffusion length for each minority carrier lifetime is 21, 29.7, 42, and 66.4 μm, respectively. The absorption length, which is determined by the absorption coefficient, is 5.46 μm. As shown in Fig. 2.41, responsivity increases with an increase of the minority carrier lifetimes. Therefore, the optimal d_{abs} increase with increasing of the diffusion lengths.

Figure 2.42 compares the responsivity for the different wavelengths of incident light when the minority carrier lifetime is 5 ns. The corresponding absorption lengths are 0.77, 1.97, 3.33, and 5.46 μm, respectively, and the minority diffusion length is 21 μm. It is found that the responsivity increases with the increase in the wavelength of the incident light. And the optimal thickness of the absorption layer

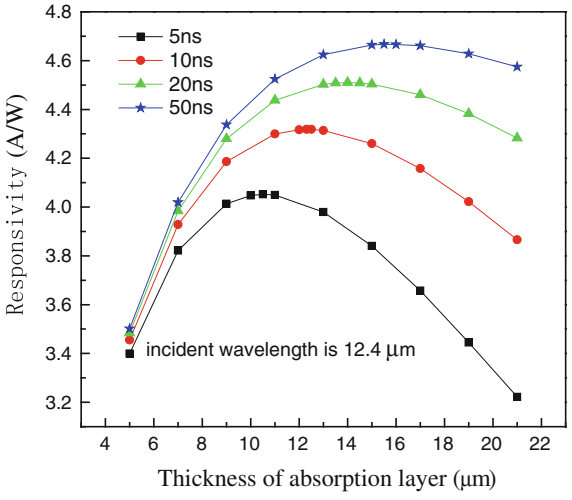

Fig. 2.41 When incident light wavelength is 12.4 μm, responsivity versus the thickness of absorption layer under different minority carrier lifetime. Reprinted from Ref. [22], with kind permission from Springer Science+Business Media

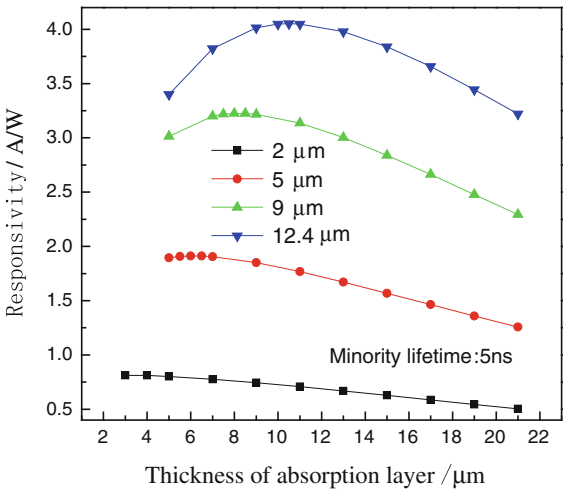

Fig. 2.42 Responsivity versus the thickness of absorption layer under different incident light wavelengths with the minority lifetime of 5 ns. Reprinted from Ref. [22], with kind permission from Springer Science+Business Media

increases as well. The reason for the absorption layer increase is that the absorption coefficient decreases with increasing wavelength of incident light with constant Cd mole fraction of HgCdTe material. Specifically, the absorption length increases with increasing wavelength of the incident light. Therefore, the optimal thickness of the absorption layer increases with increasing absorption length. When the wavelength of incident light remains constant, the intrinsic absorption coefficient of HgCdTe material decreases with increasing of the mole fraction. Consequently, the optimal thickness of the absorption layer of mid and short wavelength devices is smaller than that for long wavelength devices.

By discussion, the optimal absorption layer thickness when the minority carrier lifetime is 5, 10, 20 and 50 ns, and incident light wavelength is 2, 5, 9, and 12.4 μm, a fitted empirical formula for predicting the optimal absorption layer thickness as function of diffusion length and absorption length can be obtained:

$$d = 1.72 \times \sqrt{L_a} \cdot \ln L_d - 1.31 \tag{2.48}$$

In Eq. (2.48), d is the optimal absorption layer, L_a is absorption length, L_d is diffusion length, and the unit are all μm, as shown in Fig. 2.43.

Due to the lattice discontinuity and complex fabrication process, many traps will be formed in the substrate and the passivation layer of HgCdTe device causing a significant impact to device performance. Traps can be usually divided into two categories: donor trap and acceptor trap. A full state of the trap is defined as the state that is occupied by electrons, and an empty state of the trap is the state that is occupied by holes. For a donor trap, it is neutral in full state, which can capture holes or release electrons. Additionally, a donor trap is positively charged in the empty state, and can capture electrons or release holes. Therefore, the interface of donor traps is usually positively charged. An acceptor trap is negatively charged in the full state and can capture holes or release electrons. Additionally, it is neutral in

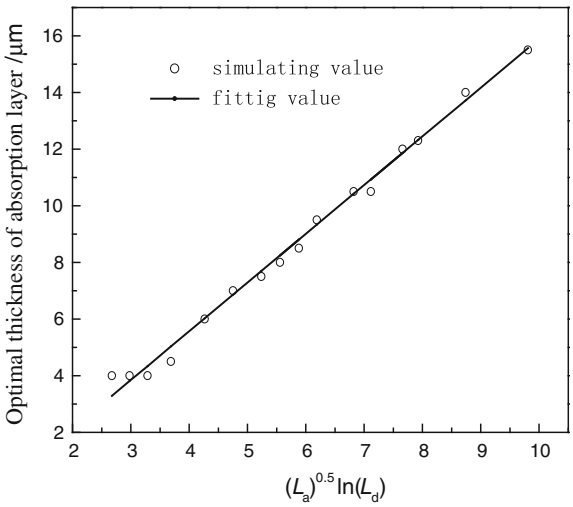

Fig. 2.43 Fitting curve of the optimal thickness of absorption layer as a function of absorption length L_a and diffusion length L_d. Reprinted from Ref. [22], with kind permission from Springer Science+Business Media

the empty state and can capture electrons or release holes. Therefore, the interface of acceptor traps is usually negatively charged. In addition, the fixed charge and moveable charge usually exist in the passivation layer. Here, they are all equivalent as interface charges in calculations.

The structural and material parameters are the same with that of the device listed in Table 2.11, and the thickness of the p region is 11 μm. The spectral response of the device without interface charge and with interface charge is shown in Fig. 2.44. The interface charge in Fig. 2.44a is 1×10^{12} cm^{-2}, and in Fig. 2.44b is -1×10^{12} cm^{-2}.

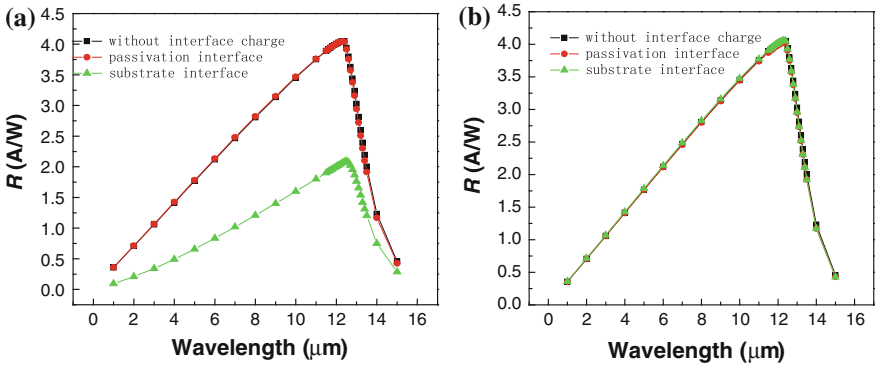

Fig. 2.44 Spectral response of the device without interface charge and with interface charge. **a** The density of interface charge is 1×10^{12} cm^{-2}, **b** the density of interface charge is -1×10^{12} cm^{-2}

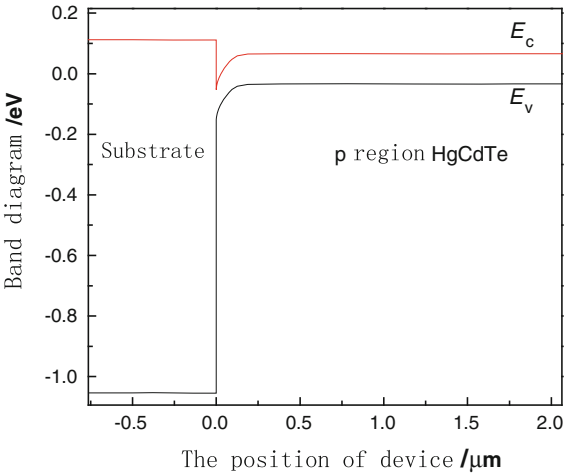

Fig. 2.45 The band diagram of device when the substrate interface charge is 1×10^{12} cm^{-2}

As shown in Fig. 2.44, regardless if the charge is positive or negative, the interface charge in the passivation layer has little effect on the device responsivity. However, the positive charge at the substrate interface has a great effect on the responsivity of device. The reason is that the energy band is changed by the charge at the substrate interface. As illustrated in Fig. 2.45, the energy band is bent down due to the positive interface charge, which results in the formation of an induced *pn* junction at the interface. When the device is back illuminated, photogenerated carriers are formed at the interface and some will be separated by the induced junction, which ultimately reduces the responsivity of the device. When the interface charge is negative, the energy band is bent upward, which results in the formation of an accumulation layer at the substrate interface. This accumulation layer has little effect on the responsivity of the device.

The analysis of the passivation layer is similar to the above situations. When the interface charge is positive, the direction of the built-in electric field generated by the induced junction is the same as that of the device. However, it is far away from the light absorption region, so it has little effect on the device responsivity. If a strong inversion occurs in the passivation layer, an n-type channel will be formed, which results in an increase of dark current and a decrease in device performance. When the interface charge is negative, a p-type accumulation layer at the interface will be formed, which can also lead to the increase of tunnel leakage currents at the surface.

The responsivity as a function of the positive substrate interface charge is shown in Fig. 2.46, where the wavelength of incident light is 12.4 μm. It shows that when the positive interface charge is more than 2×10^{10} cm^{-2}, the device responsivity will begin to decrease; when the positive interface charge is more than 5×10^{11} cm^{-2}, photo response will reach the minimum value. This phenomenon can be explained by the theory of MOS devices. The energy band is bent downward due to the positive interface charge, which results in the depletion of the p-type region at

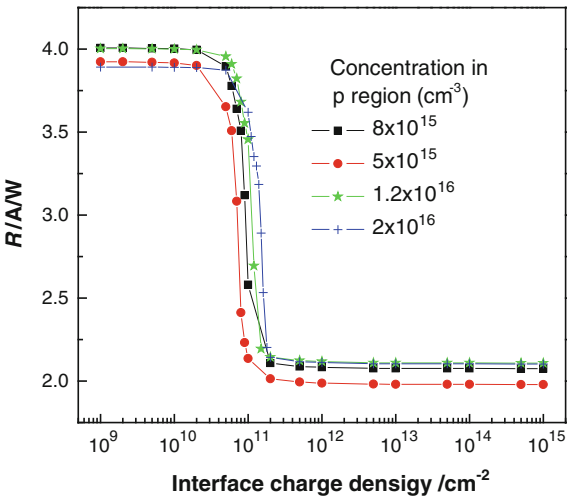

Fig. 2.46 Responsivity of device with the substrate interface charge, where the doping density in *p* region is 8 $\times$ 10^{15} cm, the wavelength of incident light is 12.4 μm

interface. When the density of the interface charge is 2 $\times$ 10^{10} cm^{-2}, an inverted *n* region will be formed at the interface, which results in the formation of an induced junction. The depletion width of the induced *pn* junction increases with the charge density. Photo-generated carriers generated in this area will be separated by the induced junction, which drastically reduces the device responsivity. When the density of the interface charge is 5 $\times$ 10^{11} cm^{-2}, a strong inversion layer will be formed at the substrate interface. The depletion width of the induced *pn* junction will stop increasing. Therefore, the responsivity of the device remains stable with the density of the interface charge.

Based on the theory of MOS devices [15], the interface charge density of a device with nominal inversion and strong inversion is expressed as follow:

$$N_s = N_a \cdot W = \sqrt{\frac{2\varepsilon_s \varepsilon_0 N_a V_s}{q}} \tag{2.49}$$

where W is the width of depletion region, V_s is the interface potential, ε_s is the relative permittivity of HgCdTe. When the composition of HgCdTe is 0.211, the relative permittivity of HgCdTe is 17.5. The surface potential of a device with the nominal inversion and strong inversion are expressed as follows:

$$V_{s-\text{inversion}} = \frac{kT}{q} \cdot \ln\left(\frac{N_a}{n_i}\right) \tag{2.50}$$

$$V_{s-\text{strong inversion}} = 2 \cdot \frac{kT}{q} \cdot \ln\left(\frac{N_a}{n_i}\right) \tag{2.51}$$

The concentration of p region is 8×10^{15} cm^{-3}. Integrating Eqs. (2.50) and (2.51) with Eq. (2.49), shows the calculated charge density of device with the inversion and strong inversion to be 8.05×10^{10} cm^{-2} and 1.14×10^{11} cm^{-2} respectively. The magnitude of the calculated results is the same as that in simulation. The difference between them is due to the depletion layer approximation in MOS theory.

Equation (2.49) shows that the critical density of the interface charge is related to the concentration the p region. The greater the concentration, the greater the critical density of interface charge. Therefore, the influence of the interface charge on the responsivity of device can be reduced by increasing the concentration of the p region. Figure 2.46 also shows the responsivity of the device varies with the interface charge, when the concentration of p region is 5×10^{15} cm^{-3}, 1.2×10^{16} cm^{-3} and 2×10^{16} cm^{-3}. The simulated results are very consistent with that of formula (2.49). In Fig. 2.46, the responsivity of a device with a concentration of p region 5×10^{15} cm^{-3} is less than that of a device when the concentration of p region is 8×10^{15} cm^{-3}. This is mainly because series resistance decreases with an increase of the p region concentration. When interface charge density is relatively small, the responsivity of a device with the p region concentration of 5×10^{16} cm^{-3} is smaller than that of device with the of p region concentration of 8×10^{15} cm^{-3}. This is mainly because an increase of p region concentration will reduce the minority lifetime. When the strong inversion of device occurs, the responsivity of a device with high of p region concentration will be slightly decreased. Instead, there is a relatively high responsivity in a device with a high density of interface charge. It is noted that an increase of the p region concentration can reduce the influence of the substrate interface charge on the responsivity of device, however, as concentration increases, the built-in electric field will also increase which results in an increase in tunneling current. At the same time, the decrease of carrier lifetime will lead to an increase of diffusion current, which also degrades the device performance.

2.2.4 *Design of Two-Color HgCdTe Detector*

With the development of infrared imaging technology, single wave band (monochromatic) imaging systems are increasingly being perfected. There is now an urgent demand for multiband (or multicolor, including two-color) imaging systems. Multicolor systems are designed to provide multiband data to reduce the complex background of a target. In terms of target recognition, signal identification and antijamming performance, a multicolor system is superior to monochromatic detectors. Research into multicolor systems has important application to many applications, such as earth observation, environment sensing, target discrimination and identification [60]. At present, many agencies in the world have carried out research work into multicolor infrared detectors [61–67]. HgCdTe two-color detectors have two working patterns: “sequential” pattern and “uniform” pattern

[68]. For a "sequential" pattern [69, 70], each unit has only one output electrode, the diode detecting band is determined by selecting an offset voltage, each band works in time-sharing and the device structure is relatively simple. Although two bands cannot be synchronously detected in space and time by varying the bias voltage to select the working band, it is useful for removing false signals and improving detection efficiency. For the "uniform" pattern [71, 72], each unit has two output electrodes, the two bands operate at the same time, but the device structure is more complicated than that of the device with "sequential" pattern. However, the two working bands are fully synchronous in space and time, which greatly expands functionality over monochromatic devices. Compared to monochrome devices, two-color devices are more difficult in the aspect of structure, process, and performance control [73–77]. Simulation calculations have become an effective means to predict the performance of two-color devices and reduce the device cost. Simulation can provide an important reference value for research into device manufacturing techniques.

2.2.4.1 Typical Two-Color HgCdTe Detectors

At present, there are mainly four types of typical two-color HgCdTe detector structures [61–77]: ① The n-p^+-n structure originally reported by the Hughes Research Laboratory (HRL); ② The p-n-n-n-p structure reported by the Lockheed Martin company (now called BAE Systems); ③ The n-p-p-p-n structure reported by the French LETI/LIR; ④ The p^+-on-n structure reported by the French LETI/LIR. This section will compare the photoelectric properties of four MW1/MW2 two-color detectors, and investigate the optimal structures that meet the demand of applications and the existing technology platform.

① HRL Structure. As shown in Fig. 2.47, this structure overcomes the shortcomings of the two-color detector with "sequential" pattern does not permit two photodiodes to operate at the same optimum bias thus causing an increase in spectral cross talk. However, each unit consists of two electrodes, and readout circuit to separate and read out two band signals at the same time. The theoretical spectral curve of this structure is shown in Fig. 2.48, and its structural parameters are listed in Table 2.12.

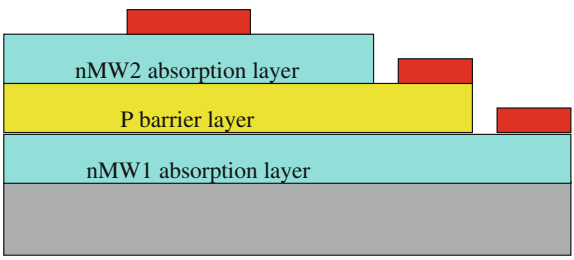

Fig. 2.47 The n-p^+-n schematic structure of two-color detector reported by HRL

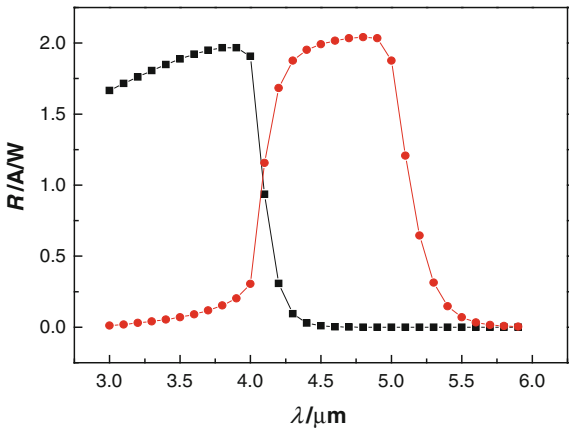

Fig. 2.48 The theoretical spectral curve of n-P^+-N two-color detector reported by HRL

Table 2.12 The structural parameters of n-p^+-n two-color detector reported by HRL

	Component	Doping (cm^{-3})	Thickness (μm)	Bandgap wavelength (μm)	SRH lifetime
nMW1 absorption layer	0.342	n-type 1×10^{15}	6	4.0	1 μs
p-barrier	0.4	p-type 1×10^{17}	2	3	
nMW2 absorption layer	0.304	n-type 1×10^{15}	7	5.0	

② BAE Structure. As shown in Fig. 2.49, an n-n-n barrier is introduced to this kind of structure between two photoelectric diodes, which can stop the diffusion of minority carrier hole between two wave bands, thus reducing the spectral cross talk. The theoretical spectral curve of this structure is shown in Fig. 2.50, and its structural parameters are listed in Table 2.13.

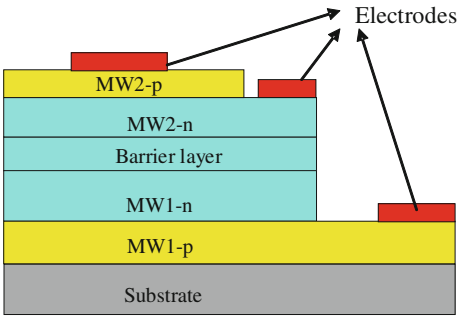

Fig. 2.49 The p-n-n-n-p schematic structure of two-color detector reported by BAE

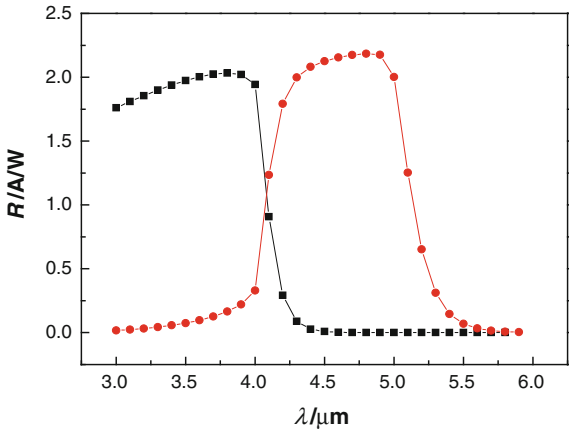

Fig. 2.50 The theoretical spectral curve of p-n-N-N-P two-color detector reported by BAE

Table 2.13 The structural parameters of p-n-n-n-p two-color detector reported by BAE

	Component	Doping (cm^{-3})	Thickness (μm)	Bandgap wavelength (μm)	SRH lifetime
MW1-p	0.42	p-type 2×10^{17}	1.2	2.86	1 μs
MW1-n	0.342	n-type 1×10^{15}	6	4.0	
Barrier	0.4	n-type 5×10^{15}	0.2	3	
MW2-n	0.304	n-type 1×10^{15}	6.0	5.0	
MW2-p	0.4	p-type 2×10^{17}	1.0	3.0	

③ LTEI Structure. As shown in Fig. 2.51, the structure of MW2 photoelectric diode is designed as an injected planar junction, and the MW1 diode is in situ a mesa junction. There is a high duty cycle in the LTEI structure. The theoretical spectral curve of LTEI structure is shown in Fig. 2.52, and its structural parameters are listed in Table 2.14.

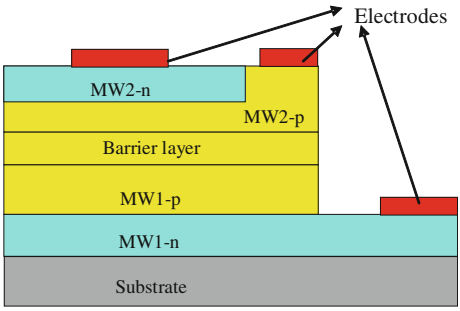

Fig. 2.51 The n-p-p-p-n schematic structure of two-color detector reported by LETI

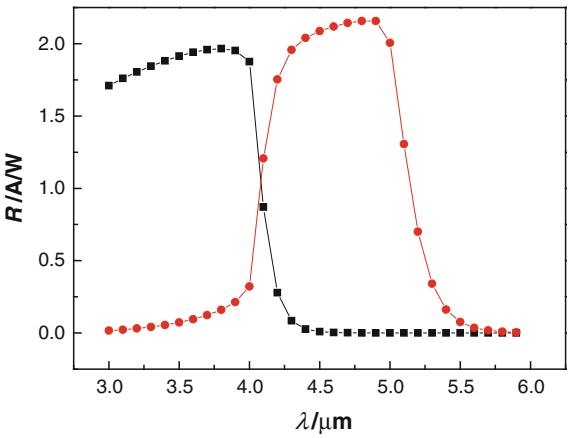

Fig. 2.52 The theoretical spectral curve of n-p-p-p-n two-color detector reported by LETI

Table 2.14 The structural parameters of n-p-p-p-n two-color detector reported by LETI

	Component	Doping (cm^{-3})	Thickness (μm)	Bandgap wavelength (μm)	SRH lifetime
MW1-n	0.42	n-type 2×10^{17}	1.2	2.86	10 μs
MW1-p	0.342	p-type 1×10^{15}	6	4.0	
Barrier	0.4	p-type 5×10^{15}	0.2	3	
MW2-p	0.304	p-type 1×10^{15}	7	5.0	
MW2-n	0.304	n-type 2×10^{17}	1.2	5.0	

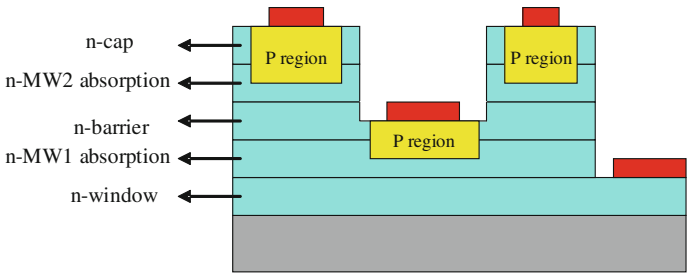

Fig. 2.53 The schematic structure of two-color detector based on p^+-on-n reported by Rockwell

④ Rockwell Structure. As shown in Fig. 2.53, this structure is actually made up of two vertical integration p^+-on-n planar diodes, which is formed by twice ion implantation in n-n-n heterogeneous material. Due to the directions of two wavelengths photoelectric diodes are the same, two light signals does not need to be separated. Therefore, its readout circuit structure is relatively simple. The theoretical spectral curve of Rockwell structure is shown in Fig. 2.54, and its structural parameters are listed in Table 2.15.

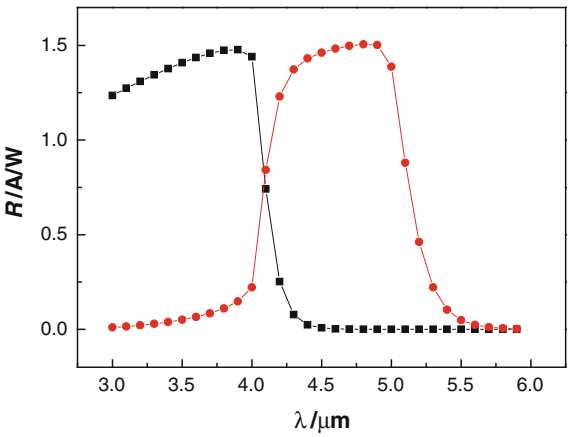

Fig. 2.54 The theoretical spectral curve of two-color detector based on p^+-on-n reported by Rockwell

Table 2.15 The structural parameters of two-color detector based on p^+-on-n reported by Rockwell

	Component	Doping (cm^{-3})	Thickness (μm)	Bandgap wavelength (μm)	SRH lifetime
n-window	0.42	n-type 1×10^{15}	1.2	2.86	1 μs
nMW1 absorption	0.342	n-type 1×10^{15}	6	4.0	
barrier	0.4	n-type 1×10^{15}	1	3	
nMW2 absorption	0.304	n-type 1×10^{15}	6.2	5.0	
n-cap	0.4	n-type 1×10^{15}	0.8	3.0	
p-implant	–	p-type 1×10^{17}	1.0	–	

Table 2.16 The quantum efficiency and spectral cross talk of four structures

	Quantum efficiency η		Spectral cross talk	
	MW1	MW2	C_{12} (%)	C_{21} (%)
HRL structure	64.2	52.7	0.02	7.76
BAE structure	66.3	56.4	0.02	8.12
LETI structure	64.2	55.7	0.02	8.14
Rockwell structure	48.1	38.9	0.02	7.5

In conclusion, the quantum efficiency and spectral cross talk of these various structures are listed in Table 2.16. C_{12} is defined for the cross talk of MW1 to MW2 (incident light wavelength is 4.8 μm). C_{21} is defined for the cross talk of MW2 to MW1 (incident light wavelength is 3.8 μm). It is obvious that the cross talk of MW2 to MW1 can be ignored, but MW1 to MW2 is too large. The main reason is that the absorption layer of MW1 is not thick enough, so that too much light is

allowed to enter MW2 through MW1. A possible solution is increasing the absorption layer thickness of MW1 to reduce the optical cross talk. However, this may reduce the quantum efficiency of MW1 and R_0A at the same time. Therefore, it is very necessary to design the best absorption layer thickness of MW1by theoretical calculation.

The performance of BAE structure is proved to be the best, according to the calculation results of the quantum efficiency, but this kind of structure is strongly dependent on the growth of the material. Therefore, the LETI structure may be most feasible, considering the requirements of device fabrication. If there are no specific notations, the two-color HgCdTe infrared detectors discussed in this section refer to the LETI structure.

2.2.4.2 Numerical Simulation of Spectral Photoresponse

Integrated as a single pixel in a focal plane array, a two-color detector has the ability to detect two spectral bands separately and independently, with high temporal and spatial coherence. When used to acquire infrared images, this type of detector provides an additional dimension of contrast that is available for signal processing and serves as a visual aid in scene interpretation, allowing determination of both absolute temperature and unique signatures of the objects from the background [78]. Several research groups have already presented interesting results on two-color focal plane arrays over the entire 2–12 μm wavelength region [67, 78–80].

HgCdTe two-color n–p–p–p–n photodetector arrays have recently been reported in Ref. [72, 81]. At 78 K, the measured SWIR and MWIR photodiode cut-off wavelengths are consistent with the expected configuration of the device. The calculated full width half maximum (FWHM) of the short wavelength (SW) spectrum is quite small, with the shape of the SW photoresponse being narrow and sharp. This phenomenon is also known as the 'short wavelength narrow effect'.

Figure 2.55 is the schematic of the n^+-p-p-p-n two-color infrared detector. Under back-illumination, the bottom *pn* junction ($x = 0.4$) absorbs SW radiation for wavelengths up to its cut-off value. This *pn* junction also acts as a transparent window for mid-wavelength light to pass through and be absorbed by the top n^+-p junction with the MW cutoff. The specific details of the detector, such as the doping densities, composition, thickness of each epilayer, etc., are listed in Table 2.17.

The spectral responsivity of the two-color infrared detector was measured with the samples held at 78 K using an NEXUS 670 FTIR spectral measurement system with a specific external optical path setup. Figure 2.56 shows the spectral photoresponse for the integrated HgCdTe two-color infrared detector illustrated in Fig. 2.55 where the corresponding two spectral bands with cut-off wavelengths of 3.04 and 5.74 μm are evident. Firstly, it can be observed that the cut-off wavelength of the SW photovoltaic diode is close to the cut-on wavelength of the MW photovoltaic diode. This effectively enables the SW photovoltaic diode to not only

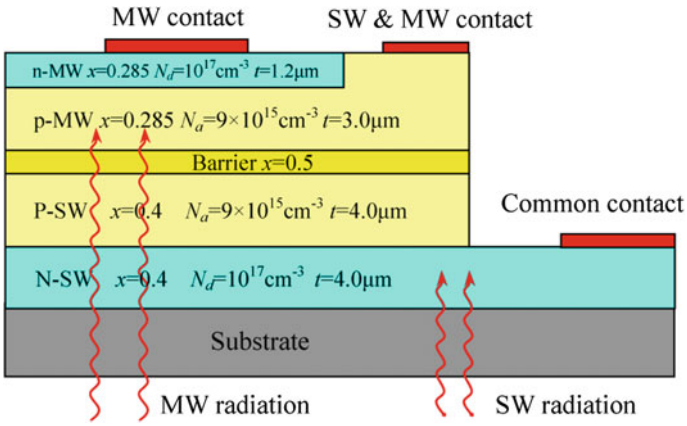

Fig. 2.55 Schematic of n^+-p-p-p-n HgCdTe two-color infrared detector

Table 2.17 Material and structural parameters of the two-color $Hg_{1-x}Cd_xTe$ photodetector

Parameters (SW)	Value (Units)	Parameters (MW)	Value (Units)
Cd molar fraction (x) of N region	0.4	Cd molar fraction (x) of N region	0.285
Cd molar fraction (x) of P region	0.4	Cd molar fraction (x) of P region	0.285
Temperature	77 (K)	Temperature	77 (K)
SRH lifetime for electron and hole	τ (ns)	SRH lifetime for electron and hole	τ (ns)
Doping density of N region	1×10^{17} (cm^{-3})	Doping density of N region	1×10^{17} (cm^{-3})
Doping density of P region	9×10^{15} (cm^{-3})	Doping density of P region	9×10^{15} (cm^{-3})
Thickness of N region	4 (μm)	Thickness of N region	1.2 (μm)
Thickness of P region	4 (μm)	Thickness of P region	3 (μm)

absorb and respond to the SW radiation, but also acts as a window for any MW radiation.

To further study the physical mechanism of the spectral response, two-dimensional numerical simulations using Sentaurus Device was carried out. For plain drift–diffusion simulation, the well-known Poisson equation and continuity equations are used. The carrier generation–recombination process consists of Shockley–Read–Hall, Auger and optical generation–recombination terms. Additionally, tunneling effects such as band-to-band and TATs are included in the continuity equations by incorporating them as additional generation–recombination processes. Comparison of the simulation results with different interface generation–recombination velocities and carrier lifetimes in the highly doped n region are presented in Fig. 2.57. The value of minority carrier lifetime in the bottom n-SW

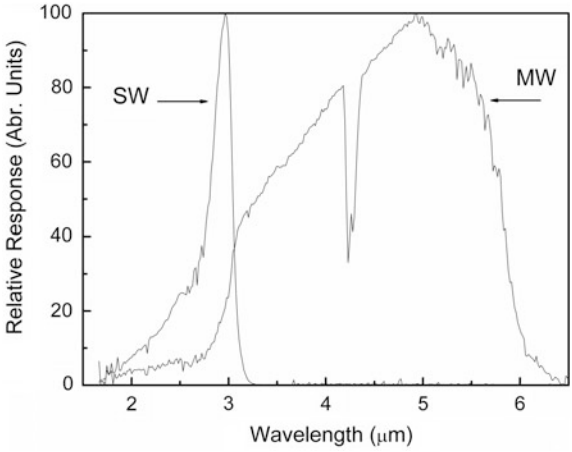

Fig. 2.56 Experimentally measured spectral photoresponse of preliminary integrated HgCdTe two-color infrared detector

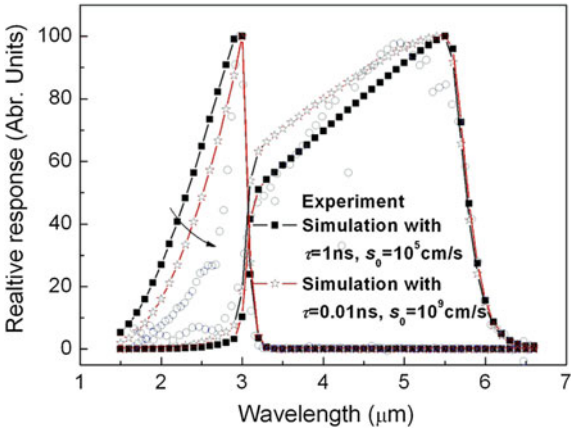

Fig. 2.57 Spectral photoresponse of a newly proposed integrated HgCdTe two-color infrared detector employing a heterostructure SW *pn* junction in place of the homostructure SW *pn* junction. The unfilled circles represent the experimental data and the solid lines with symbols represent the simulation results. τ is the maximum carrier lifetime, and s_0 is the surface recombination velocity in the bottom n layer

layer is assumed as 0.1 ns in the simulation. The simulated photoresponse with high interface generation–recombination velocity and short carrier lifetime is in good agreement with the experimental data, reaffirming the validity of the above analysis as well as providing an additional avenue for further device performance improvement through simulations.

Due to the high generation–recombination velocity at the buffer interface and short carrier lifetime of the highly doped *n* region, photogenerated carriers undergo significant recombination at the interface region which induces the short wavelength narrow effect of the integrated HgCdTe two-color infrared detector. A reasonable solution is to change the bottom *pn* junction from the homostructure to a heterostructure. This should enable SW radiation to transmit through the highly doped bottom *n* region and be absorbed in the low-doped *P* region which is further away from the buffer interface, hence reducing undesirable interface effects on the photo-generated carriers. Figure 2.58 illustrates a schematic of the proposed

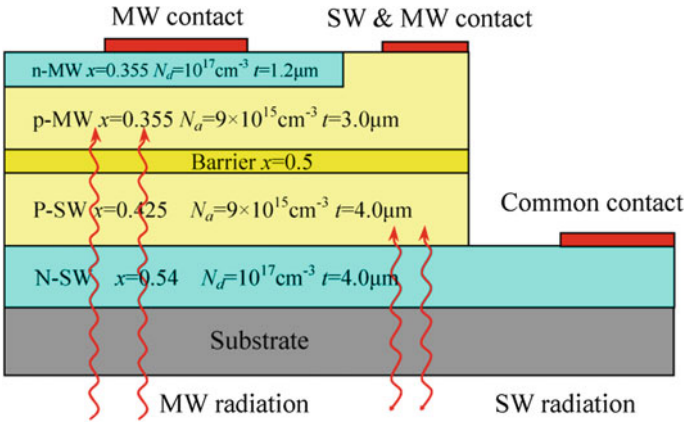

Fig. 2.58 Schematic of proposed heterostructure n^+-p-p-p-n HgCdTe two-color infrared detector incorporating a SW pn heterostructure in place of the SW pn homostructure

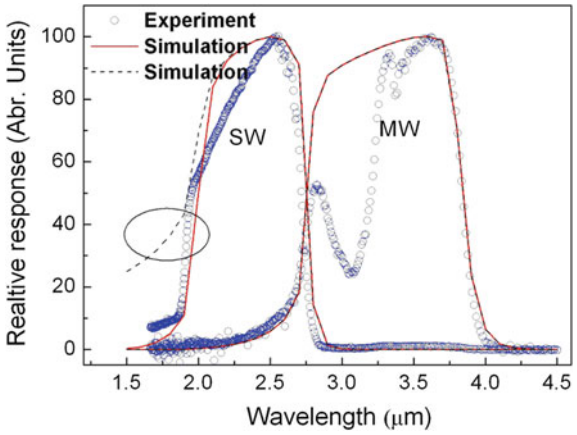

Fig. 2.59 Spectral photoresponse of a newly proposed integrated HgCdTe two-color infrared detector employing a heterostructure SW pn junction in place of the homostructure SW pn junction. The unfilled circles represent the experimental data while the *solid* and *dashed lines* represent the simulation results. The maximum carrier lifetime in the simulation for the solid line is 0.1 ns for the bottom *n* layer and 10 ns for the other layers. The maximum carrier lifetime in the simulation for the dashed line is 10 ns for the bottom *n* layer and the other layers

structure where the heterostructure of the bottom *pn* junction consists of a bigger energy gap *n* region with high doping density and a smaller energy gap *P* region with low doping density. Figure 2.59 shows the spectral photoresponse of the newly proposed integrated HgCdTe two-color infrared detector with a heterostructure SW *pn* junction with device parameters given in Fig. 2.58. The proposed integrated HgCdTe two-color infrared detector with a heterostructure SW *pn* junction has a much larger FWHM than that of the initial integrated HgCdTe two-color infrared detector, resulting in an increase in device performance.

High temporal and spatial coherent simultaneous long wavelength/mid-wavelength (LW/MW) two-color focal plane array (FPA) infrared detection is the cutting-edge technique for third-generation infrared remote sensing [82–84]. HgCdTe LW/MW two-color infrared detectors were designed and fabricated [82]. The top long wavelength and bottom mid-wavelength infrared planar photodiodes are processed by selective B^+-implantation after etching the long wavelength epi-layer into a curvature and exposing the mid-wavelength layers for the implantation of the *n* region of the MW photodiode by a micro-mesa array technique. Non-planar boron ion implantation and metallization are developed by using photoresist spray coating technology for the two-color HgCdTe IR detector. Figure 2.60a shows the schematic of two-color LW/MW HgCdTe photovoltaic detector with an n_1^+-p_1-p-p_2-n_2^+ architecture. Under back-illumination, the bottom p_2-n_2^+ junction absorbs MW

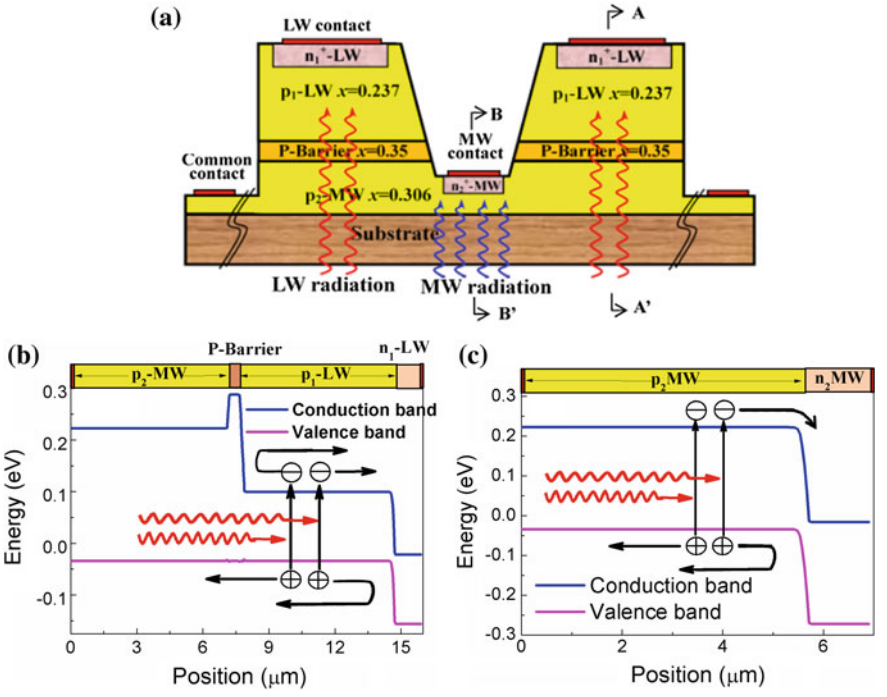

Fig. 2.60 **a** Schematic of grooved HgCdTe two-color infrared detector. **b** Equilibrium energy band diagram cut at A-A′. **c** Equilibrium energy band diagram cut at B-B′

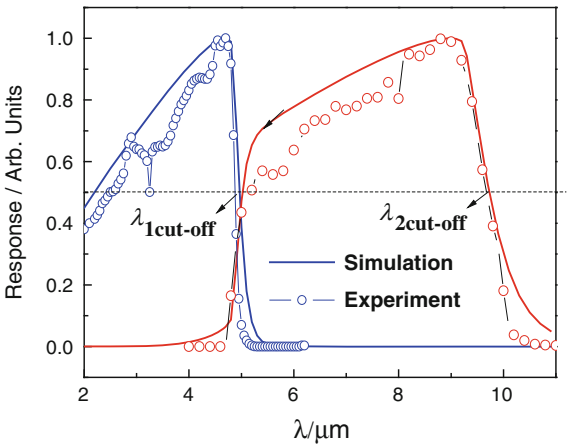

Fig. 2.61 Experimental (*dotted*) and simulated (*solid*) spectral photoresponse of LW/MW HgCdTe two-color infrared detector with cut-off wavelengths of $\lambda_{1cut\text{-}off}$ = 4.8 μm and $\lambda_{2cut\text{-}off}$ = 9.7 μm for the LW and MW diodes respectively. A voltage of 0.01 V is used in simulation and experiment

radiation for wavelengths up to its cut-off value. This p-type layer junction for MW light also acts as a transparent window for LW light to pass through and be absorbed by the horizontal n_1^+-p_1-P-p_2 junction with LW cutoff, as shown in Figs. 2.60b, c.

Figure 2.61 shows the spectral photoresponse for the HgCdTe two-color infrared detector with the proposed structure from the numerical simulations. The cut-off wavelengths of the LW and MW diode are 4.8 and 9.7 μm, respectively. It can be observed that the cut-off wavelength of the MW diode is close to the cut-on wavelength of the LW diode. This effectively enables the MW diode to not only absorb and respond to the MW radiation, but also acts as a window for any LW radiation. The simulated spectral photoresponse is also compared to that of experimental results showing that the simulation and experiment are self-consistently in good agreement. The calculated peak detectivity is 3.2×10^{11} and 4.3×10^{10} $cmHz^{1/2}$ for the MW and LW photodiodes, respectively. The proposed LW/MW HgCdTe two-color structure is very promising for third-generation intelligent infrared imaging.

2.2.4.3 The Relationship of Spectral Response with Minority Carrier Lifetimes

Integrated HgCdTe two-color infrared device, with multilayer heterojunction structure, is developed based on monochromatic infrared device. Composition, doping concentration distribution and thickness of each layer are needed to be designed precisely. This type of device technology is more complicated than for a monochromatic device, greatly increasing the difficulty of device performance control. Ballet [80], Ferret [85], Baylet [86], etc. studied the fabrication process and performance characterization of two-color devices. Jozwikowski and Rogalski [87] calculated the photoelectric gain and the noise of two-color devices. The spectral responses of a two-color device as a function of temperature are simulated by

Bellotti et al. [88]. However, in addition to the device response and noise characteristics of the specific structure, the other key material factors and structure parameters on the devices also require in-depth research. This research can provide a theoretical guide for optimizing device performance and fabrication control parameters such as the relationship between the performance of a HgCdTe two-color device and the lifetime of minority carriers, the components of the barrier layer for inhibiting electrical cross talk, etc. The basic structure of HgCdTe two-color device is shown in Fig. 2.60.

The spectral response and quantum efficiency characteristics of a two-color device with different SRH lifetimes are shown in Fig. 2.62a, b. Under the same SRH recombination lifetime, the quantum efficiency of the MW2 band is significantly below that of the MW1 band The main reason for this is that the duty ratio of MW2 (75 %) is lower than that of MW1 (nearly 100 %). Figure 2.62c illustrates the relationship of quantum efficiency to SRH recombination lifetime under the typical wavelengths of MW1, MW2 band. It is shown that the quantum efficiency is strongly dependent on the SRH recombination lifetime. When the SRH lifetime is less than 10 ns, the quantum efficiency drops quickly with the SRH lifetime, the quantum efficiency of MW1 band is reduced by more than 30 % when the SRH lifetime drops from 10 to 1 ns, while the quantum efficiency of MW2 band is

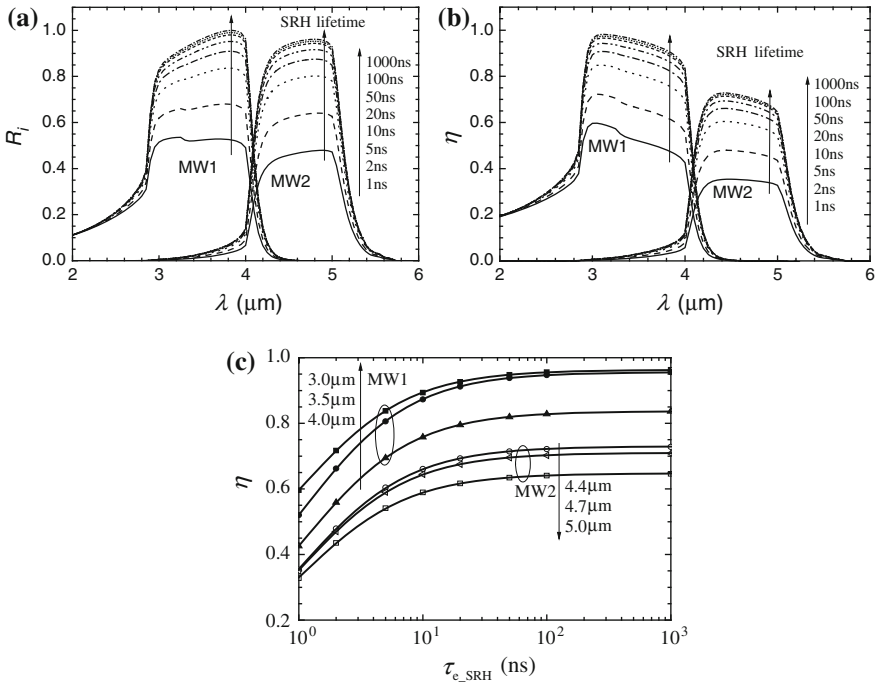

Fig. 2.62 The spectral response of two-color detector varies with the SRH electronic lifetime in p zone. **a** Spectral response R_i, **b** Quantum efficiency η, **c** The relationship between the quantum efficiency and the SRH electronic lifetime (*Dotted lines* represent the results of simulation calculation, *solid lines* represent the fitting results using formula (2.52))

reduced by almost 50 %; when the SRH lifetime varies between 100 and 10 ns, the quantum efficiency of MW1 and MW2 bands are both little changed.

According to the SRH recombination lifetime, the total life τ_e and diffusion length L_e of the electron can be calculated as:

$$\frac{1}{\tau_e} = \frac{1}{\tau_{e\_R}} + \frac{1}{\tau_{e\_Auger}} + \frac{1}{\tau_{e\_SRH}} \tag{2.52}$$

$$L_e = \sqrt{\frac{kT}{q}\mu_e\tau_e} \tag{2.53}$$

where τ_{e_R}, τ_{e_Auger} are the Radiation recombination lifetime and Auger recombination lifetime, μ_e is the electron mobility, and K, T, q are the Boltzmann's constant, temperature, and basic charge respectively. The Radiative and Auger recombination lifetime of HgCdTe material are the function of temperature and components, and have nothing to do with the technology process. However, the recombination lifetime of SRH is closely related to the technology process.

2.2.4.4 The Relationship of Cross Talk with the Barrier Layer

As can be seen from the response in Fig. 2.62, the cross talk of MW1-to-MW2 is greater than that of MW2-to-MW1 under the different carrier lifetimes. There are two formation mechanisms of the cross talk: optical cross talk and electrical cross talk. Optical cross talk is caused by the absorption of MW1 radiation in the MW2 area. The optical cross talk has been discussed in detail in Chap. 1, therefore the focus here is to study the electrical cross talk problem.

The spectral responses of the two-color device (see Fig. 2.63) with different barrier layer components (Δx_b) are shown in Fig. 2.64. Δx_b is defined as the

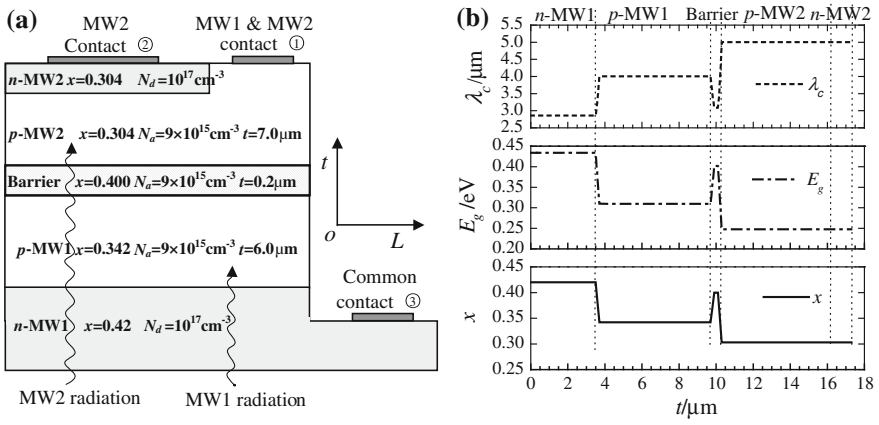

Fig. 2.63 The structure of two-color detector. **a** The structure of n-p-p-p-n $Hg_{1-x}Cd_xTe$ two-color detector, **b** Device component x, forbidden band width E_g and the cutoff wavelength λ_c varies with the direction of thickness

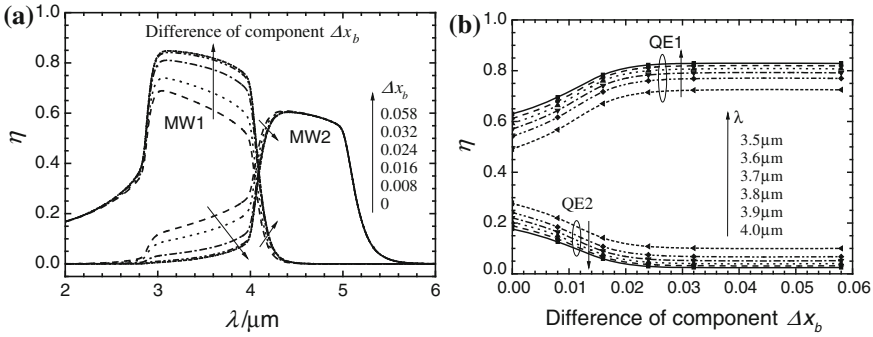

Fig. 2.64 The spectral response (quantum efficiency) of two-color device with different difference of component. **a** Spectral response; **b** Quantum efficiency varies with the difference of barrier layer components Δx_b

difference between the highest composition x_b of barrier layer and that of p-MW1 area. It is evident from Fig. 2.64 that the component of the barrier layer has an important effect on the quantum efficiency of MW1 band (3.0–4.0 μm): the quantum efficiency of MW1 increases with the component of barrier layer, while the quantum efficiency of MW2 decreases with the component of barrier layer. The quantum efficiency changes when Δx_b varies from 0 to 0.02 although it remains unchanged when Δx_b exceeds 0.03; when Δx_b varies from 0 to 0.032, the quantum efficiency of MW1 is increased from 49 to 72 % at the radiation wavelength of 4.0 μm, while for MW2 it is decreased from 28 to 10 %. The output ratio of MW2 to MW1 is known as the cross talk of MW1 to MW2. For incident light in MW2 band (4.4–5.0 μm), the spectral response has nothing to do with the component of barrier layer. Therefore, the design of the barrier layer is only related to the incident light in the MW1 band.

As mentioned previously, incident light in MW1 band is absorbed in the p-MW1 area and the photogenerated electrons may diffuse into either the MW1 junction or MW2 junction. If the photogenerated electrons diffuse into the MW2 junction, this results in the electrical cross talk of the MW1 to MW2 signal. However, if there are any barrier layers, the diffusion of electrons from p-MW1 to p-MW2 area will be restrained, and cross talk is reduced. That is why the barrier layer is introduced in the middle of a two-color device (see Fig. 2.62). The different components of the conduction band barrier layer are shown in Fig. 2.65 under the equilibrium state. The barrier height is calculated:

$$\Delta V_b \approx \Delta E_g = E_{g\_b} - E_{g\_pMW1} \tag{2.54}$$

where ΔV_b is defined as the difference of the conduction band between barrier layer and p-MW1 diffusion zone, and ΔE_g is the difference of the band gap between barrier layer (E_{g_b}) and p-MW1 diffusion zone ($E_{g\_p\text{-}MW1}$). Therefore, ΔV_b and ΔE_g

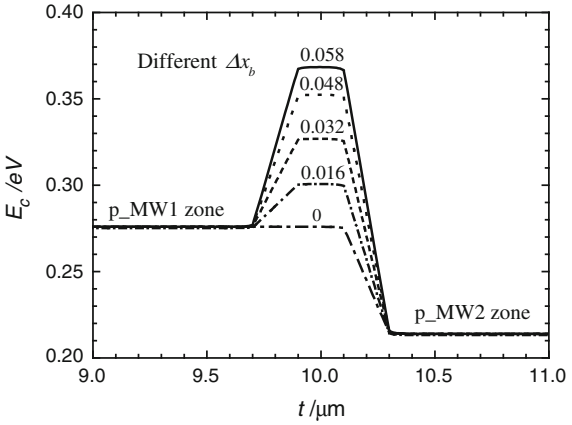

Fig. 2.65 The formation of the barrier with different components of barrier layer in the conduction band under equilibrium

are obviously dependent on the different components between the barrier layer and p-MW1 area (Δx_b). For HgCdTe material, ΔV_b and ΔE_g are approximately linear to Δx_b. In the device simulation, the transition of components is introduced at the interface between the barrier layer and p-MW1, p-MW2 area, which is consistent with the actual device. The thickness in the barrier layer is 0.2 μm in the simulation.

In order to accurately study the relationship of cross talk with the barrier layer's components (x_b), the cross talk with different barrier layer's components is calculated in detailed under laser illumination with the representative wavelength of 3.5, 4.0 μm in MW1 band. As shown in Fig. 2.66, the barrier height ΔV_b with each component in the barrier layer is obtained. Figure 2.65 shows the formation of the barrier in the conduction band with different components of barrier layer under equilibrium state.

To ensure the cross talk caused by carrier diffusion is maximally suppressed, theoretical results show that the component of barrier layer x_b should be at least 0.03 higher than that of p-MW1 area for the two-color device (see Fig. 2.63). For

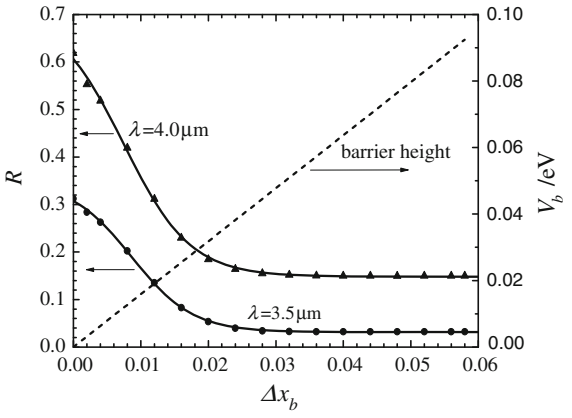

Fig. 2.66 The cross talk of MW1-to-MW2 (R) with the barrier height (ΔV_b) and the difference of component (Δx_b)

the design of the barrier layer's components in the actual device, the only applied standard is that the electrical cross talk should be far less than the optical cross talk.

2.2.4.5 The Optimum Thickness of the Absorption Layers

Compared with monochromatic devices, multicolor detectors are unique from the performance indicators to the device structure. Absorption layers of p-MW1 and p-MW2 are the locations where the incident light is absorbed and translated into electrical signals. The parameters of the absorption layers directly affect the performance of the device, including the material and device parameters such as components, minority carrier lifetime, the thickness of absorption zone, etc.

According to the previous discussion, as long as the components of barrier layer are appropriately designed, the electrical cross talk can be greatly reduced, even negligible. In this case, the optical cross talk becomes the component of the total cross talk. The thickness of the absorption zone has an important influence on the optical cross talk and the quantum efficiency of two-color device. This section mainly studies the optimization of the absorption area from two aspects: the quantum efficiency and cross talk (optical).

The optimization of the absorption area is analyzed under an ideal condition: the lifetime of SRH recombination is assumed to be very long, so that the main process of recombination is determined by the Radiative recombination, and Auger recombination. In this simulation, the barrier layer is high enough ($\Delta x_b = 0.058$) so that the electrical cross talk is completely suppressed. The spectral efficiency of the two-color device with different thickness of p-MW1 absorption area is shown in Fig. 2.67. For the back-illuminated n-p-p-pn two-color structure, shortwave radiation passes from p-MW1 to p-MW2 area. It is first absorbed in the p-MW1 area, and then the remainder is absorbed in p-MW2 area.

It is observed that with an increase in the thickness of p-MW1, more light is absorbed and a larger the signal from the MW1 is obtained. However, less infrared radiation reaches p-MW2, and a smaller signal of MW2 is obtained. The quantum efficiency of MW1 gradually moves closer to 100 % with the increase of the thickness of p-MW1 under the laser wavelength of 3–4 μm in the MW1 band, as shown in Fig. 2.67c. When the thickness of p-MW1 is about 8 μm, the rate of increase in quantum efficiency of MW1 slows until it becomes static. Therefore, in order to ensure that the internal quantum efficiency of MW1 is above 90 %, the thickness of p-MW1 should be 8–10 μm.

The spectral efficiency of the two-color device with different thickness of p-MW2 absorption area is shown in Fig. 2.68. According to the previous theoretical analysis, the thickness of MW1 is chosen as 10 μm in the calculation. Compared with the case of p-MW1 zone, the thickness of p-MW2 zone only affects the quantum efficiency of MW2, and makes little impact on the quantum efficiency of MW1. It is found that the greater the thickness of p-MW2, the larger the quantum efficiency of MW2. When the thickness of p-MW2 zone varies from 4 to 7 μm, the quantum efficiency of MW2 will increase quickly; when the thickness of p-MW2 is

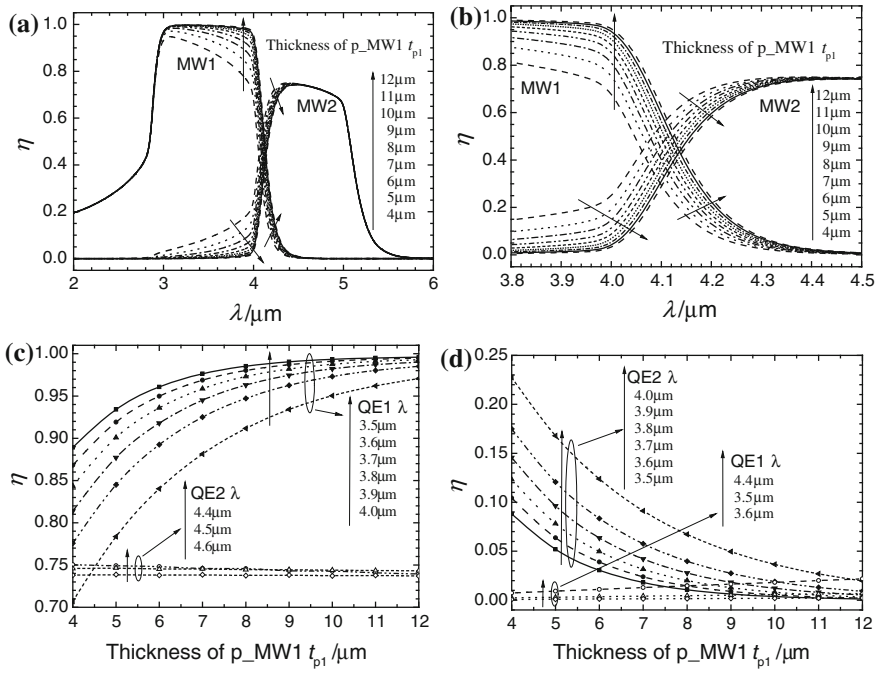

Fig. 2.67 The quantum efficiency with different thickness of p-MW1 zones. **a** Spectral response, **b** A magnified view of the middle of Spectral response, **c** Quantum efficiency along with the thickness of p-MW1 zone under the key radiation wavelength, **d** The quantum efficiency with the thickness of p-MW1 zone under the specific radiation wavelength, which has an effect on the cross talk

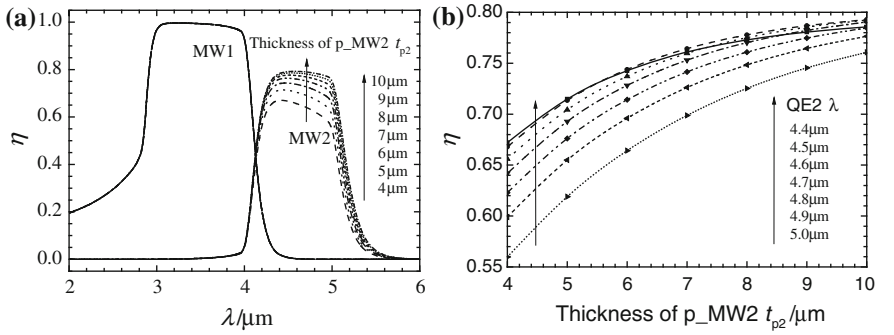

Fig. 2.68 The quantum efficiency with different thickness of p-MW2 zones. **a** Spectral response, **b** Quantum efficiency along with the thickness of p-MW2 zone under the key radiation wavelength in MW2 band

about 8 μm, the increasing trend of quantum efficiency will slow down. However, in addition to part of the transverse junction, the MW2 zone also owns part of longitudinal junction (see Fig. 2.63). Actually, the illumination area is greater than the *pn* junction area. Therefore, the right side of diode in the MW2 zone also has a contribution to quantum efficiency, and the quantum efficiency of MW2 may finally be more than 75 %.

On the other hand, for the MW2 diode, medium wave radiation is mainly absorbed in the p-MW2 area near the substrate region. The greater the thickness of the p-MW2 area, the more the absorption center is further away from the junction area, and the minority carrier (electrons) are easier to be lost due to the recombination, which results in the decrease of quantum efficiency of MW2 with the thickness of p-MW2 area.

The relationship of cross talk to the thickness of p-MW2 zone is shown in Fig. 2.69. The cross talk of MW1-to-MW2 increases slightly with the thickness of p-MW2 zone, the reason is that the quantum efficiency of MW2 increases slightly with the thickness of p-MW2 under the laser wavelength of MW1 band. On the other hand, the cross talk of MW2-to-MW1 decreases with the thickness of p-MW2 zone, the reason is that the quantum efficiency of MW1 has nothing to do with the thickness of p-MW2 under the laser wavelength of MW2 band, but, the quantum efficiency of MW2 increases with the thickness of p-MW2 zone. Therefore, the ratio of the former to the latter (cross talk) decreases with the thickness of p-MW2 zone.

Taken as a whole, the cross talk of MW1-to-MW2 and MW2-to-MW1 both changes little with the thickness of p-MW2 zone. In conclusion, the optimization of p-MW2 thickness can be based on the quantum efficiency of MW2. According to the above analysis, together with the principle of reducing device thickness as far as possible, p-MW2 with a thickness of 8 μm is a reasonable choice. The quantum efficiency of MW2 is over 70 %, the monochromatic cross talk of MW1-to-MW2 and MW1-to-MW2 are less than 3.9 and 2.4 %, as shown in Fig. 2.70.

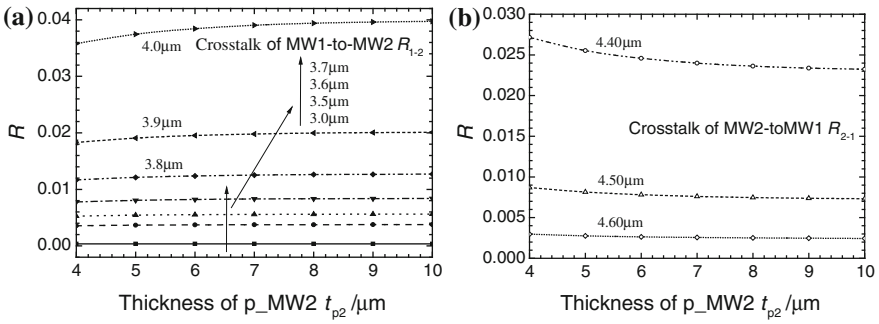

Fig. 2.69 The cross talk with different thickness of p-MW2 zone. **a** The cross talk of MW1-to-MW2; **b** The cross talk of MW2-to-MW

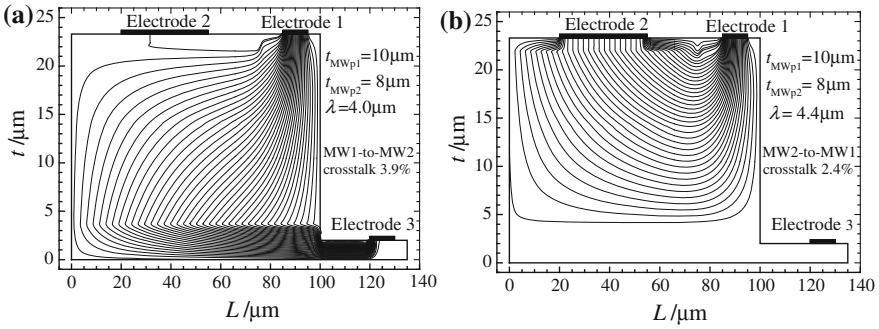

Fig. 2.70 The distribution of photocurrent in device under the optimized thickness of absorption zone. **a** λ = 4.0 μm, **b** λ = 4.4 μm

2.3 Methods of Extracting Parameters from HgCdTe Materials and Chips

2.3.1 Extracting Device Parameters by Electrical Method

Either a current–voltage (*I–V*) curve or a resistance–voltage(*R–V*) curve is a standard characterization to quantify the dark current performance of a HgCdTe photovoltaic detector. One can obtain *R–V* characteristics by mathematical differential calculations from *I–V* characteristics which are measured by experiments, and also can obtain *R–V* characteristic directly by implement differential signal from the experiment. As is known, the properties of HgCdTe photodiodes can be improved by minimizing dark current. Therefore, it is important to quantitatively analyze *I–V* or *R–V* curves to obtain device parameters and reveal roles of the different physical mechanisms of the parameters in HgCdTe photodiodes.

2.3.1.1 Extract Device Parameters for Long Wavelength HgCdTe Photodiodes

At present, the typical fitting process for the *I–V* or *R–V* curves are empirically made to extract parameters in a sequential mode [89–91]. Various dark current mechanisms are used in different bias regions in which they have the dominant effect on the fitted curve. However, many HgCdTe photodiodes have more than one mechanism in most bias regions having comparable effects on the fitted curve. Then the extract parameters by the sequential mode will have large error. A method that could fit the *R–V* curves simultaneously in all bias regions will be valuable to device designers. Few studies on the simultaneous fitting approach have been reported on *R–V* curves analysis, owing to its time-consuming procedure and the multi-minimum problem in mathematics. Moreover, the errors of the extracted

parameters have not been analyzed in the previously published works, although it is very important for the estimation of the quality of HgCdTe photodiodes. In this chapter, a data processing technique in the simultaneous mode [92] has been developed. It is shown that this method can be used to fit the *R–V* curves of long wavelength HgCdTe n-on-p photodiodes for the determination of the device parameters and their errors.

The measured *I–V* curves generally include photocurrent due to the background illumination. Based on the assumption of low photon injection, the photocurrent can be regarded as bias-independent [93]. The *R–V* curves of illuminated photodiodes are the same as those of unilluminated ones. Therefore, the *R–V* curves are taken to be the fitting object in our fitting process. Then the effects of the current offsets in the device will be eliminated in our fitting procedure. The measured *R–V* curves of HgCdTe photodiodes are fitted by a dark current model including diffusion current (I_{diff}), generation–recombination current (I_{gr}), trap-assisted tunneling current (I_{tat}), and band-to-band tunneling current (I_{bbt}).The bias voltage is an effective bias $V_e = V_d - I \times R_s$ corrected by the series resistance R_s. Here, V_d is the applied voltage, I is the total dark current, and R_s is the series resistance. The total dynamic resistance is given as:

$$R_{\text{fit}} = \left(\frac{1}{R_{\text{diff}}} + \frac{1}{R_{\text{gr}}} + \frac{1}{R_{\text{tat}}} + \frac{1}{R_{\text{bbt}}} \right)^{-1} + R_s \tag{2.55}$$

At present, the mainstream of HgCdTe focal plane detector design is n-on-p diodes. These diodes are fabricated using n-type boron ion implantation on mercury vacancy doped HgCdTe material. For planar n-on-p HgCdTe photodiodes, there are six fitting parameters to be extracted from *R–V* curves as follows: the dopant density N_d in *n*-region, the ratio of mobility to lifetime of electrons μ_n/τ_n in *p*-region, the effective lifetime τ_0 in the depletion region, the relative energy position of trap level E_t/E_g and its density N_t in the depletion region, and the series resistance R_s. A theoretical *R–V* curve can be obtained from substituting a set of the six parameters into Eq. (2.55). In our fitting procedure, the algorithm is to minimize the function value of $F = \sum_{i=1}^{N} \left[\log(R_{\text{fit}}(V_{d\,i})) - \log\left(R_{\text{exp}}(V_{d\,i})\right) \right]^2$, where R_{exp} is the experimental data, and N is the number of data. An initial value should be input first, and then the parameters vary in the their corresponding range to minimize the fitting variance F by using a standard nonlinear gradient search method combined with the algorithm of reconstruction of the whole-region-minimum for *N*-dimensional function [94]. Figure 2.71 is the flowchart of the fitting procedure. Through such a process, we can obtain a theoretical *R–V* curves which correspond to the experiment as well as a set of fitting parameters. The range of error is difficult to determine due to the fact that F is a multi-valued minimum function consisting of six parameters in six dimensional space and the fitting parameters will change when the initial value is varied through this method. Moreover, the range of these parameters is large, and the fitting time also increases accordingly, so looking for a quick and accurate fitting approach is necessary.

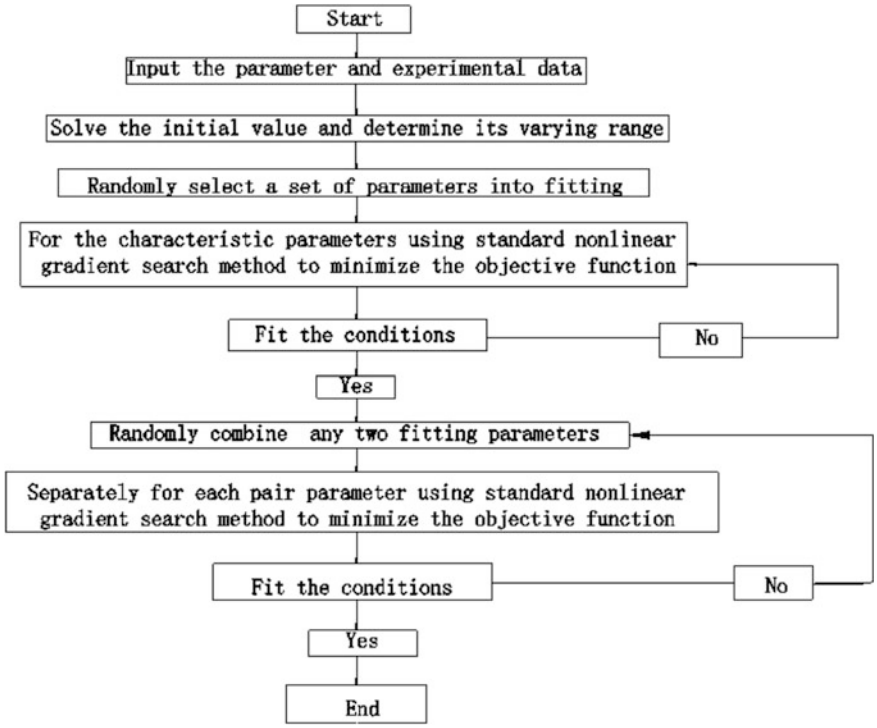

Fig. 2.71 Flow chart of the fitting procedure

For the first step in the fitting process, one must determine the initial values of the fitting parameters carefully. According to Eq. (2.55), the following equation comes into existence for each bias value:

$$R_{\text{exp}} - \left(\frac{1}{R_{\text{diff}}} + \frac{1}{R_{\text{gr}}} + \frac{1}{R_{\text{tat}}} + \frac{1}{R_{\text{bbt}}}\right)^{-1} - R_{\text{s}} = 0 \tag{2.56}$$

There are six unknown variables in this equation, namely six fitting parameters. A set of six variable equations is obtained by choosing six characteristic points on the measured R–V curve. The initial values of the six fitting parameters can be determined by solving these equations set with the method of iteration based on the Taylor series expanded nonlinear terms. A given set of initial values is still needed for the iteration. A fault-tolerant problem in the iteration may lead to a divergent solution once these initial values deviate from the solution to a certain extent. Therefore, it is impractical to directly solve the equations set.

In order to solve Eq. (2.56) for initial values, we use the sequential mode algorithm because it is well known that the four dark current mechanisms have different contributions to the dark current under different biases. Generally, for long

wavelength HgCdTe diodes, I_{diff} dominates the dark current under a large forward bias; I_{gr} becomes dominant near zero forward bias; I_{tat} has the largest contribution under middle reverse bias; and I_{bbt} dominates under large reverse bias. The series resistance R_s, which is comparable to the junction resistance only under a large forward bias, can be omitted in the initial value determination. Then, Eq. (2.56) can be solved as follows.

First, I_{bbt} is only related to the dopant density N_d in n-region. In the large reverse bias region, I_{bbt} dominates the dark current. Equation (2.56) can be replaced by

$$R_{exp} - R_{bbt} = 0 \tag{2.57}$$

Substituting a measured point in the large reverse bias region into Eq. (2.57) with one variable, the initial value of N_d is obtained.

Likewise, for the large forward bias region, I_{diff}, which depends on N_d and μ_n/τ_n, is the dominant dark current. Equation (2.56) can be simplified as

$$R_{exp} - R_{diff} = 0 \tag{2.58}$$

Substituting N_d and a measured point in the large forward bias region into Eq. (2.58) with one variable, the initial value of μ_n/τ_n is obtained.

For the small forward bias region, the combination of I_{diff} and I_{gr} dominates the dark current. Equation (2.56) is approximated as

$$R_{exp} - \left(\frac{1}{R_{diff}} + \frac{1}{R_{gr}}\right)^{-1} = 0 \tag{2.59}$$

I_{gr} is related to N_d and the effective lifetime τ_0 in the depletion region. Substituting N_d, μ_n/τ_n and a measured point in the small forward bias region into Eq. (2.59) with one variable, the initial value of τ_0 is obtained.

Finally, for the middle reverse bias region, the combination of I_{gr}, I_{tat} and I_{bbt} dominates the dark current. From Eq. (2.56) one has

$$R_{exp} - \left(\frac{1}{R_{gr}} + \frac{1}{R_{tat}} + \frac{1}{R_{bbt}}\right)^{-1} = 0 \tag{2.60}$$

I_{tat} is related to N_d, the relative energy position of trap level E_t/E_g, and the trap density N_t. So Eq. (2.60) is a two-variable equation, which can be solved using a joint method of search and iteration. In the search process, for each value of E_t/E_g in the reasonable range (0.2–0.8) with the interval of 0.01, two values of N_t are obtained from Eq. (2.60) for two of the measured points in the middle reverse bias region. The searched value of E_t/E_g, for which the difference between the two values of N_t is the smallest, is assigned to be the initial value for the iteration method. Then in the iteration process, at step-1, N_t is obtained by substituting N_d, τ_0, E_t/E_g and one measured point in the middle reverse bias region into Eq. (2.60). At step-2, a new E_t/E_g is obtained by substituting N_d, τ_0, N_t and another measured

point in the middle reverse bias region into Eq. (2.60). Then the step-1 is repeated by taking the new E_t/E_g obtained in the previous step-2 as a new initial value. This iteration loop does not stop until the solution comes to convergence. By so doing, the initial values of both E_t/E_g and N_t are obtained. Now we have obtained all the initial values for the six fitting parameters. Accordingly, the variation range for each parameter can be assigned. Typically, the upper limit of the variation range is twice of the initial value, and the lower limit is half of it.

To evaluate the fitting accuracy, the errors of the fitting parameters should be analyzed. The error of the dynamic resistance can be expressed by $\Delta R = |R_{fit}(V_d) - R_{exp}(V_d)|$. Assuming that this error is effectively resulted from one of the six fitting parameters, this parameter's error can be given as,

$$\sigma_{x_j} = \left|\frac{\partial R_{fit}}{\partial x_j}\right|^{-1} \cdot \Delta R \tag{2.61}$$

where, x_j is the six fitting parameters, and σ_{x_j} is the error of the parameter x_j. This value reflects the upper limit of the error for the fitting parameters to a certain extent.

The *R–V* curves of HgCdTe photodiodes, however, have the feature that the four types of dark current mechanisms have different contributions to the dark current under different biases. The error of μ_n/τ_n, for example, will be magnified if it is analyzed when I_{gr} dominates the dark current. This error will be even infinitely enlarged under large reverse bias. Therefore, the simple averaging of σ_{x_j} over the whole bias range is meaningless for evaluating the accuracy of the fitting parameters. The different bias regions at which each fitting parameter has the largest influence to the *R–V* curve should be ascertained. We define $\eta = \left|\frac{\partial R_{fit}(V_d)}{\partial x_j} \cdot \frac{1}{R_{fit}(V_d)}\right|$ as a criterion of the sensitivity. The larger the value of η is, the greater the influence on ΔR from the corresponding fitting parameter is. The average of σ_{x_j} for those biases is taken as the theoretical estimation error for the specific parameter x_j, where η is larger than half of its maximum.

To demonstrate the determination process of the fitting parameters errors and to verify its applicability, some artificial *R–V* curves, derived with the combination of the generated noise current and the calculated current with preassigned fitting parameters, are fitted as the experimental data by our fitting program. The differences between the fitting parameters obtained from the fittings and the preassigned parameters are defined as the real errors. The fitting results given in this work are the averaged results from ten fits in different fitting paths. Figure 2.72 shows the fitting results of the artificial *R–V* curves whose noise level is 1, 2, and 3 %, respectively. The material and device parameters, which are not used as fitting parameters, are summarized in Table 2.18, where x is the Cd composition, T is the measurement temperature, A is the junction area, N_a is the dopant densities at *p*-region, and μ_p is the mobility of excess holes. The voltage range for the fitting

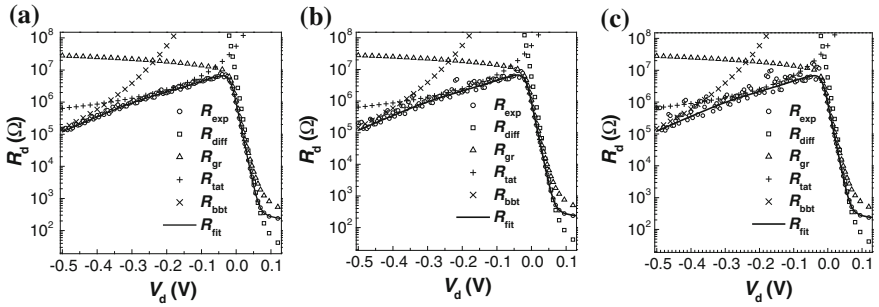

Fig. 2.72 Fitting results of the artificial *R–V* curves with the generated noise level of 1 % (**a**), 2 % (**b**), and 3 % (**c**). Reprinted with permission from Ref. [92] © 2006, American Institute of Physics

Table 2.18 Input parameters for the fitting program

X	N_a (cm^{-3})	μ_p (cm^2/Vs)	A (μm^2)	T (K)
0.233	8×10^{15}	633	28×28	77.4

Reprinted with permission from Ref. [92] © 2006, American Institute of Physics

Table 2.19 Comparisons of the assigned values of the six fitting parameters and the fitting results of the theoretically generated *R–V* curves whose noise level is 1, 2, and 3, respectively

	N_d (cm^{-3})	μ_n/τ_n ($cm^2/V\ s^2$)	τ_0 (ns)	E_t/E_g	N_t (cm^{-3})	R_s (Ω)
Assigned	1.676×10^{16}	9.51×10^{13}	0.207	0.491	1.968×10^{12}	200
Noise 1 %	1.683×10^{16}	1.05×10^{14}	0.192	0.4889	1.988×10^{12}	205.2
	(6×10^{12})	(1×10^{12})	(0.001)	(0.0004)	(1×10^{10})	(0.2)
Noise 2 %	1.676×10^{16}	9.92×10^{13}	0.1834	0.4866	2.028×10^{12}	204.2
	(5×10^{12})	(9×10^{11})	(0.001)	(0.0003)	(9×10^{9})	(0.2)
Noise 3 %	1.667×10^{16}	1.008×10^{14}	0.1843	0.4869	1.962×10^{12}	204.6
	(3×10^{12})	(3×10^{11})	(0.0003)	(0.0001)	(3×10^{9})	(0.1)

Data in brackets are the standard errors of the results from ten fits in different fitting paths) Reprinted with permission from Ref. [92] © 2006, American Institute of Physics

is –0.48–0.12 V. The assigned values and the fitting results of the fitting parameters are listed in Table 2.19.

Figure 2.72 shows the fitting results of the artificial *R–V* curves. It can be seen from Table 2.19 that when the noise level is smaller than 3 %, both the deviation of the fitting results from the assigned ones and the discreteness among the results from the ten fits in different fitting paths are very small. In this noise level, our data processing approach can give a good fitting precision for quantitative analysis of the *R–V* curves. Since the noise level is generally smaller than 3 % under regular experimental conditions, our fitting method is feasible in practice.

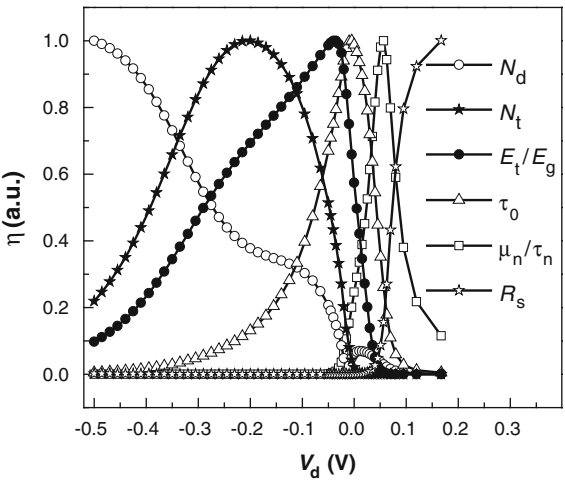

Fig. 2.73 Normalized sensitivity criterion (η) versus the bias for the six fitting parameters. Reprinted with permission from Ref. [92] © 2006, American Institute of Physics

Figure 2.73 shows the dependence of the normalized sensitivity criterion η on the bias. As one can see the largest η for each fitting parameter is located at a different bias region where its related dark current mechanism dominates the dark current. Accordingly, the estimation error for each fitting parameter can be obtained. The error range of the fitting parameters can be defined as follows: the standard error of the ten fits in different fitting paths (in Table 2.19) is regarded as the minimum possible error in the data processing procedures. Therefore, it is taken as the lower limit. The estimation error by Eq. (2.61) is regarded as the maximum possible error—the upper limit. The error ranges and the real errors for the fitting results of the artificial *R*–*V* curves, whose noise level are 1, 2, and 3 %, respectively, are listed in Table 2.20. All the real errors drop between the upper and lower limits. This indicates that the estimation errors calculated using this method can be used to represent the accuracy of the fitting parameters.

Table 2.20 Error ranges of the six fitting parameters of the theoretical *R*–*V* curves whose noise level is 1, 2, and 3 %, respectively

Error ranges	ΔN_d (cm^{-3})	$\Delta\mu_n/\tau_n$ ($cm^2/V\ s^2$)	$\Delta\tau_0$ (ns)	$\Delta E_t/E_g$	ΔN_t (cm^{-3})	ΔR_s (Ω)
Noise 1 %	(7×10^{13})	(1×10^{13})	(0.015)	(0.002)	(2×10^{10})	(5)
	6×10^{12} ~9×10^{14}	1×10^{12} ~3×10^{13}	0.001 ~0.022	0.0004 ~0.0051	1×10^{10} ~2.4×10^{11}	0.2 ~5.8
Noise 2 %	(< 1×10^{13})	(4×10^{12})	(0.024)	(0.0044)	(6×10^{10})	(4)
	5×10^{12} ~2.6×10^{15}	9×10^{11} ~3×10^{13}	0.001 ~0.038	0.0003 ~0.014	9×10^{9} ~7.5×10^{11}	0.2 ~5.4
Noise 3 %	(9×10^{13})	(6×10^{12})	(0.023)	(0.0041)	(6×10^{9})	(5)
	3×10^{12} ~7.2×10^{15}	3×10^{11} ~3×10^{13}	0.0003 ~0.081	0.0001 ~0.034	3×10^{9} ~2.0×10^{12}	0.1 ~5.3

Data in brackets are the real errors). Reprinted with permission from Ref. [92] © 2006, American Institute of Physics

Table 2.21 Input materials and device parameters of the R_d–V fitting procedure for the fabricated devices A, B, and C

Sample	X	N_a (cm^{-3})	μ_p (cm^2/V s)	A (μm^2)	T (K)
A	0.233	7.69×10^{15}	1290	784	77.4
B	0.2323	9.03×10^{15}	622	784	77.3
C	0.224	8.92×10^{15}	828	784	77.0

Reprinted with permission from Ref. [92] © 2006, American Institute of Physics

To verify the applicability of the above developed fitting procedure, the R–V curves of three long wavelength devices A, B, and C with different Cd composition have been studied. The material and device parameters, which are not used as fitting parameters, are summarized in Table 2.21. Their experimental measurement process is the same as that described in Ref. [95, 96]. The fitting voltage range is −0.48 to 0.12 V. Figure 2.74 shows the fitting results. The fitting parameters and their error ranges are listed in Table 2.22.

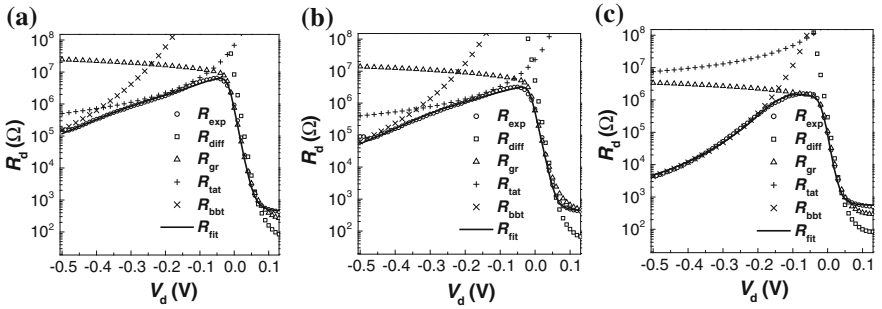

Fig. 2.74 Measured R–V curves of three real devices and their fitting results for Samples A (**a**), B (**b**), and C (**c**). Reprinted with permission from Ref. [92] © 2006, American Institute of Physics

Table 2.22 Six fitting parameters of N_d, μ_n/τ_n, τ_0, E_t/E_g, N_t, and R_s and their error ranges extracted from the measured R–V curves of the real devices A, B, and C

Sample	N_d (cm^{-3})	μ_n/τ_n (cm^2/V s^2)	τ_0 (ns)	E_t/E_g	N_t (cm^{-3})	R_s (Ω)
A	1.79×10^{16}	4.258×10^{13}	0.0796	0.4524	3.68×10^{12}	395.5
	(2×10^{13} ~ 3×10^{14})	(3×10^{12} ~ 6×10^{13})	(0.001 ~ 0.02)	(0.0007 ~ 0.006)	(4×10^{10} ~ 3×10^{11})	(1 ~ 14.8)
B	1.701×10^{16}	1.238×10^{14}	0.1248	0.5008	2.31×10^{12}	388.2
	(5×10^{12} ~ 4.5×10^{14})	(2×10^{12} ~ 1.2×10^{14})	(0.0007 ~ 0.04)	(0.0003 ~ 0.005)	(1×10^{10} ~ 2.3×10^{11})	(0.4 ~ 18.1)
C	2.109×10^{16}	1.024×10^{15}	0.0325	0.4601	8.49×10^{10}	498.7
	(3×10^{12} ~ 9×10^{14})	(2×10^{14} ~ 1.3×10^{15})	(0.003 ~ 0.005)	(0.005 ~ 0.006)	(5×10^{9} ~ 1.9×10^{11})	(2.1 ~ 41.6)

Data in brackets are the error ranges. Reprinted with permission from Ref. [92] © 2006, American Institute of Physics

In Table 2.22, compared to the value of the corresponding parameter, the lower limits of the error ranges are very small for all the samples. The maximum lower limit in Sample A is less than 10 % of the value of the corresponding parameter (μ_n/τ_n); and that of Sample B < 2 % (for N_t); and that of Sample C < 20 % (for μ_n/τ_n). These data indicate that the discreteness among the results from the ten fits in different fitting paths is very small. The upper limit of the error ranges is less than 40 % of the value of the corresponding parameter, except for the parameter N_t (in Sample C) and μ_n/τ_n (in all three samples). The upper error limits of μ_n/τ_n in all the three samples are almost equal to the value of μ_n/τ_n itself because the diffusion current mechanism, which is strongly correlated with μ_n/τ_n, fails to become dominant under forward biases. As shown in Fig. 2.74, when I_{diff} has only a small amount larger contribution to the dark current than I_{gr} after $V_d > 0.05$ V, the effect of series resistance increases and enlarges the estimation error (the upper limits of the error ranges). Likewise, the upper limits of the error ranges of N_t for Sample C is twice as much as the value of N_t, since the trap-assisted tunneling current mechanism, which is correlated with the parameter N_t, fails to become dominant under any biases. Nevertheless, one can see in Fig. 2.74 that the calculated *R–V* curves accurately fit the measured curves for all the three samples. Moreover, our fitting method can also correctly fit the specific case like Sample C, for which both the diffusion current mechanism and the trap-assisted tunneling current mechanism fail to be the dominant dark current at any bias in measured *R–V* curve. For Sample C, the parameters' multi-valued phenomena in the ten fits with different fitting paths do not exist. However, the upper limits of the error ranges are magnified. This only effects correctly estimating the accuracy of the fitting parameters. Therefore, we conclude that the fitting method developed in this work has highly fault-tolerant capability and could be expected to be an effective tool to analyze the *R–V* curves of long wavelength HgCdTe *n*-on-*p* photodiodes.

2.3.1.2 Temperature Dependence for Long Wavelength HgCdTe Photodiodes

The working temperature of a HgCdTe detector is generally around 80 K, this is mainly in order to allow the system to work in the scope of background limitations, so that the signal from background radiation is greater than the thermal noise. Background radiation signals are associated with the quantum efficiency and carrier lifetime, the thermal noise is associated with the working temperature and doping concentration of the base area. Therefore, determining the detector's carrier lifetime, carrier concentration and the working temperature limit becomes very important [97]. In addition, the nonuniformity of the temperature from the detector array can also produce different performance between different samples. These problems can be analyzed through research of the temperature dependence of the device's dark current. Analysis of the dark current characteristics under different operating temperatures is rather useful for determining the dark current mechanism. Many researchers on the analysis of HgCdTe devices have used the temperature

dependence of dark current [98–101] to obtain detailed operational information. In this chapter, we measured the variable temperature data of the dark current of HgCdTe detectors, and then used the fitting procedure that was introduced in the previous chapter to analyze the data [101].

The experiment set up 31 measurement points between 30 K and 300 K. We measured the *I–V* curve of the HgCdTe long wave detectors for each temperature in order to obtain the temperature dependence characteristics. Additionally, the experiment tests four samples on the same chip in order to ensure the repeatability of experimental results. The first step for the initial value in the analysis method is to find the initial carrier concentration of the *n* region under a large reverse bias. The carrier concentration of the *n* region is associated with a direct tunneling. Therefore, we want to measure the *I–V* curve in the bias region where the direct tunneling mechanism dominated the dark current, so that the reverse bias voltage should be appropriately large. Here, the range of measurement bias is −0.8 to 0.3 V, the bias interval is 5 mV. Sample C1, C2, C3, and C4 are tested from one chip C. The parameters of the chip C are shown in Table 2.21.

Figure 2.75a shows the temperature dependence of the R_0A product of n^+-on-p LW HgCdTe photodiodes for the four selected samples from 30 to 300 k. R_0A products of the four samples in the same chip show very good repeatability indicating the stability of the process. Figure 2.75b gives the property of the *R–V* curves for the sample C1 from 40 to 150 k. As the Fig. 2.75b shown: (1) the dynamic resistance decreases monotonously with the increasing of the temperature at the near zero-bias region; (2) the peak value of the dynamic resistance moves to the reverse bias region with increasing temperature. The peak value decreased with increasing temperature when the temperature is lower than 70 K. As the temperature is increased from 70 to 110 K, the peak value increased with increasing temperature. For temperatures above 110 K, the value again decreased with increasing temperature; (3) in the reverse bias region, the dynamic resistance increased with increasing temperature until 120 K, and then decreased.

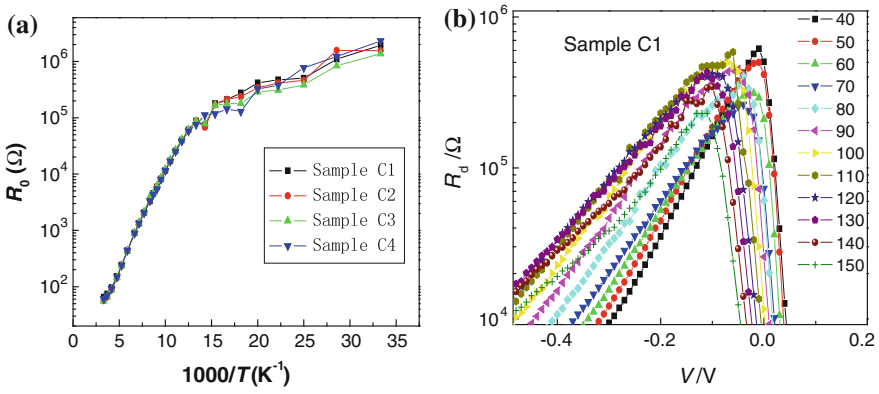

Fig. 2.75 **a** Temperature dependence of the R_0A for the four selected samples in the same chip. **b** Diode dynamic resistance versus bias for the sample C1 at different temperatures. Reprinted with permission from Ref. [101] © 2009, American Institute of Physics

To explain the experimental phenomena, we analyzed the experimental results with the fitting procedure. Figure 2.76 gives the fitting results of the *R–V* curves at some typical temperatures. As the fitting results show: (1) under a small forward

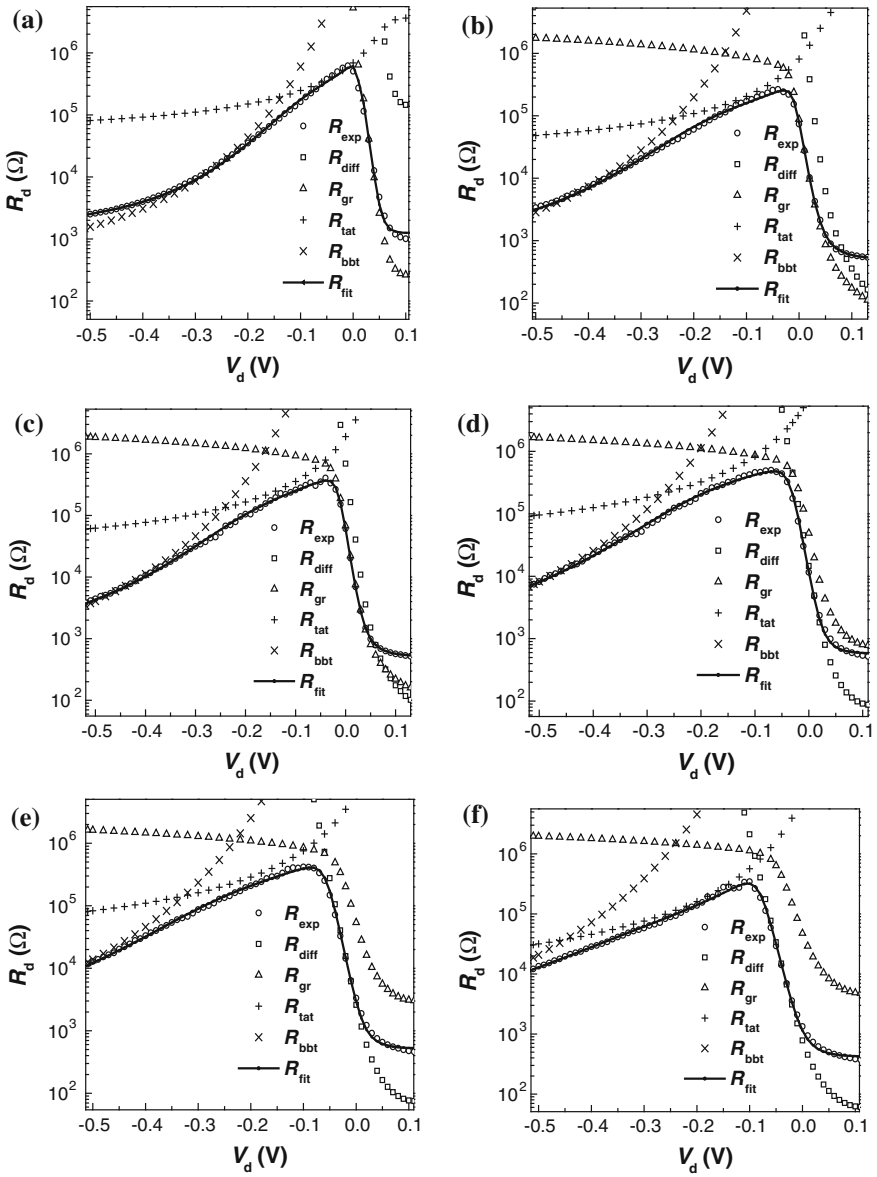

Fig. 2.76 Measured *R–V* curves and their fitted current components for the sample C1 at the temperatures of 40 K (**a**), 70 K (**b**), 80 K (**c**), 100 K (**d**), 120 K (**e**), and 140 K (**f**). Reprinted with permission from Ref. [101] © 2009, American Institute of Physics

bias, diffusion current is the dominant mechanism and the region dominated by diffusion will expand as temperature increases. For the forward bias region, I_{gr} dominates the dark current at low temperatures, while I_{diff} dominates the dark current in high temperatures. Both I_{diff} and I_{gr}, which linearly increase with the increasing temperature, are the thermal current components. This result explains the first phenomenon observed in the experiment. (2) The peak value of the *R–V* curves is decided by the TAT mechanism in low temperatures. As the temperature is increased to 70 K, the I_{gr} begins to jointly dominate the peak value. For temperatures above 100 K, the I_{gr} completely becomes the dominant mechanism. However, as the temperature rises further, I_{diff} dominates the peak value to replace the I_{gr}. When the temperature is increased to 140 K, the TAT mechanism again dominates the peak value of the *R–V* curves. In this process, RTAT decreased, then increased, and then decreased with the increasing of the temperatures. The resistance of the thermal mechanism decreased and moved to the left, so the peak value of the *R–V* curve tends to move to the left with the increasing temperature, it corresponds to the second point of experimental phenomenon (3). In the reverse bias region, the resistance of the TAT mechanism increased with increasing temperatures at low temperature, and was unchanged when the temperature is larger than 100 K. As the temperature increases, the region which is dominated by the TAT mechanism is moved to the large reverse bias side. So with increasing temperature, the dynamic resistance increased, but then the resistance began to decline when the temperature was higher than 120 K.

In the process of fitting, we also obtained a set of fitting parameters corresponding to each temperature. Figure 2.77 gives the characteristic parameters as function of the temperature for the four samples. It is important to note that the concentration of holes in the sample is measured from the Hall effects measurements at liquid nitrogen temperature, and the frozen effect [102] of acceptors in p-type HgCdTe material must be taken into account in the low temperature. Thus, according to the research results from Scott [103], shallow acceptor ionization energy and hole concentration at the temperature of 77 k have a simple relationship:

$$E_A = E_0 - \alpha P_0^{1/3} \tag{2.62}$$

where E_0 = 17 meV, α = 3 × 10-8 eV·cm, and P_0 is the hole concentration in the temperature of 77 k.

Figure 2.77a shows the dopant density in the *n* region (N_d) as a function of the temperature. Note that N_d is not monotonously increased with increasing temperature, but decreased with increasing temperature less than 60 K and increased with increasing temperature at a temperature lager than 60 k. These phenomena can be explained as follows. The ion implantation damaged n-type donors are completely ionized. Figure 2.77b shows the electron lifetime in the *p* region (τ_n) as a function of the temperature. Because fitting procedures can only fit the ratio of electron mobility to lifetime (μ_n/τ_n), we must use an empirical formula to calculate the electron mobility μ_n, then obtain τ_n. Figure 2.77c shows the temperature

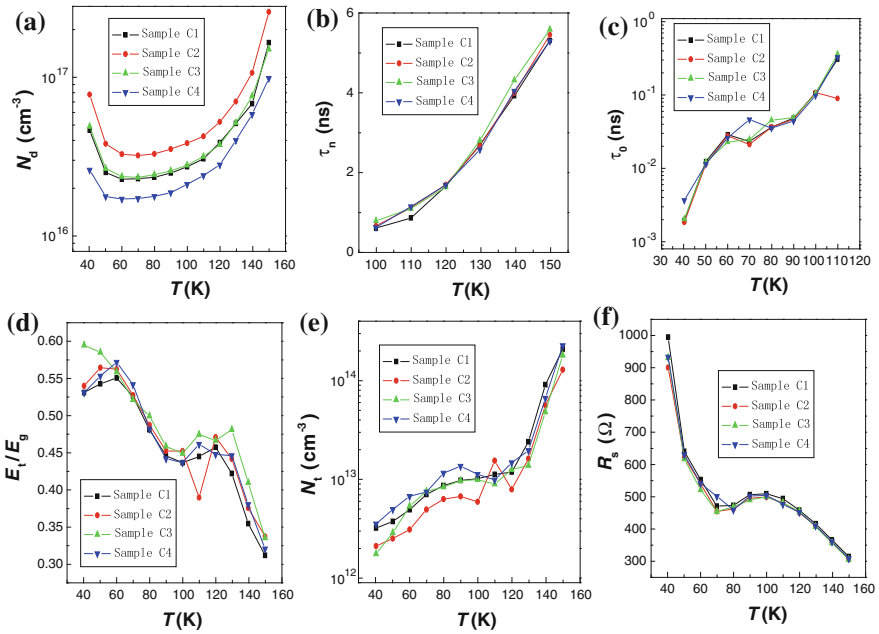

Fig. 2.77 Temperature dependence of the fitting parameters for the four samples. **a** the dopant density in the *n* region (N_d), **b** electron lifetime in the *n* region (τ_n), **c** effective lifetime in the depletion region (τ_o), **d** relative energy position of trap level (E_t/E_g) and (e) trap density (N_t) in the depletion region, and **f** series resistance (R_s). Reprinted with permission from Ref. [101] © 2009, American Institute of Physics

dependence of effective lifetime in the depletion region (τ_0). As the g-r current dominates the dark current for the forward bias at the low temperature, the fitting results of τ_n below 100 K, where the fitting error of τ_n is very large, are not shown in Fig. 2.77b. Similarly, the diffusion current dominates the dark current for forward bias at high temperature, magnifying the fitting error of τ_0. Therefore, the fitting results of τ_0 above 110 K are not shown in Fig. 2.77c. As the two figures show, minority carrier lifetime increased with increasing temperature, the qualitative temperature dependency of τ_n is in agreement with the reported in literatures [104–105].

Figure 2.77b shows the temperature dependence of τ_n. The value of τ_n is comparable to that reported in [106], about 3–150 ns. Note that the fitting value of the effective lifetime in the depletion region (in Fig. 2.77c) is smaller than that of normal one. We attribute parts of the deviation to the screening effect reduction and resonance scattering enhancement from deep level trap and charged trap in the depletion region in the high voltage field.

Figure 2.77d shows the relative energy position of the trap level (E_t/E_g) as function of temperature. From the figure, there are two stable stages: $0.45E_g$ for 90–130 K and $0.55E_g$ for temperature lower than 60 K. Therefore, we can consider that

HgCdTes have two stable characteristic trap levels. The trap level of $0.55E_g$ dominates the TAT mechanism when the temperature is lower than 60 k. When the temperature is increased to 60 K, the $0.45E_g$ begin to jointly dominate the TAT mechanism. For temperature above 90 K, the $0.45E_g$ completely becomes the dominant trap. Thus, we can also speculate that there is a trap level in $0.25E_g$ at high temperature. Figure 2.77e shows the temperature dependence of the trap density (E_t), trap concentration increased exponentially with the increasing of the temperature. Figure 2.77f shows the temperature dependence of the series resistance (R_s), the series resistance decreased with increasing temperature.

2.3.1.3 Statistical Analysis of Long Wave HgCdTe Photodiodes

At present, the processing of HgCdTe material and devices is much less mature than that of Si and GaAs due to the sensitive nature of HgCdTe material. Therefore, HgCdTe IRFPAs still suffer severely from temperature and photo related defects and nonuniformities in the performance of individual elements. In order to thoroughly understand the performance of HgCdTe material, a feasible method is to obtain the basic parameters of HgCdTe material from statistical analysis. However, the characteristics research of a single device can't meet the needs of such statistical requirement. For example: (1) the physical parameters obtained by the analysis of *I–V* characteristics from one unit cannot be applied to the whole chip; (2) the physical parameters obtained by the analysis of single chip cannot be applied to another chip even under the same process technology. An efficient approach is to study the *I–V* characteristics of many units between different chips under the same process technology. Then, the statistical results of basic physical parameters can be extracted by the proposed physical model. These statistical results of HgCdTe devices associated with the process condition have a great significance for the design and optimization for HgCdTe devices, especially for the next generation of focal plane devices such as HgCdTe two-color detectors.

In order to obtain the statistical parameters of a long wave HgCdTe device, the *R–V* curves of 392 HgCdTe diodes are analyzed and fitted. The Cd components of these devices are different from 0.223 to 0.238, which are tested at liquid nitrogen temperature (77.0–80.9 K). According to the fitting results, the diffuse current cannt be the dominant current all the time at liquid nitrogen temperature so that its contribution to the dark current can be ignored. Therefore, the fitting parameter μ_n/τ_n related to the diffuse current is unbelievable, and the size of μ_n/τ_n is not listed in this section.

The statistical range of each parameter obtained by fitting method is as follows: the dopant density in the n-type region is varied from 3×10^{15} to 3×10^{16} cm^{-3}; the effective lifetime (τ_0) of the depletion region is varied from 0.01 to 0.2 ns; the energy level (E_t) of the trap is varied from $0.4Eg$ to $0.6Eg$; the concentration of the trap (N_t) is varied from 1×10^{12} to 1×10^{13} cm^{-3}; the size of series resistance (R_s) is about 500 Ω. τ_0 is smaller than the lifetime of the neutral region due to the enhanced scattering from trap in high field. The other parameters are consistent with

the typical experiment results, which demonstrate the accuracy of the statistical method.

In order to obtain the distribution of parameters associated with the different process technologies, the performance parameters of HgCdTe devices manufactured by MBE and LPE process is studied for comparison. Figures 2.78, 2.79, 2.80, 2.81 and 2.82 show the distribution of the parameters from these two technologies (Black lines represent the MBE device, gray lines represent the LPE device, R_I is the responsivity of current, D^* is the detectivity, R_0 is the average value of the current responsivity, and D_0^* is the average value of detectivity). In the figure, the responsivity and detectivity of current are the experimental measurement data. The results show that the parameters obtained from MBE device are close to that of LPE device.

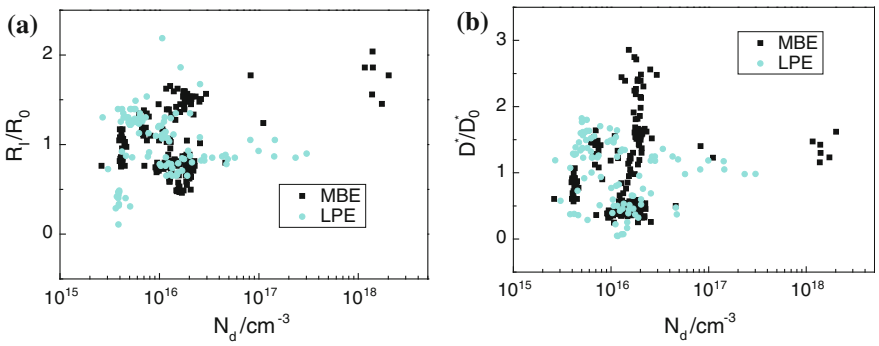

Fig. 2.78 **a** The statistical distribution of the responsivity with the dopant density in n-type region. **b** The statistical distribution of the detectivity with the dopant density in n-type region

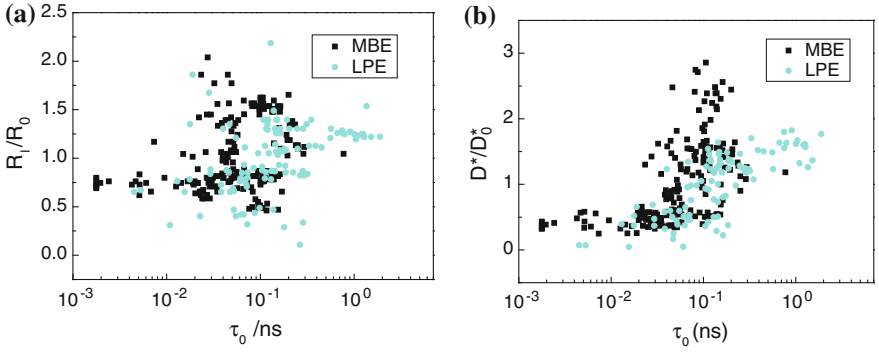

Fig. 2.79 **a** The statistical distribution of the responsivity with the effective lifetime of the depletion region. **b** The statistical distribution of the detectivity with the effective lifetime of the depletion region

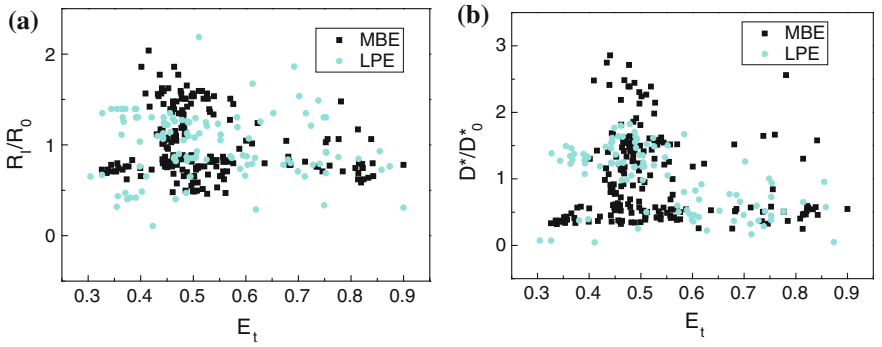

Fig. 2.80 a The statistical distribution of the responsivity with the relative energy level of the trap. **b** The statistical distribution of the detectivity with the relative energy level of the trap

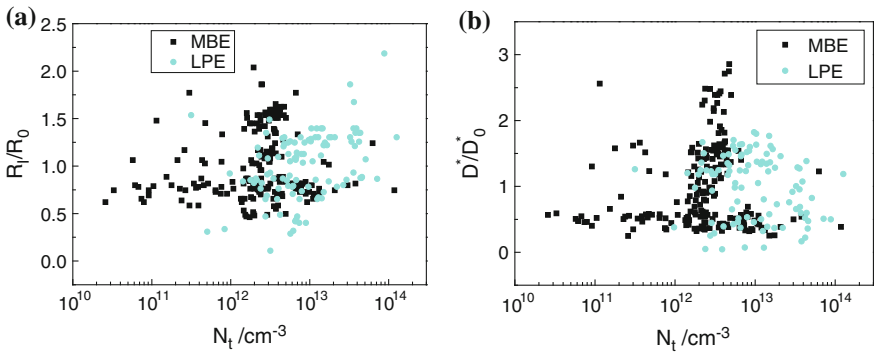

Fig. 2.81 **a** The statistical distribution of the responsivity with the concentration of the trap. **b** The statistical distribution of the detectivity with the concentration of the trap

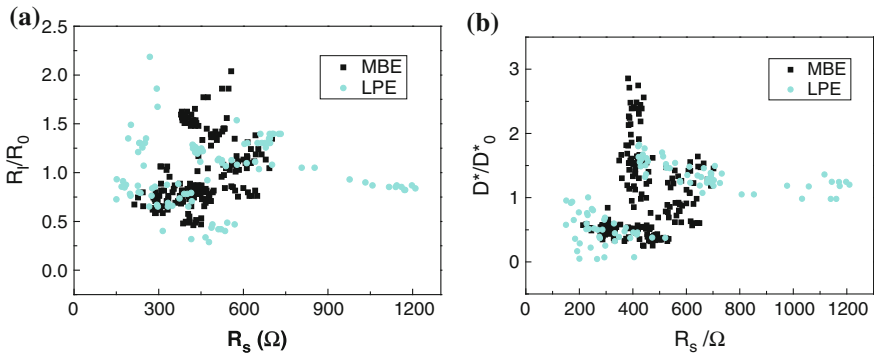

Fig. 2.82 **a** The statistical distribution of the responsivity with the series resistance. **b** The statistical distribution of the detectivity with the series resistance

2.3.1.4 Statistical Analysis of Mid-Wavelength HgCdTe Photodiodes

In order to obtain statistical parameters of medium wave HgCdTe device, the *R*–*V* curves of 206 HgCdTe diodes are analyzed and fitted. The Cd components of these devices are different from 0.2927 to 0.314, which are tested at liquid nitrogen temperature (77.0–78.3 K). The parameters of HgCdTe devices manufactured by MBE process are studied. According to the fitting results, the diffuse current cannot be the dominant current all the time at liquid nitrogen temperature so that its contribution to the dark current can be ignored. In addition, the direct tunneling cannot be the dominant current in a large reverse bias region all the time at liquid nitrogen temperature so that its contribution to the dark current also can be ignored. Therefore, the fitting parameter μ_n/τ_n and N_d related to the diffuse current and the direct tunneling current respectively are unreasonable, and the values of μ_n/τ_n and N_d are not listed in this section.

The statistical range of each parameter obtained by the by fitting method is as follows: the effective lifetime (τ_0) of the depletion region is varied from 0.01 to 1 ns; the energy level (E_t) of the trap is varied from 0.45*E*g to 0.7*E*g; the concentration of the trap (N_t) is varied from 1×10^{12} to 1×10^{15} cm^{-3}; the size of series resistance (R_s) is about 1000 Ω. The parallel resistance (*R*Sh) is varied from 108 to 109 Ω. τ_0 is smaller than the lifetime of the neutral region due to the enhanced scattering from trap in high field. The other parameters are consistent with the typical experiment results, which demonstrate the accuracy of the statistical method.

2.3.2 Extracting Device Parameters by Photoelectric Method

2.3.2.1 Photon-Generated Minority Carrier Lifetime

Minority carrier lifetime is one of the basic parameters of performance for semiconductor devices. For a conventional semiconductor, measuring the lifetime of minority carriers has become a routine technology. Even though HgCdTe has been studied extensively for infrared detectors, there is still a great deal of ambiguity in some issues, such as the minority carrier lifetime and its dominating recombination mechanisms. This is because of the instability of HgCdTe, in which the material property may be changed during the formation process of *pn* junction. Therefore, the parameter of the raw material can not be applied to estimate the properties of *pn* junction devices. Moreover, there are great differences between the actual parameters and the design parameters such as trap concentration, carrier concentration, the junction depth, the junction width in conventional techniques. These factors have a lot of unpredictable effects on the minority carrier lifetime in a *pn* junction device. In order to determine the minority carrier lifetime and the dominating recombination mechanisms of electron in a HgCdTe photodiode, measurements must be

carried out on the actual devices then the extracted parameters can be applied in devices design and simulate.

Many measurements have been developed to determine the minority carrier lifetime for other material devices such as: short-circuit current, open-circuit voltage decay (OCVD), pulse recovery technique, etc. However, the minority carrier lifetimes of HgCdTe material are in the nanosecond range, and these methods are not suitable to measure such short lifetime. In this chapter, we measure the minority carrier lifetime using an improved photo-induced OCVD measurement technique which compensates the effects of the junction equivalent capacitor and the trap center on the measurements. In order to minimize the effect of the junction equivalent capacitor and series resistance on the measurements, we used an Oriel QTH lamp as the steady-state bias light source. By recording the OCVD and fitting to the exponential decay curve, the minority carrier lifetime can be extracted.

The incident pulse laser having wavelength tuning range 2.3–10 μm was provided by a commercial optical parametric oscillator and a difference frequency generator which were pumped by a picosecond Nd: YAG laser. The structure of the machine is shown in Fig. 2.83. The laser delivered a pulse of 30 ps in duration at a frequency 10 Hz. Therefore, the influence of the laser pulse on the falling time was avoided.

As shown in Fig. 2.84, all HgCdTe samples were grown by MBE on GaAs substrates with CdTe buffer layers and an abrupt n^+-on-p structure were formed by

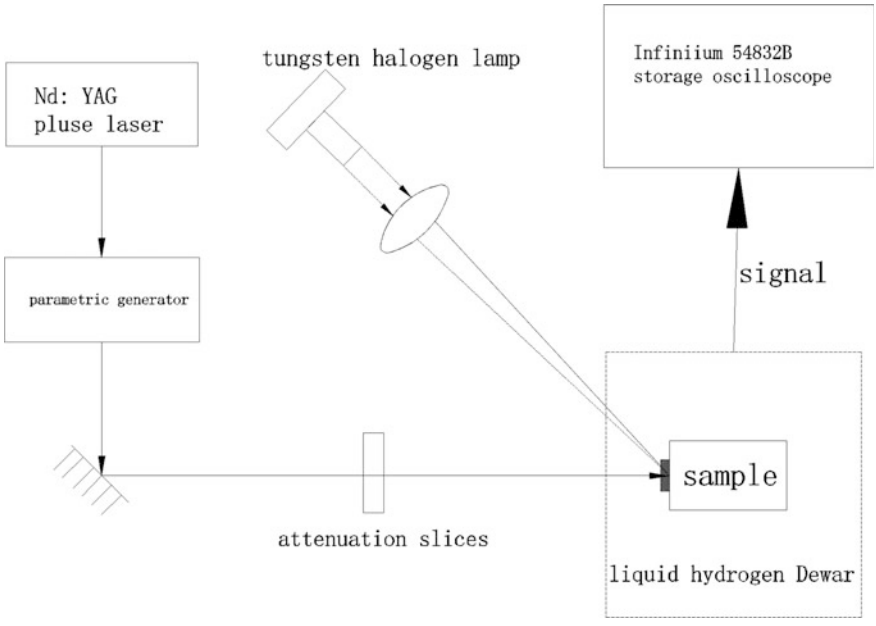

Fig. 2.83 The diagrammatic map of the experimental facility for measuring the lifetime of HgCdTe *p-n* junction use pulse laser open-circuit voltage decayed method

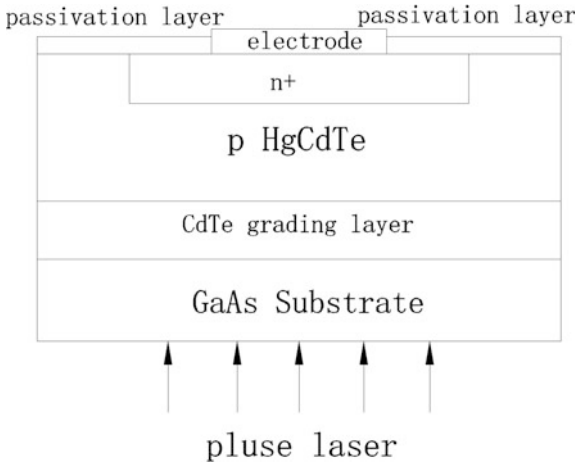

Fig. 2.84 Schematic of HgCdTe diode in the experiment

the ion implantation of B^+ in p-type $Hg_{1-x}Cd_xTe$. As ZnS films were formed on the $Hg_{1-x}Cd_xTe$ surface for passivation, the measured lifetime values were not influenced by the surface treatment. The detectors were processed into 50 × 50 μm^2 area mesa structures. The photogenerated voltage has been recorded by a storage oscilloscope.

In the experiments, according to the intensity of the injected carrier, the decay curve of photovoltage in the *p-n* junction can be divided into three different areas: strong injection, medium injection, and the low injection. If the bias light source is strong enough, the influence of n^+p junction and impurity deep energy level to the photovoltage decay behavior can be ignored. Then the lifetime can be determined by analyzing the result of the photovoltage decay curve. The lifetime of minority carriers in strong injection is given by: $\tau = \frac{2kT}{q}\left|\frac{1}{dV_{oc}/dt}\right|$. The concentration of excess minority carriers in p region is much higher than the equilibrium minority carrier but less than the equilibrium majority carrier at the condition of medium injection. The lifetime of minority carrier in medium injection is given by: $\tau = \frac{kT}{q}\left|\frac{1}{dV_{oc}/dt}\right|$. Here, k is the Boltzmann constant, T is the absolute temperature, q is the electron charge, t is the time. We can see, in strong and medium injection, the photovoltage (V_{oc}) linearly decays. The concentration of excess minority carriers in the p region is less than the equilibrium minority carrier in low rejection, and the curve of the photovoltage exponentially decays.

$$V_{oc} = \frac{kT}{q}\left[\exp\left(\frac{qV(0)}{kT}\right) - 1\right]\exp(-\frac{t}{\tau}) \tag{2.63}$$

where $V(0)$ is the open-circuit voltage when the light stops. In order to make the measured minority carriers reflect the actual working state of the device, we must take the non-equilibrium carriers in a state of low injection.

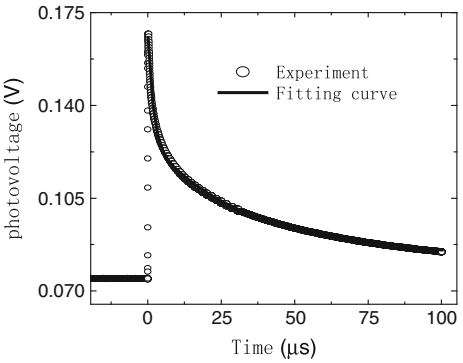

Fig. 2.85 Pulsed photo-response profiles from photodiode illuminated with laser pulses at zero bias light intensity. Reproduced from Ref. [109] with kind permission from Springer Science and Business Media

When the HgCdTe photodiode is excited by the pulsed laser, the photo-response shows a rapid increase and slow decay process. Depending on the intensity of the excitation source, the device is in a low injection condition. Figure 2.85 gives the pulsed photoresponse profiles from a photodiode illuminated with laser pulses at zero bias light intensity. The curve is an exponential decay to visual inspection. However, when the decay tail of the photoresponse was analyzed, we were not able to fit the measurement data with a suitable first-order exponential decay. Instead, a good fit is realized with a second-order exponential decay function with two different time constants: $V_{oc} = A\exp(-\frac{t}{\tau_1}) + B\exp(-\frac{t}{\tau_2})$. Here, $\tau_1 \sim 2$ μs and $\tau_2 \sim 35$ μs. Neglecting the detailed photo-generation and recombination mechanisms, we describe the decay curve profiles as dominated by the *RC* time constant and trap energy level effects on excess carrier's relaxation. Therefore, neither of the two time constants is the lifetime of minority carriers.

Figure 2.86 gives the OCVD curves at different intensities of bias light in the condition of the photodiode illuminated with a background. The steady-state photovoltage of the photodiode increases with the rising of the bias incident intensity. The decay time constants of photovoltaic response induced by the pulsed

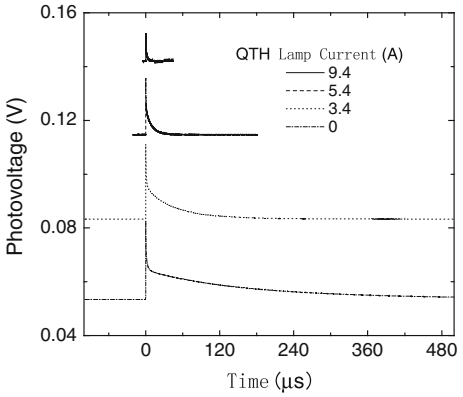

Fig. 2.86 OCVD curves at different intensity of bias light. Reproduced from Ref. [109] with kind permission from Springer Science and Business Media

laser are becoming shorter and shorter and the peak amplitude decreases with the increase of incident intensity, which is given in Fig. 2.86. This phenomenon can be attributed to the compensating of the junction equivalent capacitor and the trap center energy level effects under the bias light condition.

When the steady-state photovoltages do not increase with an increase in the background intensity, the photogenerated carriers recombination will dominate the decay time constant which is related to the minority carrier lifetime. Since the values of the resistance and the carrier lifetime are much larger in the p region than in the n^+ region. In addition, the photogenerated carriers in the emitter are about one percent of the carriers generated in the base; therefore, we can assume that the carriers stored in the base play a dominant role in the OCVD process. The compensated photoexcited OCVD decay curve is fitted with the exponential decay function, and the lifetime magnitude of the minority carrier in p region is determined to be 190 ns, which is shown in Fig. 2.87.

Using the method mentioned above, the minority carrier lifetime of the HgCdTe photodiode with different compositions can be obtained and is shown in Fig. 2.88. The results show that the carrier lifetimes are in the range of 18–407 ns at 77 K for the measured detectors of four compositions. With increasing composition, the minority carrier lifetimes have an increasing tendency, and the lifetime of the shortest wavelength infrared detectors are the longest compared to other detectors. The results of the same composition came from different units of one array. The basis of distinction between the different units within the same array is that the HgCdTe raw material is non-uniform or the growing process can not be mastered. The electron lifetimes extracted from the experiments are reasonable because of the lifetime magnitude consist with others results. Generally, there is a certain difficulty to measuring minority carrier lifetime precisely. Even for the silicon material, the accuracy scope of the minority carrier lifetime is ±135 % in different laboratory in American Society for Testing and Materials (ASTM). Therefore, it is acceptable that there is some difference in the lifetime experiment measuring of HgCdTe photodiode.

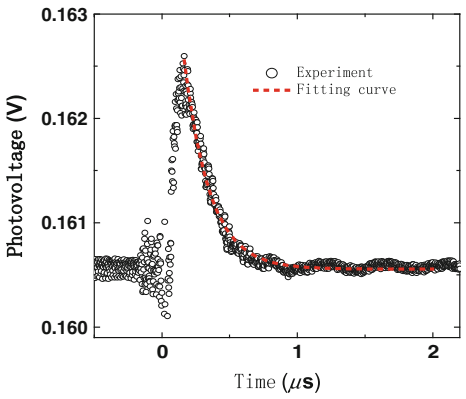

Fig. 2.87 Pulsed photo-response profiles from photodiode illuminated with laser pulses at suit bias light intensity. Reproduced from Ref. [109] with kind permission from Springer Science and Business Media

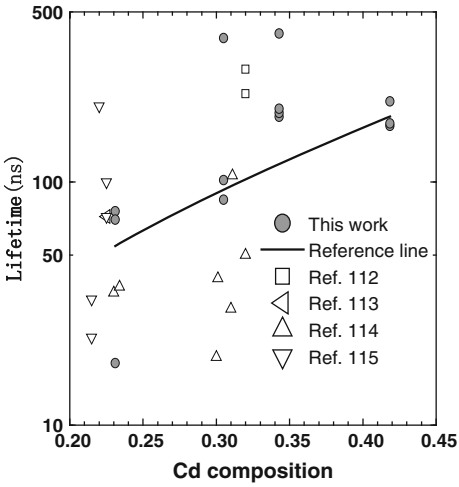

Fig. 2.88 Variation of the extra carrier lifetime with Cd composition [106–109], the line is for guiding. Reproduced from Ref. [109] with kind permission from Springer Science and Business Media

2.3.2.2 Laser Beam-Induced Current Microscopy for HgCdTe Photodiodes

Laser beam-induced current (LBIC) microscopy has proven useful for quick and non-destructive measurement of the junction performance of each pixel in large arrays at an early stage in the fabrication process. Therefore, significant cost savings and processing improvement would be expected in FPAs. Two-dimensional LBIC microscopy, also generally called photocurrent mapping (PC mapping), can provide spatially resolved information about local electrical properties and *p-n* junction formation in photovoltaic infrared photodetectors from which it is possible to extract material and device parameters such as junction area, junction depth, diffusion length, leakage current position and minority carrier diffusion length, etc. To date, LBIC as a nondestructive method has been widely used for infrared photodiode array characterization. The big challenge is to quantify the relationship between LBIC mapping and parameters that influence the electrical performance of devices. The main issue of this section is the application with respect to extracting material and device parameters [110].

(1) **LBIC setup**

In preparation for the LBIC experiment, only two shorted Ohmic contacts would be constructed at remote positions on either side of the device(s). The principle of *p-n* junction array LBIC testing is schematically represented in Fig. 2.89. He–Ne laser irradiance at a wavelength of 632.8 nm is focused onto the surface of the semiconductor, and stepped incrementally across the sample in the horizontal direction. When the laser spot is more than a few carrier diffusion lengths from a built-in electric field, the photogenerated electron–hole pairs recombine without reaching a junction region and therefore no current signal will be induced. In contrast, if the

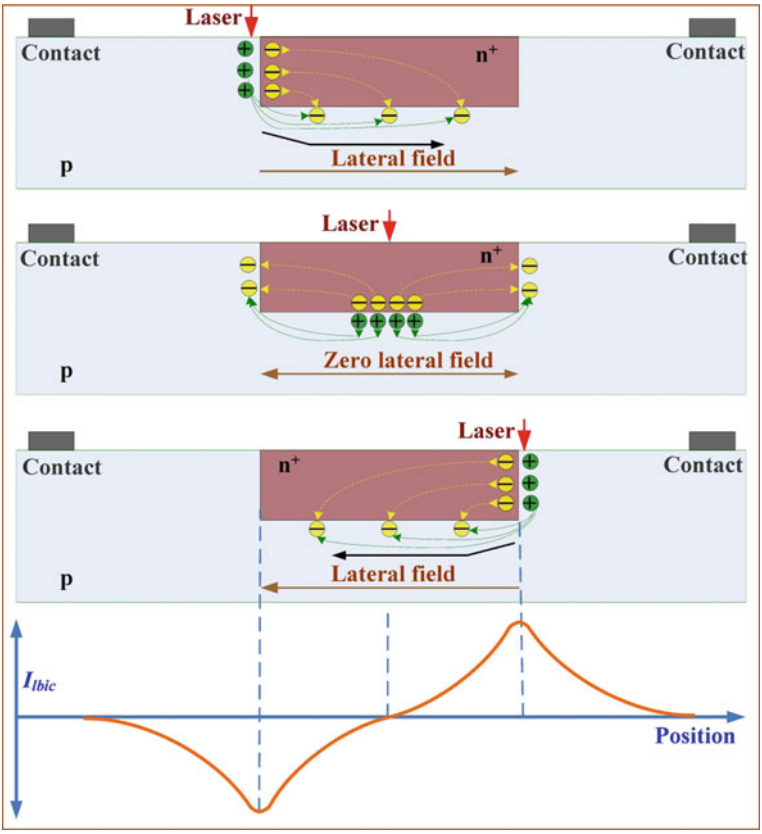

Fig. 2.89 The principle of a single n^+-on-p pixel LBIC testing. Reprinted with permission from Ref. [111] © 2014, American Institute of Physics

photogenerated electron–hole pairs can diffuse and be separated by the built-in electric field, the separated carriers seek to recombine via returning current paths, which could be both the internal and external closed circuits; resulting in an induced current that can be measured.

The LBIC profile presents a positive and negative bimodal distribution according to the three typical positions of a laser spot on the surface of the sample. This is explained by assuming the direction from right to left of device as being the direction of negative current flow.

Case 1: Illumination on the left of p-type region close to the junction

If the laser is focused onto the surface of the p-type region close to the junction, the photogenerated carriers that are separated by the built-in electric field would provide excess electrons (denoted by "-") into the n-type region while excess holes (denoted by "+") remain in the p-type region. Since the conductivity of the n-type

region is nearly two orders of magnitude more than that in the p-type region, the excess electrons can quickly redistribute themselves over the region uniformly. A reinjection of electrons can occur in the underlying p-type region. Finally, the presence of these excess holes and electrons constitutes a localized forward bias of the junction (direction from left to right), that drives the excess carriers to seek any possible returning current paths for recombination. Among these paths, the returning current via the external circuit contribute to the LBIC's negative signal.

Case 2: Illumination on the right of p-type region close to the junction

This situation is similar to the previous analysis; the photogenerated carriers diffuse and are separated by the built-in electric field, resulting in excess electrons passing into the n-type region while excess holes pass into the p-type region. However, a localized forward bias of the junction in the opposite direction (from right to left) is formed. Therefore, a positive LBIC signal can be obtained.

Case 3: Illumination on the surface of n-type region

A unique feature in the situation where the laser is focused onto the surface of the n-type region was the appearance of two types of returning current flows in the opposite direction. If the laser spot is exactly located in the middle of n-type region, two opposite return current flows will cancel each other, producing a zero net LBIC signal.

Two different structures of the laser beam induced current (LBIC) test system are shown in Fig. 2.90. The test system typically consists of a laser light source, CCD camera, computer, temperature controller, and an induced current measuring system with a lock-in amplifier. The sample is placed in a temperature controlled Dewar of liquid nitrogen. The He–Ne laser is focused to a spot of 1–1.5 μm in diameter which is stepped across the sample. The induced current is recorded by a SR830 DSP lock-in amplifier as a function of *x*-*y* scanning coordinates to provide a spatial LBIC map. The main difference between the two LBIC test systems is the method used to scan the samples. In Fig. 2.90a, the sample is scanned on a two-dimensional computer controlled mobile platform. Another method is the use of a two-dimensional scanning galvo system to precisely control the direction of the laser beam by the computer, as shown in Fig. 2.90b.

(2) **Junction depth and length extraction**

The temperature dependence of the peak-to-peak LBIC measurements on a *p*-*n* junction was first examined by Redfern et al. [112], indicating that a saturation state can be reached under low temperatures. Under the saturation conditions, the junction resistance may be enough to dominate the resistance of each of the possible current paths. Therefore, the peak-to-peak magnitude of LBIC is independent of the bulk material properties. Other parameters, including the junction geometry, can be examined by the LBIC peak-to-peak magnitude, greatly reducing the complexity of the analysis. Simulated LBIC peak-to-peak magnitudes as a function of temperature in HgCdTe photodiodes with different components are shown in Fig. 2.91 [113].

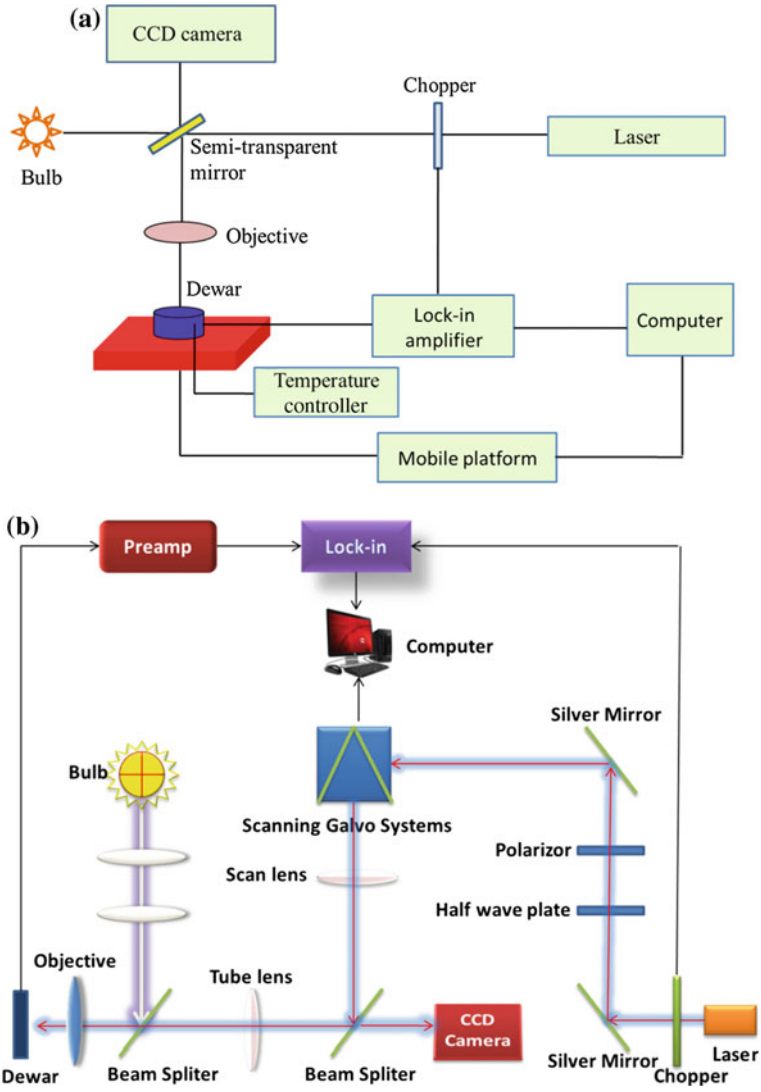

Fig. 2.90 Two different structure frames of laser beam induced current (LBIC) test system. **a** Scanning is performed by changing position of sample under control of a two-dimensional mobile platform. **b** Scanning is performed by changing the direction of the laser beam under control of a scanning galvo system

The condition of threshold temperature for $Hg_{0.69}Cd_{0.31}Te$ is below 200 K. The effects of junction depth and length on LBIC profiles in $Hg_{0.69}Cd_{0.31}Te$ photodiodes at 170 K below the threshold temperature are shown in Fig. 2.92. It has been found that there is a linear relationship between the magnitude of the LBIC peak and the value of the junction depth and length. For photodiodes with greater depth,

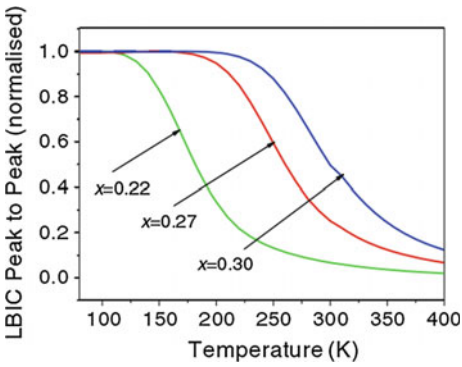

Fig. 2.91 Simulated LBIC peak-to-peak magnitudes as a function of temperature in $Hg_{1-x}Cd_xTe$ photodiodes. Reprinted from Ref. [113], with kind permission from Springer Science+Business Media

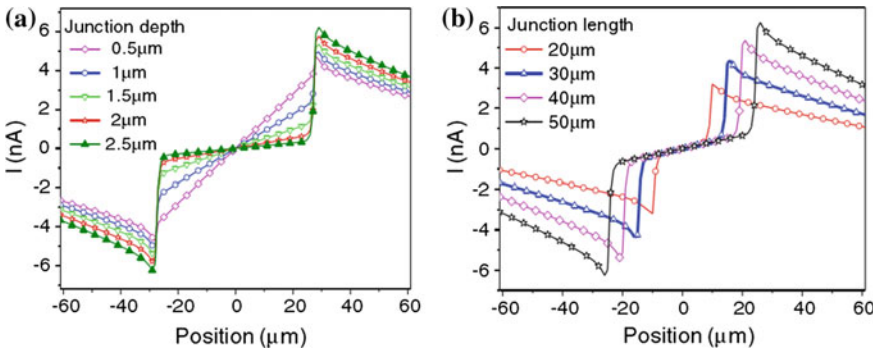

Fig. 2.92 **a** LBIC profiles with different depths of $Hg_{0.69}Cd_{0.31}Te$ p-n junction and **b** LBIC profiles with different lengths of $Hg_{0.69}Cd_{0.31}Te$ *p-n* junction. Reprinted from Ref. [113], with kind permission from Springer Science+Business Media

more photogenerated electrons in the p-type region can be swept across the junction, which results in a stronger LBIC signal. On the other hand, loop circuit resistance is reduced by shortening of the distance between the contact and junction in the photodiodes with longer length. Therefore, the LBIC current also becomes larger when the junction length becomes larger [113].

(3) **Minority carrier diffusion length extraction**

The minority carrier diffusion length is a key indicator of material quality and device performance. The dependence of laser beam induced current (LBIC) on minority carrier diffusion length of n-on-p HgCdTe photodiode has been investigated earlier [114, 115]. In the standard diffusion length (L_p) test method, the procedure may bring about damage to the *p-n* junction. The test structure is also

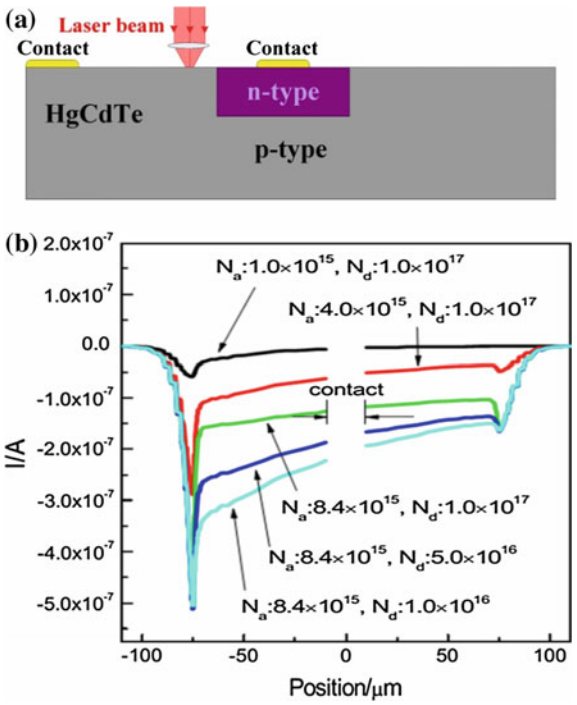

Fig. 2.93 **a** The standard diffusion length (L_p) test structure **b** the standard diffusion length (L_p) test in HgCdTe photodiodes with different doping concentrations. Reprinted with permission from Ref. [115] © 2009, Chinese Physical Society

difficult to fabricate because of the need for electrical contacts on the *p-n* junction unit as shown in Fig. 2.93a. In contrast, the LBIC test structure consists of only two Ohmic contacts at remote positions on either side of the device(s). The decay of the LBIC as the laser spot is scanned away from the edge of *p-n* junction is related to the diffusion length in p-type region. The characteristic diffusion length (L) can be obtained by fitting a simple exponential function to the LBIC curve. The exponential formula for the attenuation curve in p-type region is given by [116]:

$$|I_{\mathrm{LBIC}}(d)| = k \cdot \mathrm{e}^{-\frac{d}{L}} \tag{2.64}$$

where k is the proportional coefficient, d is the distance from the laser spot location to the boundary of *p-n* junction, and L is the characteristic diffusion length.

In two characteristic ways of diffusion length, the attenuation curves in p-type region are both related to the minority carrier diffusion length. When the laser spot is near the carrier diffusion length from a built-in electric field, the photogenerated electron–hole pairs can diffuse and be separated by the built-in field. The only difference is that the separated carriers recombine via return current paths, i.e., the internal and external closed circuits (two electrodes are both in *p* region). A LBIC signal can be measured in an external closed circuit of LBIC in this phenomenon. However, the separated carriers are directly collected by the electrodes in *p* region and n region of the standard protocol. Therefore, there may be a negligible

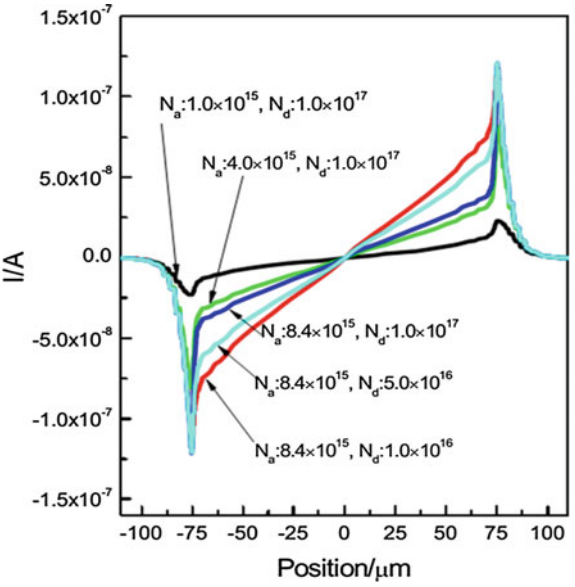

Fig. 2.94 The LBIC test for characteristic diffusion length (L) in HgCdTe photodiodes with different doping concentrations. Reprinted with permission from Ref. [115] © 2009, Chinese Physical Society

difference between the size of L and L_p. One can extract the ratio of L/L_p from the experimental results using two different methods.

The standard diffusion length (L_p) and the characteristic diffusion length (L) tested by LBIC in HgCdTe photodiodes with different doping concentrations are shown in Fig. 2.93 and Fig. 2.94, respectively [115].

The diffusion lengths extracted by both these methods are listed in Table 2.23 [115]. It is found that the L/L_p ratio is close to 1 and is independent of the doping concentration distribution. At the same time, the ratio of L/L_p remains the same, irrespective of the size of SRH carrier lifetime and mobility. Therefore, the characteristic diffusion length by LBIC can be considered equivalent with the standard diffusion length.

Table 2.23 Extracted L/L_p under different N_a and N_b

$N_a/10^{15}$ cm^{-3}	$N_d/10^{17}$ cm^{-3}	Characteristic diffusion length L (μm)	Standard diffusion length L_p (μm)	L/L_p
1.0	1.0	8.34	7.81	1.07
4.0	1.0	6.09	5.73	1.06
8.4	1.0	5.34	4.97	1.07
8.4	5.0	5.41	5.02	1.08
8.4	1.0	5.40	5.06	1.07

Reprinted with permission from Ref. [115] © 2009, Chinese Physical Society

(4) Localized junction leakage characterization

The effect of localized defects is one of the main limitations in the performance of HgCdTe infrared focal plane arrays. Such defects, including voids; line dislocations; and triangles, may influence the overall integrity of the *p-n* junction and significantly degrade the performance of the photodiodes due to the localized junction leakage. LBIC, as an efficient and nondestructive tool, is used for the localized junction leakage characterization in the photodiodes. Redfern et al. [117, 118] studied the LBIC profiles when a small localized leakage region was introduced at various positions along the horizontal portion of the junction. The leakage current was simulated by including a small piece of metal that was Ohmic to both sides of the junction [119]. The model structure of the *p-n* junction with localized junction leakage path is shown in Fig. 2.95.

It was shown that when the leakage point is asymmetric inside the device, an asymmetry in the LBIC line profile induced by the small metallic region can be obtained by this leakage model. However, the assumption of bringing in metal with large conductance in the HgCdTe photodiodes is not very practical.

On the basis of this data, an improved leakage model including a small HgCdTe region with extremely short carrier lifetime instead of the metallic region is proposed [120]. Many factors, such as trap-assisted tunneling, generation–recombination (g-r) and diffusion current, can influence the junction leakage current. Dark current dominant mechanisms change with the operating temperature. The temperature dependence of the LBIC profiles is shown in Fig. 2.96.

The asymmetric LBIC profile can indicate that there is localized leakage somewhere inside the sample structure. The localized defects reduce the resistance of the return current path crossing the junction via localized leakage, and most current flows through the leakage current path and fails to contribute to the external circuit current. In addition, the temperature dependence of symmetry in the LBIC profile reflects the change in the dominating mechanism of dark current from a certain degree.

It can be observed that the LBIC profiles have different distributions for different temperatures. Below 170 K, the diffusion and generation–recombination dark currents are very small. However, with increasing the temperature, the deep level traps are activated that lead to a lower SRH lifetime. The LBIC profile tends to be more asymmetric with increasing temperature. When temperature is above 170 K, the diffusion current component becomes dominant. Then, the leakage current is relatively reduced with the diffusion current being dominant at higher temperatures.

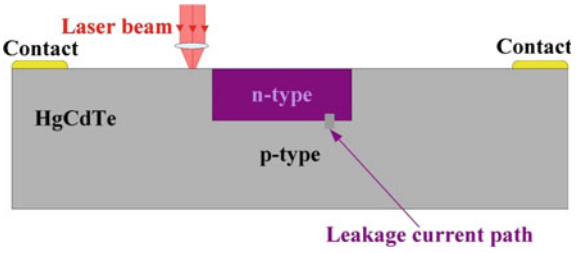

Fig. 2.95 The model structure of the *p-n* junction with localized junction leakage path along the horizontal portion of the junction

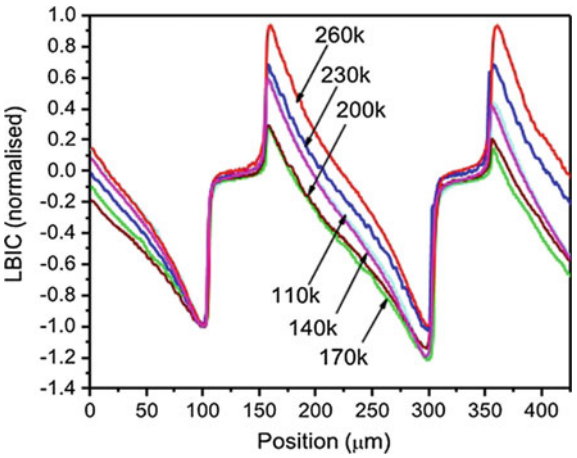

Fig. 2.96 The LBIC measurements are taken at a range of temperatures from 110 to 260 K. Reprinted with permission from Ref. [120] © 2013, American Institute of Physics

The LBIC profile becomes more symmetric with increasing temperature above 170 K. However, when the localized leakage point is situated at the center in the device, it is very difficult to confirm whether there is leakage in the diode because the distribution of LBIC profile is symmetrical. Therefore, in most situations, the asymmetric LBIC profile may indicate that there is localized leakage somewhere inside the sample structure.

(5) **Electrically active defects-related junction transformation**

Recent study [111, 121–125] shows that the phenomenon of extended defects induced by semiconductor manufacturing process always exists in HgCdTe infrared arrays, such as in B^+ ion implantation and pulsed laser drilling for the formation of a *p-n* junction. Those defects may be sensitive to temperature and laser excitation intensity and play a very significant role in the junction transformation. Hu et al. [121, 126] first observed that B ion implantation damage-induced defects can potentially produce a deformation of the LBIC in As-doped long wavelength HgCdTe infrared detector pixel arrays. This discovery unveiled an application of LBIC for the corresponding implant-induced defects analysis and characterization. Correlated theoretical models for trap-related *p-n* junction transformation have been proposed to analyze the deformation of LBIC curve induced by the extended defects.

The model structure of the *p-n* junction transformation in As-doped long wavelength $Hg_{1-x}Cd_xTe$ ($x \approx 0.224$) infrared arrays under different temperatures is shown in Fig. 2.97, When the temperature is relatively high, the deep levels (acceptor-type) induced by the ion implantation damage are fully activated and can trap significant numbers of free electrons, which are temperature sensitive. It makes the B^+ ion implantation region become n^--type or p-type as shown in Fig. 2.97b, c. Furthermore, the laser beam intensity is another key factor that determines the reversion. The photo-generated carriers are comparable to the temperature induced intrinsic carriers, and create an n^+-type to n^--type reversion [121]. At cryogenic

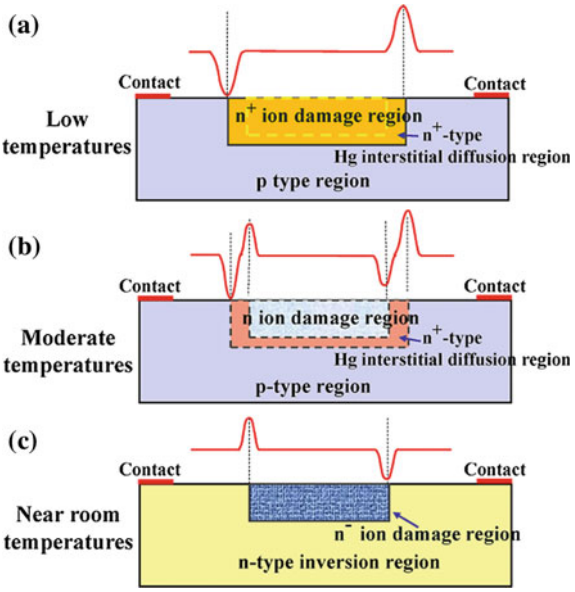

Fig. 2.97 Proposed *p-n* junction transformation models **a** at low temperature where the typical n^+-*on-p* junction is formed, **b** at moderate temperature where the *n*-n^+-*on-p* junction is formed, and **c** at near room temperature where the n^--on-*n* junction are formed. Reprinted with permission from Ref. [126] © 2012, American Institute of Physics

temperatures the implantation damage-induced traps in the n^+ region are almost inactivated, therefore, a typical n^+-on-p junction is formed.

In addition, the mixed conduction effect for p-type narrow band gap HgCdTe materials must be taken into account. This effect is mainly caused by the higher electron mobility compared with that of holes and the temperature increase generated large number of intrinsic carriers. Therefore, the narrower the forbidden bandgap, the more obvious is the mixed conduction effect. The mixed conduction, together with As-doping amphoteric behavior, makes the p-type absorption layer transform to an n-type layer at near room temperature. At moderate temperature, the coupling *n*-n^+-on-p junction is formed.

Ion implantation traps, As-doping amphoteric behavior, and the mixed conduction effect, are the main reasons for inducing the polarity reversion coupling of LBIC at different temperatures. Figure 2.98 shows the experimental results of the polarity inversion and coupling of the LBIC in As-doped long wavelength HgCdTe infrared detector pixel arrays.

In summary, accompanied by the technological development and extensive applications of infrared focal plane arrays, position-dependent LBIC or PC mapping has triggered a wave of research interest for device characterization in the early stages of the fabrication process. LBIC or PC mapping technologies rely on a scanning laser system that is close to the diffraction limit, making them highly sensitive to spatially resolved electric fields and localized nonuniformities in infrared materials. The spatially resolved information about electrical properties makes the extraction of performance parameters in infrared materials easier and more efficient through the establishment of accurate simulation models. The high

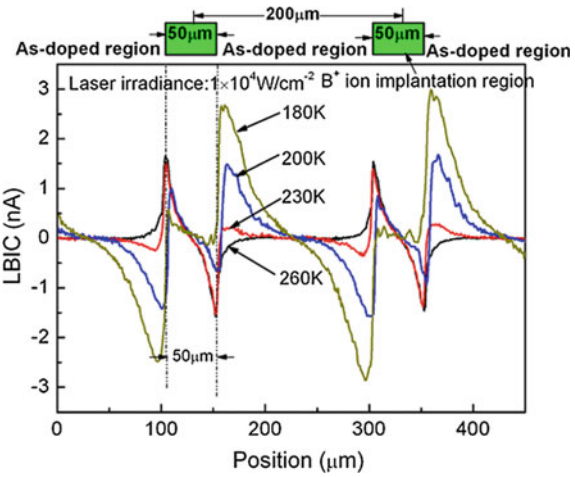

Fig. 2.98 Experimental results of temperature-dependent LBIC signal profiles with a laser power density of 1×10^4 W/cm^2. Reprinted with permission from Ref. [126] © 2012, American Institute of Physics

flexibility, low operational costs, and excellent spatial resolution properties of LBIC enable this method to be a highly useful tool for the characterization and optimization of future photovoltaic studies.

2.4 Summary

During the rapid development of HgCdTe infrared detector technology, many new models and methods have been proposed and developed. In this chapter, those models and methods, which are associated with the process of materials and devices, have been introduced. First, to improve the accuracy of device modeling, the influences of non-parabolic conduction bands and carrier degeneracy on dark currents are studied systematically. The analysis method of the HgCdTe dark current is established. At the same time, statistical results of characteristic parameters are extracted. Second, a feasible numerical method is achieved to optimize the thickness of the absorption layer and reduce the influence of the interface charge on device performance. In addition, the optimized structure of HgCdTe infrared detectors with low cross talk is proposed. Thirdly, the dependences of material and device parameters on actual HgCdTe devices are discussed comprehensively. Simulation methods for the structure characteristics, temperature effects, and cross talk of HgCdTe two-color detection are proposed. Finally, the lifetime of minority carriers in actual HgCdTe photodetector is extracted. The LBIC analytical method, which is accepted as a nondestructive tool and has been widely used for infrared photodiode array characterization, is introduced in detail. The application of LBIC with respect to extracting material and device parameters is systematically summarized.

References

1. Schmit JL. Intrinsic carrier concentration of $Hg_{1-x}Cd_xTe$ as a function of x and T using k.p calculations. J Appl Phys. 1970;41:2876–9.
2. Leonard WF, Michael ME. Carrier concentration of $Hg_{1-x}Cd_xTe$. J Appl Phys. 1974;45:958–60.
3. Hansen GL, Schmit JL. Calculation of intrinsic carrier concentration in $Hg_{1-x}Cd_xTe$. J Appl Phys. 1983;54:1639–40.
4. Lowney JR, Seiler DG, Littler CL, et al. Intrinsic carrier concentration of narrow-gap mercury cadmium telluride based on the nonlinear temperature dependence of the band gap. J Appl Phys. 1992;71:1253–8.
5. Nemirovsky Y, Finkman E. Intrinsic carrier concentration of $Hg_{1-x}Cd_xTe$. J Appl Phys. 1979;50:8107–11.
6. Chu J. The physics of narrow band gap semiconductors. 1th ed. Beijing: Science press; 2005. p. 283.
7. Madarasz FL, Szmulowicz F. Intrinsic carrier concentration in $Hg_{1-x}Cd_xTe$ with the use of Fermi-Dirac statistics. J Appl Phys. 1985;58:2770–2.
8. Kosai K. Status and application of HgCdTe device modeling. J Electron Mater. 1995;24:635–40.
9. Williams GM, De Wames RE. Numerical simulation of HgCdTe detector characteristics. J Electron Mater. 1995;24:1239–48.
10. Wenus J, Rutkowski J, Rogalski A. Two-dimensional analysis of double-layer heterojunction HgCdTe photodiodes. IEEE Trans Electron Devices. 2001;48:1326.
11. Hess GT, Thomas JS. HgCdTe double layer heterojunction detector device. SPIE. 2000;4028:353–63.
12. Gopal V, Singh SK, Mehra RM. Excess dark currents in HgCdTe p^+-n junction diodes. Semicond Sci Technol. 2001;16:372–6.
13. Velicu S, Ashokan R, Sivananthan S. A model for dark current and multiplication in HgCdTe avalanche photodiodes. J Electron Mater. 2000;29:823–7.
14. Quan ZJ, Chen GB, Sun LZ, Ye ZH, Li ZF, Lu W. Effects of carrier degeneracy and conduction band non-parabolicity on the simulation of HgCdTe photovoltaic devices. Infrared Phys Technol. 2006;50:1–8.
15. Liu E, Zhu B, Luo J. The physics of semiconductors. 6th ed. Beijing: Publishing House of Electronics Industry; 2003. p. 71.
16. Bhan RK, Dhar V. Carrier density approximation for non-parabolic and highly degenerate HgCdTe semiconductors. Semicond Sci Technol. 2004;19:413–6.
17. Bhan RK, Dhar V. Improved model for surface shunt resistance due to passivant for HgCdTe photoconductive detectors. Semicond Sci Technol. 2003;18:1043–54.
18. Wang J, Chen XS, Wang ZQ, Hu WD, Lu W, Xu FQ. The mechanism of the photoresponse blueshift for the n-type conversion region of n^+-on-p $Hg_{0.722}Cd_{0.278}Te$ infrared photodiode. J Appl Phys. 2010;107:044513.
19. Gopal V, Gupta S, Bhan RK, et al. Modeling of dark characteristics of mercury cadmium telluride n^+-p junctions. Infrared Phys. Technol. 2003;44:143–52.
20. Jo NH, Yoo SD, Ko BG, et al. Two-dimensional numerical simulation of HgCdTe infrared detectors. SPIE. 1998;3436:50–60.
21. Ye ZH, Hu XN, Zhang HY, Liao QJ, Li YJ, He L. Study of dark current for mercury cadmium telluride long-wavelength photodiode detector with different structures. J Infrared Millim Waves. 2004;23(2):86–90.
22. Hu WD, Chen XS, Yin F, Ye ZH, Lin C, Hu XN, Quan ZJ, Li ZF, Lu W. Simulation and design consideration of photoresponse for HgCdTe infrared photodiodes. Opt Quant Electron. 2009;40:1255–60.
23. Madarasz FL, Szmulowicz F. Equilibrium barrier formation in p-on-N and P-on-n graded HgCdTe heterojunctions. SPIE. 1989;1106:117–32.

24. Weiler MH, Reine MB. Effect of a valence-band barrier on the quantum efficiency and background-limited dynamic resistance of compositionally graded HgCdTe P-on-n heterojunction photodiodes. J Electron Mater. 1995;24:1329–39.
25. Wenus J, Rutkowski J. Influence of valence-band barriers in VLWIR HgCdTe P-on-n heterojunctions on photodiodes parameters. Phys Stat Sol (b). 2002;229:1093–6.
26. Vasilyev VV, Predein AV. Influence of graded p-P heterojunction's potential barrier on characteristics of three-dimensional HgCdTe photodiode. SPIE. 2005;5834:83–91.
27. Quan ZJ, Sun LZ, Ye ZH, Li ZF, Lu W. Optimization design of the band profiles of HgCdTe heterojunctions. Acta Physica Sinica. 2006;55:3611–6.
28. Migliorato P, White AM. Common anion heterojunctions: CdTe-CdHgTe. Solid-State Electron. 1983;26:65–9.
29. Bratt PR, Casselman TN. Potential barriers in HgCdTe heterojunctions. J Vac Sci Technol. 1985;A3:238–45.
30. Madarasz FL, Szmulowicz F. Barrier formation in graded $Hg_{1-x}Cd_xTe$ heterojunctions. J Appl Phys. 1987;62:3267–77.
31. Madarasz FL, Szmulowicz F. The effect of a valence-band offset on barrier formation in graded $Hg_{1-x}Cd_xTe$ heterojunctions. J Appl Phys. 1988;64:6373–8.
32. Madarasz FL, Szmulowicz F. Valence-band barrier formation in graded $Hg_{1-x}Cd_xTe$ heterojunctions with a valence-band offset included. J Appl Phys. 1989;66:3082–7.
33. Djaloshinski L, Nemirovsky Y. Methodology of abrupt heterostructures: band diagram calculations. Solid-State Electronics. 1996;39:1385–90.
34. Nemirovsky Y, Gordon G, Goren D. Measurement of band offsets and interface charges by the C-V matching method. J Appl Phys. 1998;84:1113–20.
35. Goren D, Asa G, Nemirovsky Y. Barrier formation at graded HgTe/CdTe heterojunctions. J Appl Phys. 1996;80:5083–8.
36. Johnson NF, Hui PM, Ehrenreich H. Valence-band-offset controversy in HgTe/CdTe superlattices: a possible resolution. Phys Rev Lett. 1988;61:1993–5.
37. Shih CK, Spicer WE. Determination of a natural valence-band offset: the case of HgTe-CdTe. Phys Rev Lett. 1987;58:2594–7.
38. Altschul VA, Finkman E, Bahir G. Approximations for Carrier density in non-parabolic semiconductors. IEEE Trans Elec Dev. 1992;39:1312–6.
39. Fu Y, Lu W. Physical models of semiconductor quantum devices. 1th ed. Beijing: Science Press; 2005. p. 308.
40. DESSIS ISE TCAD Manual, Release 10.06 (ISE Integrated Systems Engineering AG, Zurich, 2005), 15.137.
41. He Y, Wei T. The computer simulation method of semiconductor devices. 1st ed. Beijing: Science Press; 1989.
42. Zhao H. The computer simulation of semiconductor devices.1th ed. Tianjin: Tianjin University Press; 1989.
43. Cang T. The numerical analysis of semiconductor devices. 1st ed. Beijing: Publishing House of Electronics Industry; 1985.
44. Lopes VC, Syllaios AJ, Chen MC. Minority carrier lifetime in mercury cadmium telluride. Semicond Sci Technol. 1993;8:824–41.
45. Hu W-D, Chen X-S, Ye Z-H, Zhang J, Yin F, Lin C, Li Z, Lu W. Accurate simulation of temperature-dependence of dark current in HgCdTe infrared detector assisted by analytical modeling. J Electron Mater. 2010;39:981–5.
46. Rogalski A. Infrared detectors. Amsterdam: Gordon and Breach Science Publishers; 2000. p. 200–2.
47. Talipov NK, Ovsyuk VN, Remesnik VG, Vasilyew W. Electrical activation of boron implanted in p-HgCdTe ($x = 0.22$) by low-temperature annealing under an anodic oxide. Mater Sci Eng B. 1997;44:266–9.
48. Nemirovsky Y, Rosenfeld D, Adar R, Kornfeld A. Tunneling and dark currents in HgCdTe photodiodes. J Vac Sci Technol, A. 1989;7:528–35.

49. Nemirovsky Y, Fastow R, Meyassed M, et al. Trapping effects in HgCdTe. J Vac Sci Technol, B. 1991;9:1829–39.
50. Ellion CT, Gordon NT, Hall RS. Reverse breakdown in long wavelength lateral collection $Cd_xHg_{1-x}Te$ diodes. J Vac Sci Technol, A. 1990;8:1251–3.
51. Rosenfeld D, Bahir G. A model for the trap-assisted tunneling mechanism in diffused n-p and implanted n^+-p HgCdTe photodiodes. IEEE Trans Elec Dev. 1992;39:1638–45.
52. Hurkx GAM, Klaassen DBM, Knuvers MPG. A new recombination model for device simulation including tunneling. IEEE Trans Elec Dev. 1992;39(2):331–8.
53. Ye ZH, Wu J, Hu XN, et al. Study of HgCdTe p(+)-on-n long-wavelength heterojunction detector. J Infrared Millim Waves. 2004;23(6):423–6.
54. Kozlowski L, Vural K, Luo J, et al. Low-noise infrared and visible focal plane arrays. Opto-Electron Rev. 1999;7:259–69.
55. Quan ZJ, Chen XS, Hu WD, Ye ZH, Hu XN, Li ZF, Lu W. Modeling of dark characteristics for long-wavelength HgCdTe photodiode. Opt Quant Electron. 2006;38:1107–13.
56. Gopal Vishnu, Qiu Weicheng, Weida Hu. Modelling of illuminated current–voltage characteristics to evaluate leakage currents in long wavelength infrared mercury cadmium telluride photovoltaic detectors. J Appl Phys. 2014;116:184503.
57. Qiao H, Liao Y, Hu W D, et al. "Real-time study of gamma irradiation on $Hg_{1-x}Cd_{-x}Te$ focal plane photodiodes. Acta Physica Sinica. 2008:7088–93.
58. Quan Z-J, Z-F LI, W-D HU, et al. Parameter s extraction from the dark current characteristics of long-wavelength HgCdTe photodiode. J Infrared Millim Waves. 2007;2:003.
59. Quan Z-J, Ye Z-H, Hu W-D, et al. Study on structural optimization of decreasing the crosstalk of planar HgCdTe focal plane arrays. J Infrared Millim Waves. 2006;25(5).
60. Rogalski A. Infrared detectors: status and trends. Prog Quantum Electron. 2003;27:59–210.
61. Becker LSR. Multicolor LWIR focal plane array technology for space and ground based applications. SPIE. 2004;5564:1–14.
62. Mitra P, Barnes SL, Case FC. MOCVD of bandgap-engineered HgCdTe p-n-N-P dual-band infrared detector arrays. J Electron Mater. 1997;26(6):482–7.
63. Baylet J, Zanatta J P, Chance D, et al. Recent development in infrared FPAs with multispectral 1282 IRCMOS. SPIE. 2002;4650:128–37.
64. Rajavel RD, Brewer PD, Jamba DM, et al. Status of HgCdTe-MBE technology for producing dual-band infrared detectors. J Crystal Growth. 2000;214:1100–5.
65. Zanatta JP, Ferret P, Loyer R, et al. Single and two colour infrared focal plane arrays made by MBE in HgCdTe. Proc SPIE. 2000;4130:441–51.
66. Tennant WE, Thomas M, Kozlowski LJ, et al. A novel simultaneous unipolar multispectral integrated technology approach for HgCdTe IR detectors and focal plane arrays. J Electron Mater. 2001;30(6):590–4.
67. Smith EPG, Pham LT, Venzor GM, et al. HgCdTe focal plane arrays for dual-color mid- and long-wavelength infrared detection. J Electron Mater. 2004;33(6):509–16.
68. Ye Z. Integrated two-color HgCdTe photodetector. Ph.D. thesis; 2005.
69. Rajavel RD, Jamba DM, Wa OK, et al. High performance HgCdTe two-color infrared detectors grown by molecular beam epitaxy. J Crystal Growth. 1997;175:653–8.
70. Rajavel RD, Jamba DM, Jensen JE, Hu OK, Wilson JA, Johnson JL, Patten EA, Kosai K, Goetz P, Johnson SM. Molecular beam epitaxial growth and performance of integrated multispectral HgCdTe photodiodes for the detection of mid-wave infrared radiation. J. Crystal Growth. 1998;184:1272–8.
71. Rajavel RD, Jamba DM, Jensen JE, Wu OK, Brewer PD, Wilson JA, Johnson JL, Patten EA, Kosai K, Caulfield JT, Goetz PM. Molecular beam epitaxial growth and performance of HgCdTe-Based simultaneous-mode two-color detectors. J Electron Mater. 1998;27:747–51.
72. Ye ZH, Zhou WH, Hu WD, Hu XN, Ding RJ, He L. Spectral study on response of HgCdTe IR two-color detector arrays. J Infrared Millims Waves. 2009;28(1):4–7.
73. Hu W-D, Chen X-S, Ye Z-H, Lu W. An improvement on short-wavelength photoresponse for heterostructure HgCdTe two-color infrared detector. Semicond Sci Technol. 2010;25:045028.

74. Borniol ED, Baylet J, Zanatta JP, Mibord S, Gravrand O, Rothan F, Castelein P, Chamonal JP, Ravetto M, Destefanis G. Dual-band infrared HgCdTe focal plane array. Proc SPIE. 2003;4820:491–9.
75. Baylet J, Zanatta J P, Chance D. et al. Recent advances in development of infrared multispectral 1282 FPAs. Proc SPIE. 2002;4721:134–43.
76. Sood A, Egerton J, Puri Y, et al. Design and development of multi-color detector arrays. Proc SPIE. 2004;5564:27–33.
77. Tribolet Philippe and Destefanis. Gerard Third generation and multi-color IRFPA developments: a unique approach based on DEFIR. Proc SPIE. 2005;5783:350–65.
78. Rogalski A. HgCdTe infrared detector material: history, status and outlook. Rep Prog Phys. 2005;68:2267.
79. Cabanski W, Breiter R, Mauk KH, et al. High-resolution focal plane array IR detection modules and digital signal processing technologies at AIM. Proc SPIE. 2003;5074:72–5.
80. Ballet P, Noel F, Pottier F, Pottier F, Plissard S, Zanatta JP, Baylet J, Gravrand O, De Borniol E, Martin S, Castelein P. Dual-band infrared detectors made on high-quality HgCdTe epilayers grown by molecular beam epitaxy on CdZnTe or CdTe/Ge substrates. J Electron Mater. 2004;33(6):667–72.
81. Ye ZH, Wu J, Hu XN, Wu Y, Liao QJ, Zhang HY, Wang JX, Ding RJ, He L. SPIE. 2004;5640:66.
82. Hu WD, Ye ZH, Liao L, Chen HL, Chen L, Ding RJ, He L, Chen XS, Lu W. A 128 × 128 long-wavelength/mid-wavelength two-color HgCdTe infrared focal plane array detector with ultra-low spectral crosstalk. Opt Lett. 2014;39:5130–3.
83. Liang J, Hu WD, Ye ZH, Liao L, Li ZF, Chen XS, Lu W. Improved performance of HgCdTe infrared detector focal plane arrays by modulating light field based on photonic crystal structure. J Appl Phys. 2014;115:184504.
84. Li Y, Ye ZH, Hu WD, Lei W, Gao YL, He K, Hua H, Zhang P, Chen YY, Lin C, Hu XN, Ding RJ, He L. Numerical simulation of refractive-microlensed HgCdTe infrared focal plane arrays operating in optical systems. J Electron Mater. 2014;43:2879–87.
85. Ferret P, Zanatta JP, Hamelin R, et al. Status of the MBE technology at Leti LIR for the manufacturing of HgCdTe focal plane arrays. J Electron Mater. 2000;29(6):641–7.
86. Baylet J, Gravrand O, Laffosse E, Vergnaud C, Ballerand S, Aventurier B, Deplanche JC, Ballet P, Castelein P, Chamonal JP, Million A, Destefanis G. Study of the pixel-pitch reduction for HgCdTe infrared dual-band detectors. J Electron Mater. 2004;33(6):690–700.
87. Jozwikowski K, Rogalski A. Computer modeling of dual-band HgCdTe photovoltaic detectors. J Appl Phys. 2001;90(3):1286–91.
88. Bellotti E, D'Orsogna D. Numerical analysis of HgCdTe simultaneous two-color photovoltaic infrared detectors. IEEE J Quantum Electron. 2006;42(4):418–26.
89. Akira Ajisawa, Naoki Oda. Improvement in HgCdTe diode characteristics by low temperature post-implantation annealing. J Electr Mater. 1995;24:1105–11.
90. Cao G, Gong H, Qiu H, Kong L, Hu SH, Dai N. Bias-dependent photocurrent of $Hg_{1-x}Cd_xTe$ photodiodes. J Appl Phys. 2005;98:064504.
91. Gilmore AS, Bangs J, Gerrish A. Current voltage modeling of current limiting mechanisms in HgCdTe Focal Plane Array photodetector. J Electr Mater. 2005;34:913–21.
92. Quan ZJ, Li ZF, Hu WD, Ye ZH, Hu XN, Lu W. Parameter determination from resistance-voltage curve for long-wavelength HgCdTe photodiode. J Appl Phys. 2007;100:084503.
93. Graft A, Fischer T, Gray A, et al. Illumination-dependent dynamic resistance of $Hg_{1-x}Cd_xTe$ heterojunction photodiodes. J Appl Phys. 1993;74:5705–12.
94. Wei L, Hong L, et al. The application of solid crystallization process in optimization algorithm. Chin J Comput Phys. 1999;216:141–4.
95. Hu WD, Chen XS, Ye ZH, Lu W. A hybrid surface passivation on HgCdTe long wave infrared detector with in-situ CdTe deposition and high-density Hydrogen plasma modification. Appl Phys Lett. 2011;99:091101.

96. Chen GB, Lu W, Chen XS, Li ZF, Cai WY, He L, Hu XN, Li YJ, Shen SC. Study on optimizing the performance of infrared detectors using material chip technology. Semicond Sci Technol. 2003;18:887–90.
97. Sizov FF, Gumenjuk-Sichevska JV, Lysiuk IO, et al. Temperature dependence of the dark current in HgCdTe photodiode arrayes. SPIE. 1998;5957(59571L):1–8.
98. Wenus J, Rutkowski J, Rogalski A. Analysis of VLWIR HgCdTe photodiode performance. Opto-Electron Rev. 2003;11:143–9.
99. Juang FS, Su YK, Chang SM, et al. Analysis of the dark current of focal-plane-array $Hg_{1-x}Cd_xTe$ diode. Mater Chem Phys. 2000;64:131–6.
100. Zemel A, Lukomsky I, Weiss E. Mechanism of carrier transport across the junction of narrow band-gap planar np HgCdTe photodiodes grown by liquid-phase epitaxy. J Appl Phys. 2005;98(1–7):054504.
101. Hu WD, Chen XS, Yin F, Quan ZJ, Ye ZH, Hu XN, Li ZF, Lu W. Analysis of temperature dependence of dark current mechanisms for long-wavelength HgCdTe photovoltaic infrared detectors. J Appl Phys. 2009;105:104502.
102. Chu J. The physics of narrow band gap semiconductors. 1th ed. Beijing: Science Press;2005. p. 283.
103. Scott W, Stelzer EL, Hager RG. Electrical and far-infrared optical properties of p-type $Hg_{1-x}Cd_xTe$. J Appl Phys. 1974;47:1408–14.
104. Nishino H, Ozaki K, Tanaka M, et al. Acceptor level related Shockley-Read-Hall centers in p-HgCdTe. J. Crys. Growth. 2000;214(215):275–9.
105. Chen MC, Colombo L, Dodge JA et al. The minority carrier lifetime in doped and undoped p-type $Hg_{0.78}Cd_{0.22}Te$ liquid phase epitaxy films. J Electr Mater. 1995;24:539–44.
106. Lanir M, Vanderwyck AHB, Wang CC. Minority-carrier-lifetime determination in $Hg_{0.68}Cd_{0.32}Te$. J Appl Phys. 1978;49:6182–4.
107. Fastow R, Nemirovsky Y. The excess carrier lifetime in p-type HgCdTe measured by photoconductive decay. J Appl Phys. 1989;66:1705–10.
108. De Souza ME, Boukerche M, Faurie JP. Minority-carrier lifetime in p-type (111) B HgCdTe grown by molecular-beam epitaxy. J Appl Phys. 1990;68:5195–9.
109. Cui HY, Zeng JD, Tang NY, Tang Z. Analysis of the mechanisms of electron recombination in HgCdTe infrared photodiode. Opt. Quantum Electron. 2013;45(7):629–34.
110. Qiu Weicheng, Weida Hu. Laser beam induced current microscopy and photocurrent mapping for junction characterization of infrared photodetectors. Sci China-Phys Mech Astron. 2015;58(2):027001.
111. Qiu WC, Cheng XA, Wang R, et al. Novel signal inversion of laser beam induced current for femtosecond-laser-drilling induced junction on vacancy-doped p-type HgCdTe. J Appl Phys. 2014;115:204506.
112. Redfern DA, Fang W, Ito K, et al. Low temperature saturation of p-n junction laser beam induced current signals. Solid-State Electron. 2004;48:409.
113. Feng AL, Li G, He G, et al. Dependence of laser beam induced current on geometrical sizes of the junction for HgCdTe photodiodes. Opt Quantum Electron. 2013.
114. Redfern DA, Thomas JA, Musca CA, et al. Diffusion length measurements in p-HgCdTe using laser beam induced current. J Electron Mater. 2001;30:696–703.
115. Yin F, Hu WD, Quan ZJ, Zhang B, Hu XN, Li ZF, Chen XS, Lu W. Determination of electron diffusion length in HgCdTe photodiodes using laser beam induced current. Acta Physica Sinica. 2009;58:7885–9.
116. Ong VKS, Wu D. Determination of diffusion length from within a confined region with the use of EBIC. IEEE Trans Electron Devices. 2001;48(2):332.
117. Redfern DA, Smith E, Musca CA, Dell JM, Faraone L. Interpretation of current flow in photodiode structures using laser beam-induced current for characterization and diagnostics. IEEE Trans Electron Devices. 2006;53:23–31.
118. Redfern DA, Musca CA, Dell JM, Faraone L. Characterization of electrically active defects in photovoltaic detector arrays using laser beam-induced current. IEEE Trans Electron Devices. 2005;52:2163–74.

119. Yin F, Hu WD, Zhang B, Li ZF, Hu XN, Chen XS, Lu W. Simulation of laser beam induced current for HgCdTe photodiodes with leakage current. Opt Quant Electron. 2009;41:805–10.
120. Feng AL, Li G, He G, et al. The role of localized junction leakage in the temperature-dependent laser-beam-induced current spectra for HgCdTe infrared focal plane array photodiodes. J Appl Phys. 2013;114:173107.
121. Hu WD, Chen XS, Ye ZH, Feng AL, Yin F, Zhang B, Liao L, Lu W. Dependence of ion-implant-induced LBIC novel characteristic on excitation intensity for long-wavelength HgCdTe-based photovoltaic infrared detector pixel arrays. IEEE J Sel Top Quant. 2013;19:4100107.
122. Bubulac LO, Tennant WE. Role of Hg in junction formation in ion-implanted HgCdTe. Appl Phys Lett. 1987;51:355–7.
123. Bubulac LO. Dependence of junction formation on substrate in implanted HgCdTe. Appl Phys Lett. 1985;46:976–8.
124. Arias JM, Zandian M, Bajaj J, Pasko JG, Bubulac LO, Shin SH, Dewames RE. Molecular beam epitaxy HgCdTe growth-induced void defects and their effect on infrared photodiodes. J Electron Mater. 1995;24:521–4.
125. Buell AA, Pham LT, Newton MD, et al. Physical structure of molecularbeam epitaxy growth defects in HgCdTe and their impact on two-color detector performance. J Electron Mater. 2004;33:662–6.
126. Hu WD, Chen XS, Ye ZH, Chen YG, Yin F, Zhang B, Lu W. Polarity inversion and coupling of laser beam induced current in As-doped long-wavelength HgCdTe infrared detector pixel arrays: Experiment and simulation. Appl Phys Lett. 2012;101:181108.

http://www.springer.com/978-3-662-52716-0

Technology for Advanced Focal Plane Arrays of HgCdTe and AlGaN

He, L.; Yang, D.; Ni, G.

2016, X, 690 p. 620 illus., 299 illus. in color., Hardcover
ISBN: 978-3-662-52716-0